NOVEL FABRY-PÉROT RESONATORS FOR SENSING APPLICATIONS

JIANG XIAOPING

PhD

The Hong Kong Polytechnic University

2023

The Hong Kong Polytechnic University
Department of Electrical and Electronic Engineering

Novel Fabry-Pérot Resonators for Sensing Applications

Jiang Xiaoping

A thesis submitted in partial fulfillment of the requirements for
the degree of Doctor of Philosophy
June 2023

CERTIFICATE OF ORIGINALITY

I hereby declare that this thesis is my own work and that, to the best of my knowledge and belief, it reproduces no material previously published or written, nor material that has been accepted for the award of any other degree or diploma, except where due acknowledgment has been made in the text.

Signature: _____

Name of Student: Jiang Xiaoping

Abstract

Optical thin-film sensors and transducers have been developing rapidly for decades with applications in various fields, e.g., chemical detection, biological sensing and medical imaging. Optical thin-film sensors utilize the interaction of light with materials or objects for information regarding their properties and the environment. This thesis is focused on two types of sensing applications: (i) refractive index sensing and (ii) photoacoustic sensing and imaging. For refractive index sensing, one well-established type of sensor is the surface plasmon resonator (SPR), where a refractive index change causes the resonance to drift thus resulting in amplitude or phase shifts. For photoacoustic sensing and imaging, optical transducers detect either local pressure changes, e.g., SPR, or resonance light path changes, e.g., Fabry-Pérot (FP) thin-film resonators. An FP thin-film resonator consists of a cavity sandwiched between two reflecting mirrors. When in resonance, incident light wave interferes with the light wave circulating inside the cavity, resulting in a decrease in reflectivity.

For refractive index sensing, sensors can be evaluated by their figure of merit (FOM) and sensitivity, which refers to the noise-equivalent refractive index unit. In this thesis, at 633 nm wavelength, a novel open cavity FP structure based on a high-aspect-ratio-grating (HARG-FP) was investigated for refractive index sensing applications. A lateral comparison with SPR was drawn. The results indicated 10- and

44-fold improvement in FOM with TM and TE polarization compared to the conventional SPR, respectively. TE samples exhibited a single-shot sensitivity of 1.87×10^{-8} RIU. With 794 frames averaging (~1-second acquisition), the sensitivity can be further improved to 1.61×10^{-9} RIU, demonstrating ultra-sensitivity.

For the field of photoacoustic sensing, optical transducers offer exceptional potential of high responsivity, broad bandwidth and significantly reduced acoustic impedance mismatch compared with conventional piezoelectric transducers. Besides sensitivity, bandwidth is another crucial factor characterizing an acoustic transducer. A total-internal-reflection-based Fabry-Pérot resonator (TIR-FP) was evaluated for ultra-sensitive wideband ultrasound and photoacoustic applications at around 1550-nm wavelength. The proposed transducer consisted of a 12-nm-thick gold layer and a dielectric cavity. 1.9-μm-thick-PMMA- and 3.4-μm-thick-PDMS-based resonators showed responsivities of 3.6- and 30-fold improvements compared with the conventional SPR, respectively. Examined with photoacoustic signals generated by focused nanosecond laser pulses, bandwidths for the PMMA- and PDMS-based devices were 110 MHz and 75 MHz, respectively. Single-shot sensitivity of 160 Pa was obtained for the PDMS-based TIR-FP. The results indicated that, with the proposed resonator in imaging applications, sensitivity and the signal-to-noise ratio can be improved significantly without compromising the bandwidth.

Research has been proposed for a grating-based Fabry-Pérot (GFP) resonator as a

highly sensitive detector. The structure features two diffraction gratings as the mirrors forming the FP. The period of the grating is engineered so that only the zero-th and first orders exist inside the cavity and only the zero-th order exists outside the cavity. with a 50-μm cavity, double gratings enable rich interaction between the zero-th and the first order, which gives resonance linewidth ranging from 1 pm to 1 nm with Q ranging from 1.5×10^3 to 1.5×10^6. The freedom in Q and dynamic range offered within the same structure promises great potential for photoacoustic sensing.

Publications Arising from the Thesis

(1) **X. P. Jiang,** M. Q. Shen, D. P. K. Lun, W. Chen, and M. G. Somekh, "A total-internal-reflection-based Fabry-Perot resonator for ultra-sensitive wideband ultrasound and photoacoustic applications," Photoacoustics, vol. 30, APR 2023. (IF=9.656)

(2) **X. P. Jiang**, M. Q. Shen, D. P. K. Lun, W. Chen, and M. G. Somekh, "High Aspect-Ratio Open Grating Fabry-Perot Resonator for High-Sensitivity Refractive Index Sensing," IEEE Sensors Journal, vol. 22, no. 16, pp. 15923-15933, AUG 15 2022. (IF=4.325)

(3) M. Q. Shen, Q. Zou, **X. P. Jiang**, F. Feng, and M. G. Somekh, "Single-shot three-input phase retrieval for quantitative back focal plane measurement," Photonics Research, vol. 10, no. 2, pp. 491-502, FEB 1 2022. (IF=7.254)
(Contribution: System Build-up, Data Processing)

Under Preparation:

(1) **X. P. Jiang**, M. Q. Shen, M. G. Somekh, “Double grating based Fabry-Perot resonator for ultra-sensitive and high-dynamic-range photoacoustic applications”.

Acknowledgements

I would like to express my deepest gratitude and appreciation to all those who have contributed to the completion of this thesis.

First and foremost, I would like to extend my most sincere gratitude to my esteemed supervisors, Dr. Wen Chen, Dr. Daniel P. K. Lun and Prof. Michael Somekh. The guidance, invaluable expertise and unlimited support have been instrumental in shaping this thesis. I am truly grateful for the continued encouragement, insightful discussions and countless hours and numerous emails that have been devoted to this research project and constructive feedback provided that made this project. It has been a great honor.

I would like to express my wholehearted appreciation to the love of my life, my family. Your unyielding support and unwavering love have been a constant fountain of strength and motivation to me. I am forever grateful to have you in my life, and my love to you is beyond words.

I would like to offer my special thanks to Dr. Terrance Wong for his expertise, generosity, experience and patience in the cleanroom.

I would like to extend my profound thanks to Dr. Fu Feng, Dr. Shibiao Wei, Dr. Suejit Pechprasarn, Dr. Wei Song and Prof. Xiaocong Yuan for thoughtful discussion, technical assistance and providing convenience to this project in time of need without

hesitation.

I would also like to extend my thanks to my friends, Jiacheng Bao, Xianle Cao, Zhe Cao, Jian Cheng, Yiming Gan, Shangcheng Kong, Yilun Le, Tong Liu, Zun Niu, Tianyuan Sun, Zhiyu Zhou, Weiguo Zhou and so on, who have provided nothing but constant support, encouragement and camaraderie.

Lastly, I would like to thank the Hong Kong Polytechnic University and the Department of Electronic and Information Engineering for providing me with the opportunity. I am sincerely grateful.

Xiaoping Jiang

11/6/2023

Table of Contents

List of Figures

List of Tables

List of Abbreviations

BS	beamsplitter
BSW	Bloch surface wave
CVD	chemical vapor deposition
CWL	continuous-wave laser
DAQ	data acquisition
DM	dichroic mirror
DMD	digital micro-mirror
DUV	deep ultra-violet
EMA	effective medium approximation
EOM	electro-optic modulator
FDTD	finite-difference time-domain
FEM	finite element method
FOM	figure of merit
FP	Fabry-Pérot
FWHM	full width half maximum
GFP	grating-based Fabry-Pérot
HARG-FP	high-aspect-ratio-based Fabry-Pérot
LRSPR	Long-range surface plasmon resonance
MIM	metal-insulator-metal
NA	numerical aperture

NEP	noise-equivalent pressure
OR-PAM	optical-resolution photoacoustic microscopy
PAI	photoacoustic imaging
PDMS	polydimethylsiloxane
PL	pulsed laser
PMMA	polymethyl methacrylate
PVD	physical vapor deposition
PZT	lead zirconate titanate
Q	quality factor
RCWA	rigorous coupled wave analysis
RIU	refractive index unit
SLM	spatial light modulator
SNR	signal-to-noise ratio
SP	surface plasmon
SPR	surface plasmon resonator
TE	transverse electric
TIR-FP	total-internal-reflection-based Fabry-Pérot
TM	transverse magnetic

Chapter 1 Introduction

1.1 Background

Optical sensing has been playing an increasingly important role and revolutionizing our perception in various fields including telecommunications, industrial evaluation, pathological examination and vital signs monitoring [1-8].

Operating from ultraviolet to mid-infrared, an optical sensor is designed to convert the desired measurand to modulation of optical properties, e.g., intensity, wavelength, phase or polarization [9, 10].

The advantages of optical sensing include non-contact measurements, high precision, fast response time and remote sensing capability. Moreover, optical sensors are also less susceptible to electromagnetic interference, making them suitable for applications in electrically noisy environments. Additionally, they can be miniaturized, allowing for integration into compact devices and systems [11].

One type of optical sensor widely used in many applications is the thin-film Fabry-Pérot (FP) interferometer, which consists of two reflecting mirrors and a cavity in between. FP is based on interference of light waves. The FP structure exploits interference to create constructive and destructive interference at different wavelengths. Constructive interference results in resonance where signal amplitudes are greatly enhanced. Thin-film FP resonators lend themselves to a wide range of

applications, e.g., optical filters and acoustic transducers [12, 13].

The focus of the research is on high responsivity, improved sensitivity and broad bandwidth. A research challenge faced by conventional sensors is the intrinsic trade-off between responsivity and bandwidth. Therefore, to improve and break the conventional trade-off, novel structures have to be designed.

In this thesis, three novel FP structures will be introduced and analyzed for their sensitivity and other crucial metrics in their designated application fields.

1.2 Thesis Structure

This Ph.D. thesis is composed of 7 chapters, and Chapters 3-6 are presented based on either my published papers or papers under preparation. The layout of the thesis is as follows:

Chapter 1 introduces the background, points out the challenge faced by conventional optical sensors and presents the layout of the thesis.

Chapter 2 briefly introduces the fundamentals of the thin-film optics and reviews some prominent works of optical sensors for refractive index sensing and ultrasound and photoacoustic sensing.

Chapter 3 presents a high-aspect-ratio-based Fabry-Pérot (HARG-FP) structure for high figure-of-merit (FOM) refractive index sensing with theoretical analysis and experimental results to demonstrate its capability of high figure-of-merit (FOM) and high sensitivity.

Chapter 4 presents a total-internal-reflection-based Fabry-Pérot (TIR-FP) structure for ultrasound and photoacoustic sensing applications with theoretical analysis of both the optical and acoustic properties to elucidate the factor controlling the sensitivity and bandwidth and its potential for wide-acoustic-bandwidth high-sensitivity detection. This chapter lays the foundation for experiments.

Chapter 5 presents the experiment results of TIR-FP with TE polarization and two materials for FP cavity, i.e., PMMA and PDMS. Responsivity and bandwidth performances are presented and evaluated with ultrasonic and photoacoustic signals. A detailed analysis of noise-equivalent sensitivity is also presented.

Chapter 6 presents a grating based Fabry-Pérot (GFP) structure as an ultra-sensitive ultrasound and photoacoustic transducer. Both single-layer GFP and double-layer GFP are presented and analyzed with a comparison with a conventional FP sensor. The capability of high sensitivity and extraordinary intrinsic dynamic range is discussed in detail.

Chapter 7 summarizes the research findings and looks into prospects of the proposed sensors for more improvement over the designated metrics.

Chapter 2 Introduction to Thin-Film Optics and Literature Review

2.1 Overview

Optical Sensing is a fast-developing technology and has been widely used in many fields, e.g., medical diagnostics [2, 14, 15], chemical analysis [16, 17] and civil engineering [18]. The past few years have witnessed ever-growing research interests on optical sensors [19]. A typical operating principle of optical sensors is measuring the change of k-vector caused by changes in the desired measurand, e.g., temperature, analyte concentration, pressure. The change in k-vector can be detected by changes in resonant angle, wavelength, as well as phase or intensity of the reflected signal. The change in resonance can be categorized into internal perturbation and external perturbation. In this chapter, we first re-visit the governing fundamentals of thin-film optics, and then focus the discussion on two sectors of optical sensing: refractive index sensing and acoustic sensing.

2.2 Introduction to Thin-Film Optics

2.2.1 Wave Function for Monochromatic Electromagnetic Waves

A lightwave, as a specified type of electromagnetic wave, can be described by the most fundamental equations in electromagnetism, Maxwell's equations, the

differential formulation of which is given in international system of units (meter-kilogram-second units) by

$$\nabla \cdot \mathbf{D} = \rho \tag{2.1}$$

$$\nabla \cdot \mathbf{B} = 0 \tag{2.2}$$

$$\nabla \times \mathbf{E} = -\frac{\partial \mathbf{B}}{\partial t} \tag{2.3}$$

$$\nabla \times \mathbf{H} = \mathbf{J} + \frac{\partial \mathbf{D}}{\partial t} \tag{2.4}$$

$$\mathbf{D} = \varepsilon \mathbf{E} \tag{2.5}$$

$$\mathbf{B} = \mu \mathbf{H} \tag{2.6}$$

where **E** and **H** are electric field vector and magnetic field vector, **D** and **B** are electric displacement and magnetic induction, ρ and J are free electric charge and electric current, ε and μ are permittivity and permeability.

These equations describe the relationship between electricity and magnetism and underline the mathematical framework for propagation of electric and magnetic fields and their interaction with matter and laid the foundation for the technology advances of the microwave and optics field.

As is well known, these equations predict transverse electromagnetic waves. From the Maxwell's Equations, the wave equations can be derived for monochromatic plane waves and given by

$$\mathbf{E} = \boldsymbol{E}_0 e^{i(\omega t - \boldsymbol{k}\cdot\boldsymbol{r})} \tag{2.7}$$

$$\mathbf{H} = \boldsymbol{H}_0 e^{i(\omega t - \boldsymbol{k}\cdot\boldsymbol{r})} \tag{2.8}$$

where $\boldsymbol{E}_0$ and $\boldsymbol{H}_0$ are the constant vectors with complex amplitudes constant in time and frequency, ω is the angular frequency, $\boldsymbol{k}$ is the wave vector and $\boldsymbol{r}$ is coordinates.

The magnitude of the wave vector $\boldsymbol{k}$ is given by

$$|\boldsymbol{k}| = \omega\sqrt{\mu\varepsilon} \tag{2.9}$$

And the refractive index n of a material is given by the square root of the relative permittivity.

$$n = \sqrt{\varepsilon/\varepsilon_0} \tag{2.10}$$

In a homogeneous and isotropic charge-free medium where $\rho = 0$, it can be shown that $\boldsymbol{E}_0$ and $\boldsymbol{H}_0$ are perpendicular to the wave vector $\boldsymbol{k}$, therefore, perpendicular to the direction of the propagation. Thus, the electromagnetic waves are transverse waves.

2.2.2 Polarization State

Thin film optics, as a branch of optics, focuses on the study of optical properties and phenomena in structures consisting of one or more layers of different materials, i.e., layered media. The polarization state related to the incident sample plane is an important property describing a monochromatic electromagnetic wave [20]. It denotes the direction of oscillation of the field vector, specifically, the path traced by the end point of the electric field vector **E**. Typically, it is an ellipse as shown in Fig. 2.1. The polarization state of light can be represented with a 4 x 4 matrix, i.e., the Mueller Matrix. Since it describes the electric field rather than the power, phase information is maintained.

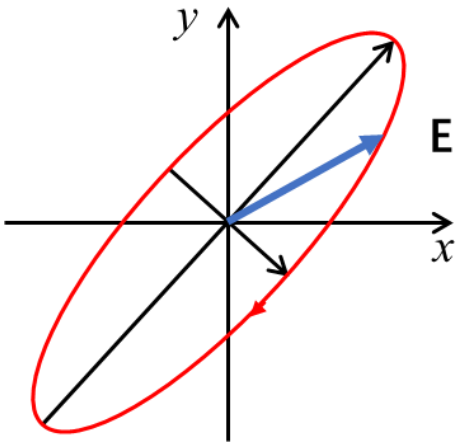

Fig. 2.1. A typical polarization ellipse. The shown plane is perpendicular to the direction of propagation where a red ellipse represents the end track of the electric field vector.

By quantitative measurement of the polarization change of the light with a known polarization reflected off a surface, the refractive index and thickness information of the material can be precisely quantified [21, 22]. Two special types of polarizations are mostly concerned in research, i.e., linear polarization and circular polarization [22-25]. Linear polarizations can be decomposed into two components, i.e., *p*-polarization and *s*-polarization, also known as transverse magnetic (TM) and transverse electric (TE) polarization. In free space, magnetic fields and electric fields are always perpendicular to the direction of propagation and each other. In TE polarization, magnetic field is perpendicular to the incident plane, whereas in TM polarization, magnetic field is perpendicular to the incident plane.

A scheme is shown in Fig. 2.2 where TE- and TM-polarized waves are transmitted or reflected at the interface of two media.

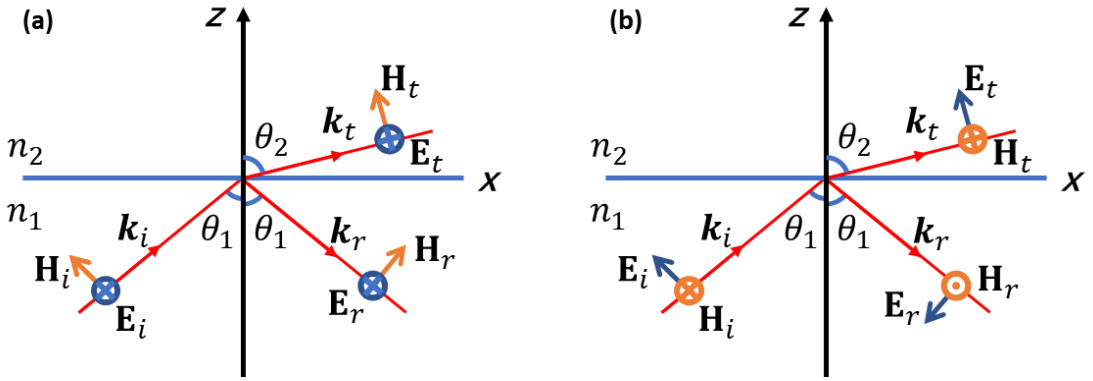

Fig. 2.2. Transmission and reflection scheme of (a) s-polarization (TE) and (b) p-polarization (TM) at the interface of two homogeneous and isotropic media.

2.2.3 Boundary Conditions

When an electromagnetic wave propagates through layered media, one of the most concerned problems is matching the boundary conditions between subsequent layers. The boundary conditions can be deduced based on Fig. 2.2 for both TE and TM polarizations.

Two primary boundary conditions in optics concerning thin-film structures are the continuity of (i) the normal components of electric field **E** and (ii) the tangential components of magnetic induction **B**.

For analytical expression of the boundary conditions, the Gauss divergence

theorem can be applied to

$$\iiint_V \ \nabla \cdot \boldsymbol{F}\, dV = \oiint_S \ \boldsymbol{F} \cdot d\mathbf{S} \tag{2.11}$$

to both sides of Eq. (2.2),

$$\boldsymbol{n} \cdot (\mathbf{B}_2 - \mathbf{B}_1) = 0 \tag{2.12}$$

where $\boldsymbol{n}$ is normal vector of the interface of media 1 and 2. This is the boundary condition for continuity of tangential components of magnetic induction **B**.

Applying the Stokes theorem

$$\iint_S \ \nabla \times \boldsymbol{F} \cdot d\mathbf{S} = \oint_l \ \boldsymbol{F} \cdot d\boldsymbol{l} \tag{2.13}$$

to both sides of Eq. (2.3) [26], this leads to

$$\boldsymbol{n} \times (\mathbf{E}_2 - \mathbf{E}_1) = 0 \tag{2.14}$$

These boundary conditions can be written as

$$\mathbf{B}_{1n} = \mathbf{B}_{2n} \tag{2.15}$$

$$\mathbf{E}_{1t} = \mathbf{E}_{2t} \tag{2.16}$$

Therefore, at the interface of two dielectric materials, where surface charge and current do not exist, normal components of the magnetic induction and tangential components of the electric field are continuous across the interface.

2.2.4 Transmission, Reflection, Total Internal Reflection

When a light wave propagates to an interface of two media, reflection and refraction/transmission happen. Let $\boldsymbol{E}_i \exp\,[i(\omega t - \boldsymbol{k}_i \cdot \boldsymbol{r})]$ denote the electric field amplitude of an incident plane wave with wave vector $\boldsymbol{k}_i$. From Eq. (2.16), the

relationships between wave vectors of incident, reflected and transmitted waves at the interface (x=0) can be given by

$$\boldsymbol{k}_i \cdot \boldsymbol{r}_i = \boldsymbol{k}_r \cdot \boldsymbol{r}_r = \boldsymbol{k}_t \cdot \boldsymbol{r}_t \tag{2.17}$$

The wave vectors of the reflected and refracted waves satisfy the following equations, i.e., Snell's Law, in order to match the boundary conditions:

$$n_i \sin\theta_i = n_i \sin\theta_r = n_t \sin\theta_t \tag{2.18}$$

where subscripts i, r and t refer to incidence, reflection and transmission, n is refractive index and θ is the angle to normal.

Transmission and reflected coefficients can be given by imposing continuity boundary conditions to electronic and magnetic field components of s- and p-polarizations as shown in Fig. 2.2. The transmission and reflection coefficients can be given by

$$r_s = \frac{n_1 \cos\theta_1 - n_2 \cos\theta_2}{n_1 \cos\theta_1 + n_2 \cos\theta_2} \tag{2.19}$$

$$t_s = \frac{2n_1 \cos\theta_1}{n_1 \cos\theta_1 + n_2 \cos\theta_2} \tag{2.20}$$

$$r_p = \frac{n_1 \cos\theta_2 - n_2 \cos\theta_1}{n_1 \cos\theta_2 + n_2 \cos\theta_1} \tag{2.21}$$

$$t_p = \frac{2n_1 \cos\theta_1}{n_1 \cos\theta_2 + n_2 \cos\theta_1} \tag{2.22}$$

Consider the case where $n_1 > n_2$, and $\sin\theta_1 > \frac{n_2}{n_1}$, θ_2 becomes a complex angle and then, its cosine becomes imaginary:

$$\cos\theta_2 = \sqrt{1 - \sin^2\theta_2} = i\sqrt{\sin^2\theta_2 - 1} = \sqrt{\left(\frac{\sin\theta_1}{n_2/n_1}\right)^2 - 1} \tag{2.23}$$

There are no longer transmitted propagating waves, and all energy is reflected.

This is called total internal reflection and $\sin^{-1}\frac{n_2}{n_1}$ is called the critical angle. Above the critical angle, reflectivity becomes unity and transmittance vanishes, meaning that no energy is transmitted across the boundary.

It can be deduced that transmission does not vanish when Eq. (2.23) is substituted into Eqs. (2.20) and (2.22). The transmitted electric field becomes an evanescent wave described as

$$\mathbf{E}_t = \boldsymbol{E}_0 e^{i(\omega t - k_2(\boldsymbol{x}\sin\theta_2 + \boldsymbol{z}\cos\theta_2))} = \boldsymbol{E}_0 e^{i(\omega t - \boldsymbol{x}k_1\sin\theta_1 - \boldsymbol{z}\beta)} \tag{2.24}$$

where $\beta = k_2\sqrt{\left(\frac{\sin\theta_1}{n_2/n_1}\right)^2 - 1}$ is the attenuation coefficient and $1/\beta$ is referred to as the penetration depth.

2.2.5 Wave Propagation in Multilayer Media

In Fig. 2.2, at the interface between medium 1 and 2, a *S*-matrix form of the field continuity for both s- and p-polarization are given by

$$\begin{bmatrix} \boldsymbol{E}_1 \\ \boldsymbol{E}_1' \end{bmatrix} = \mathbf{D_1^{-1}D_2}\begin{bmatrix} \boldsymbol{E}_2 \\ \boldsymbol{E}_2' \end{bmatrix} \tag{2.25}$$

where

$$\mathbf{D_i} = \begin{bmatrix} 1 & 1 \\ \sqrt{\frac{\mu_i}{\varepsilon_i}}cos\theta_i & -\sqrt{\frac{\mu_i}{\varepsilon_i}}cos\theta_i \end{bmatrix} \quad \text{for } s\text{-polarization} \tag{2.26}$$

$$\mathbf{D_i} = \begin{bmatrix} cos\theta_i & cos\theta_i \\ \sqrt{\frac{\mu_i}{\varepsilon_i}} & -\sqrt{\frac{\mu_i}{\varepsilon_i}} \end{bmatrix} \quad \text{for } p\text{-polarization} \tag{2.27}$$

The S matrix is given by

$$\mathbf{S_{1,2}} = \mathbf{D_1^{-1}D_2} = \frac{1}{t_{12}}\begin{bmatrix} 1 & r_{12} \\ r_{12} & 1 \end{bmatrix} \tag{2.28}$$

A propagation matrix is defined by

$$\boldsymbol{\phi_i} = \begin{bmatrix} e^{ik_x d} & 0 \\ 0 & e^{-ik_x d} \end{bmatrix} \tag{2.29}$$

where d is the thickness of a medium.

Therefore, by cascading Eq. (2.19) for multi-layers, $\mathbf{S_{tot}}$ can be given by

$$\mathbf{S_{tot}} = \prod_{l=1}^{m-1} (\mathbf{S_{l-1,l}} \boldsymbol{\phi_l}) \mathbf{D_m} \tag{2.30}$$

And transmission and reflection coefficients are given by

$$t = \frac{1}{\mathbf{S_{tot}(1,1)}}, \quad r = \mathbf{S_{tot}(2,1)} \cdot t \tag{2.31}$$

2.2.6 Diffraction formulations

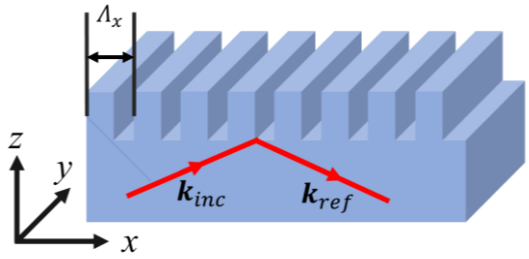

Fig. 2.3. A typical one-dimension diffraction grating with its grating vector in *x*-direction. The incident and reflected ***k***-vectors are in *x*-*z* plane.

As shown in Fig. 2.3, a diffraction grating is a periodic structure that diffracts light into several different directions. The *x*-components of the k-vectors of diffracted orders are given by:

$$\boldsymbol{k}_{x,ref,m} = \boldsymbol{k}_{x,inc} + m\frac{2\pi}{\Lambda_x}\hat{x} \tag{2.32}$$

$$\boldsymbol{k}_{x,trans,m} = \boldsymbol{k}_{x,inc} + m\frac{2\pi}{\Lambda_x}\hat{x} \tag{2.33}$$

$$k_x = \frac{2\pi}{\lambda} n \sin\theta \tag{2.34}$$

where $\boldsymbol{k}_{x,ref}$ is the *x*-component of the *k*-vectors of the reflected diffractive orders,

$\boldsymbol{k}_{trans}$ is the *k*-vectors of the transmitted diffractive orders, Λ_x is the period of the grating, n is the refractive index of the medium, $\hat{x}$ is the unit vector in *x*-direction and m is the diffractive order, e.g., $\pm 1, \pm 2, \pm 3$ .... Note that vectors are bolded whereas unbolded notations are the magnitudes of the vectors.

Substituting Eq. (2.34) into Eqs. (2.32) and (2.33), we have

$$n_{ref} \sin \theta_m = n_{inc} \sin \theta_{inc} - m \frac{\lambda_0}{\Lambda_x} \tag{2.35}$$

$$n_{trn} \sin \theta_m = n_{inc} \sin \theta_{inc} - m \frac{\lambda_0}{\Lambda_x} \tag{2.36}$$

which is always used to determine the existence of the diffracted orders of a grating and their directions. However, the amplitude of the diffracted orders cannot be worked out universally to a good agreement without more rigorous calculations, i.e., rigorous coupled wave analysis (RCWA) [27-29].

RCWA is commonly used in the design and analysis of various photonic devices with periodic structures by decomposing the incident wave into its constituent plane waves and then solving the scattering problems by matching the boundary conditions for each layer and each plane wave. It is particularly useful for studying light-matter interactions in nanoscale and microscale.

2.3 Refractive Index Sensors

A refractive index sensor measures the external perturbation, e.g., the change in substrate refractive index caused by concentration change of solutions. Other factors such as temperature, humidity as well as surface pressure could also modulate the

refractive index of the substrate. Whereas for acoustic sensors, one conventional working principle is that external changes such as ultrasound pressure, result in intrinsic perturbation such as variation of resonator dimensions, therefore result in a change in resonance. Optical sensors, based on their sensing mechanisms, can be placed into two categories: (1) metal-based plasmonic sensors and (2) dielectric-based photonic sensors. With consideration of the relevance to the thesis theme, this literature review limits its scope to only free-space optical sensors. Fiber-based optical sensors will not be discussed.

The performance of the sensors can be evaluated with their bulk responsivity and FOM. To avoid ambiguity, we use the term "responsivity" to refer to the changing rate in the measured signal with respect to a given change of refractive index, whereas we reserve the term sensitivity to refer to the detection limit of refractive index unit (RIU), or noise equivalent RIU. Therefore, this term is related to the responsivity and the noise level. Bulk responsivity is defined by

$$R_{bulk} = \frac{\Delta k_x/k_0}{\Delta n_s} \tag{2.37}$$

FOM is defined by

$$FOM = \frac{R_{bulk}}{FWHM} \tag{2.38}$$

And sensitivity is defined by

$$S = \Delta n = NEP/\left(\frac{dI}{dn_0 \sin\theta} \cdot R_{bulk}\right) \tag{2.39}$$

where k_x/k_0 denotes the normalized x-component of the wave vector, effectively

$n_0 \sin\theta$, n_s denotes to the refractive index of the sample, FWHM denotes full width half maximum of a dip or a peak, S and Δn denote the sensitivity of the system, NEP denotes the system noise level, $\frac{dI}{dn_0 \sin\theta}$ denotes the slope of the reflectivity and $\frac{dn_0 \sin\theta}{dn_s}$ denotes the bulk responsivity of the structure.

It is worth noticing that variables determining bulk responsivity and FOM are intrinsic to structure design. On the other hand, the term NEP is extrinsic as it is highly related to not only structure design but the experimental instruments and environment fluctuations. $\frac{dI}{dn_0 \sin\theta}$, which denotes the slope of the reflectivity, is inversely related to the FWHM. Thus, sensitivity is determined by NEP and FOM, which means both structure design and the experiment system.

2.3.1 Conventional Surface Plasmon Resonance Sensors

Surface plasmon resonance is a widely used and well-established metal-based plasmonic method for sensing applications [30, 31]. SPR is the resonant oscillation of electrons at the interface of metal and dielectric materials stimulated by incident light. Surface plasmons (SP) are surface electromagnetic waves propagating along the interface. Noble metal materials used mainly include Au and Ag, in some cases, also Cu [32, 33]. The wave vector of the SP propagating along the interface of semi-infinite metal and semi-infinite dielectric material excited by incident light with p-polarization can be expressed as

$$k_{sp} = \frac{\omega}{c}\sqrt{\frac{\varepsilon_1 \varepsilon_2}{\varepsilon_1 + \varepsilon_2}} \tag{2.41}$$

where ω is the angular frequency, c is the light velocity in vacuum, ε_1 and ε_2 are the relative permittivity of two media at the two sides of interface, e.g., metal and dielectric.

There are two types of configurations for SPR structures: the Kretschmann configuration [34] and the Otto configuration [35] as shown in Fig. 2.4(a) and 2.4(b), respectively. In the Kretschmann configuration, metal of appropriate thickness is deposited on top of a couplant, above metal is the analyte layer. To excite the SP at metal/dielectric interface, the incident angle of light, θ, must be above the critical angle satisfying:

$$\frac{2\pi}{\lambda} n_0 \sin\theta - k_{sp} = 0 \tag{2.41}$$

where n_0 is the refractive index of the dielectric material, θ is the angle of incident light and k_{sp} is the wave vector of the SP, which is determined by both the metal layer and the dielectric layer.

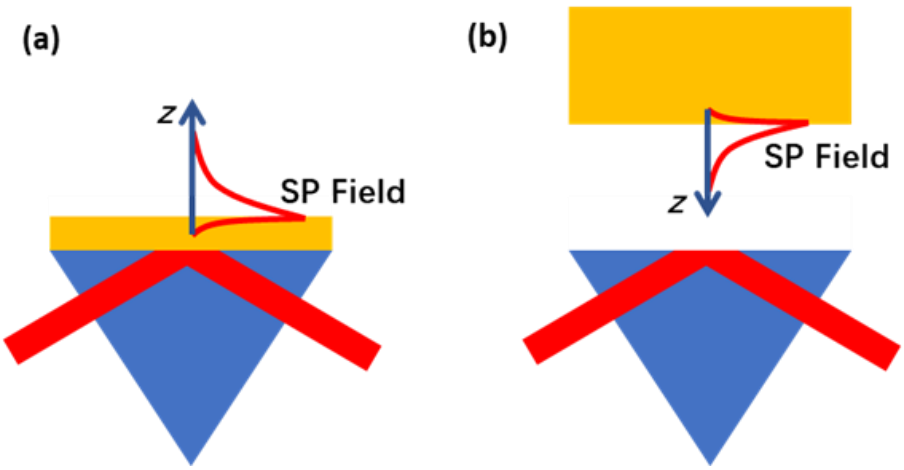

Fig. 2.4. (a) Schematic of the Kretschmann configuration. (b) Schematic of the Otto configuration.

In the Otto configuration, as shown in Fig. 2.4(b), the dielectric layer, which is usually the sensing region, is placed between the prism and metal. Incident light wave is totally internal reflected at the interface of prism and dielectric layer generating an evanescent wave at the surface. Surface plasmons are excited by the evanescent wave at the interface of the dielectric layer and the metal layer. In order to properly excite surface plasmons, the thickness of the dielectric layer has to be controlled precisely in the scale of nanometers, e.g., with a piezo actuator [36]. The dielectric layer also acts as the sensing region of the close structure, gas chambers or fluidic channels have to be manufactured, which further complicates the fabrication process. As shown in Fig. 2.5, the adjustable thickness of the dielectric layer gives the structure more degrees of freedom to excite SP at various wavelengths and angles and the parallelism between

the top surface and the gold chip is difficult to calibrate and affects the mode excitation efficiency.

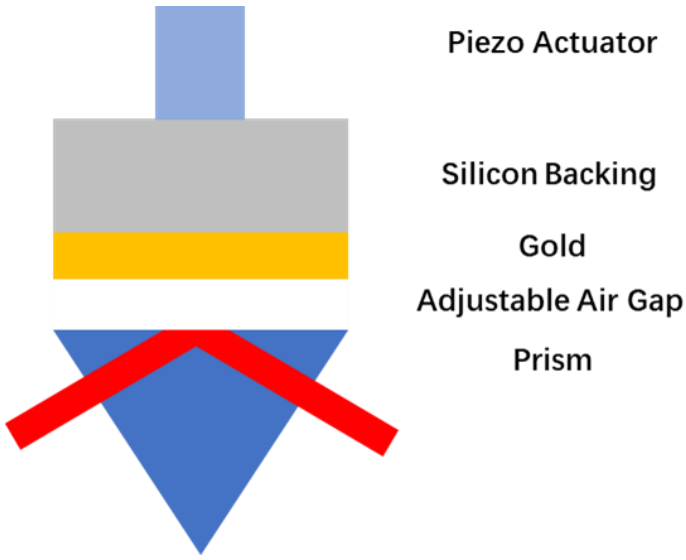

Fig. 2.5. Otto-configuration-based SPR sensor with adjustable thickness of the dielectric layer.

A hybridized Otto-Kretschmann SPR mode can be excited with a metal-insulator-metal (MIM) structure [37] with Fabry-Perot modes as shown in Fig. 2.6. With 50 nm gold as the first metal layer and 200 nm gold as the second metal layer and an adjustable air gap controlled by a piezo stage as the insulator, two hybridized modes can be excited where evanescent field exists at both the top and bottom surface of the air gap. The difference between the two hybridized SPR modes is that one mode has a phase shift of π in the air gap while the other does not. Therefore, the two modes are distinguished as the anti-symmetric mode and the symmetric mode [37].

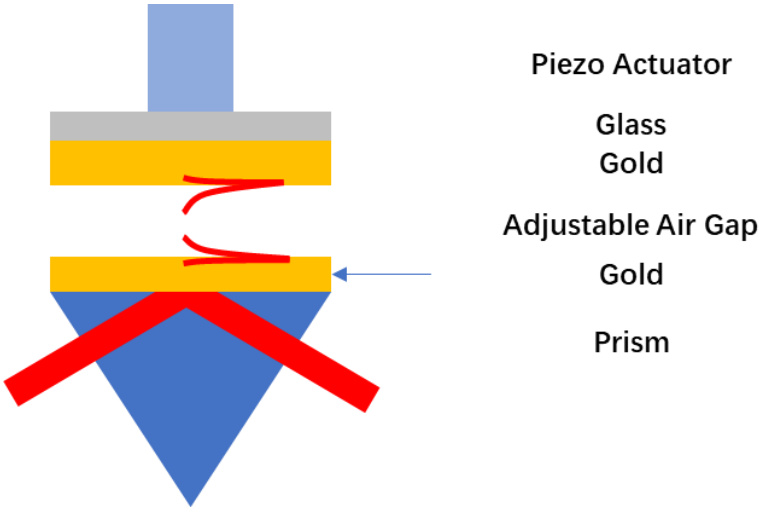

Fig. 2.6. Schematic of a metal-insulator-metal structure experimented.

Of the two, the Kretschmann configuration is more popular in most applications deriving from its refractive index sensing and acoustic sensing ability since it is without the meticulous control over the air gap that the Otto configuration needs for gap distance and parallelism. There are three main coupling mechanisms: prism coupling, objective lens coupling and metal grating (nanostructure) coupling. Objective lens coupling is mostly implemented for imaging and metal grating and nanostructure coupling could encounter a coupling efficiency issue and manufacturing difficulty [38, 39].

Prisms have been widely used to provide the required wavenumber to excite modes above the critical angle, e.g., SP modes or Fabry-Perot modes. Generally, depending on the measurand, there are several types of interrogation, e.g., intensity, angle [40], wavelength[11] and phase [41]. Conventional SPR devices are evaluated in various

sources of literature for performance metrics, e.g., responsivity, sensitivity and FOM comparison of different interrogation methods. Theoretically, angular interrogation SPR could yield a responsivity of 191 deg/RIU at 633 nm wavelength, whereas wavelength interrogation could yield a responsivity of 1000 nm/RIU, and intensity interrogation could yield a responsivity of 4000%/RIU [42]. It also shows strong dependence between the wavelength of the incident light and responsivity. An increase in wavelength could decrease angular responsivity but increase wavelength responsivity and intensity responsivity for a certain thickness of the gold layer [42]. This is because of the dispersion property of Au. As the wavelength increases from 500 nm, the imaginary part in the refractive index of Au increases quickly at a rate of 7.5 imaginary RIU/μm, therefore, the modulus of the refractive index increases. According to Ref. [39], the angular sensitivity, which is the partial derivative $\partial\theta/\partial n_a$, is inversely related to the modulus of Au refractive index, whereas the wavelength sensitivity $\partial\lambda/\partial n_a$ is related to the modulus of Au refractive index. Therefore, angular interrogation methods usually use 633 nm incident wavelength and wavelength interrogation methods usually choose higher wavelength up to 1550 nm.

Angular Interrogation Sensing

Conventionally, angular interrogation is done by rotating the laser source or rotating the prism, which is seemingly simple. However, it greatly increases the complexity of

the experiment and introduces extra mechanical errors. Utilizing a He-Ne laser at 633 nm, Ho et al. proposed a digital micro-mirror (DMD) as the interrogation probe, enabled angular interrogation with high signal-to-noise ratio (SNR) and relatively high dynamic range similar to Fig. 2.7 [43]. By modulating the DMD, multi-channel real-time detection was achieved with a noise equivalent sensitivity of $3.54 \times 10^{-6}\ RIU$. Bio-sensing applications have been realized with BSA/anti-BSA binding experiments. Apart from DMD, similar characterization of the angular interrogation system could also be achieved by a galvo mirror or a spatial light modulator (SLM) acting as the scanning device. Scanning with a galvo mirror can potentially results in slow a scanning speed, which depends on the mechanical property of the device, whereas for DMD or SLM, the system can compensate for the speed, since it is dependent on the refreshing rate of the device but they may suffer from the diffracted orders resulted from the finite pixel size, so the working distance can be long in order for the diffracted orders to fall off the aperture. One advantage with the DMD and SLM is that they can provide fast angle scanning and they have the ability to modulate the wavefront, which can make themselves a lens.

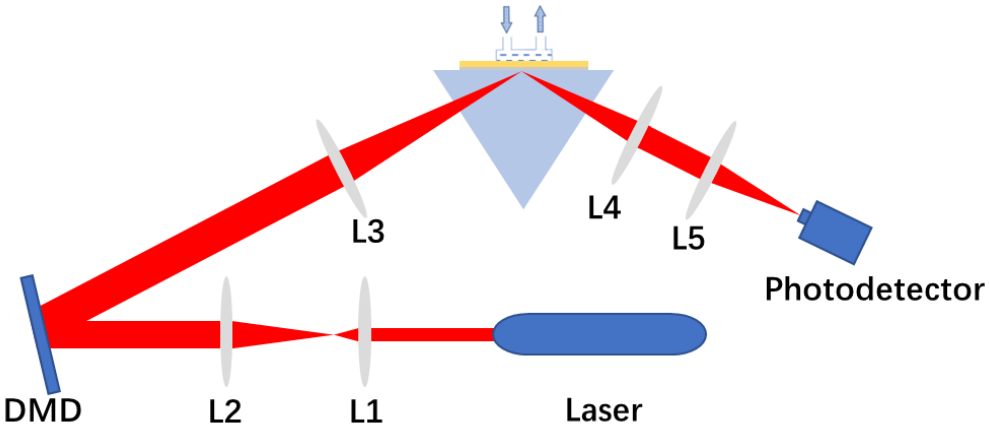

Fig. 2.7. Schematic of a typical angular interrogation SPR with a DMD as the scanning probe. The DMD is a digital micro-mirror and L1-L5 are lenses.

Wavelength Interrogation Sensing

Apart from angular interrogation, it is well established that wavelength interrogation draws considerable research interest [44] because, compared with angular interrogation, wavelength interrogation methods tend to have a more compact form without the angle scanning devices [45-47]. Wavelength interrogation could be realized with a broadband light source and a spectrum analyzer, or alternatively a tunable layer and a photon detector. In Ref. [48], Lu et al. demonstrated wavelength interrogation SPR and comparison with various plasmonic structures, e.g., Au of 50 nm thickness, Ag of 50 nm thickness and Au/Ag multilayer structure. The multilayer structure consisted of 3 pairs of 5 nm Ag and 10 nm Au stacking. It was shown that the FWHM is 90 nm for the Au resonator, 59 nm for the Ag resonator and 73 nm for the multilayer structure. The bulk responsivity ranges from 1816 to 4945 nm/RIU for

the Au resonator, from 2508 to 5548 nm/RIU for the Ag resonator and from 2022 to 5380 nm/RIU for the multilayer structure. Because the responsivity derived from the dispersion relation is related to the incident wavelength, the bulk responsivity of wavelength interrogation changes with resonance wavelength, which is related to the refractive index of the analyte. However, as the wavelength increases, the loss in gold increases, and the FWHM of the dip increases.

Phase Interrogation Sensing

A sharp phase change occurs at the resonance dip of the surface plasmons, and attempts have been made to achieve higher sensitivity with phase measurement [49-52]. Conventional phase measurement schemes utilize interferometry [51-55] or ellipsometry [9, 56, 57]. A sharp phase change can enhance the sensitivity to 10^{-7} and 10^{-8} regime [58, 59]. However, the trade-off is a narrow dynamic range. In Ref. [9], Wang et al. proposed a system where a trade-off between sensitivity and dynamic range could be achieved by varying the settings of the polarization components. Generally speaking, phase interrogation SPR tends to have higher sensitivity compared with wavelength interrogation and angle interrogation, albeit at the price of lower dynamic range. In [9], an electro-optic modulator (EOM) was used to modulate the polarization and a analyzer and a modulated light camera to detect the signal. The responsivity of the system is adjustable by varying the polarizer angle and analyzer

angle. The best sensitivity is on the order of 10^{-8} RIU. With a dynamic range of 10^{-2} RIU, the sensitivity of the system is on the order of 10^{-6} RIU.

Apart from the innovation in interrogation methods, attempts have also been made to achieve higher sensitivity or FOM by designing novel structures [6]. From the definition in Eq. (2.38), it can be seen that there are several approaches to boost sensitivity and improve responsivity: (i) increase light confinement, (ii) increase the responsivity. An increase in light confinement would increase the resonance quality factor (Q) and result in sharper resonance dip to achieve higher sensitivity and figure-of-merit.

2.3.2 Long Range Surface Plasmon Resonance Sensors

Long range surface plasmon resonance (LRSR), first reported by Sarid in 1981 [60], described a type of multilayer plasmonic structure inspired by conventional SPR sensors. The main difference is an additional dielectric layer inserted between substrate and metal layer as shown in Fig. 2.8. LRSPR has less energy enhancement inside the lossy metal compared with cSPR and more on the surface. Therefore, LRSPR has a longer penetration depth into the analyte resulting in higher sensitivity, bulk responsivity and FOM compared with cSPR with the same interrogation methods. Homola designed a LRSPR sensor consisted of 1200 nm spin-coated 6% Teflon AF and 24 nm thick Au layer working around 820 nm wavelength as shown and reported a sensitivity of $2.5 \times 10^{-8}\ RIU$ as shown and a bulk responsivity of 5.7×10^{4}

nm/RIU when investigated with wavelength-interrogation [61].

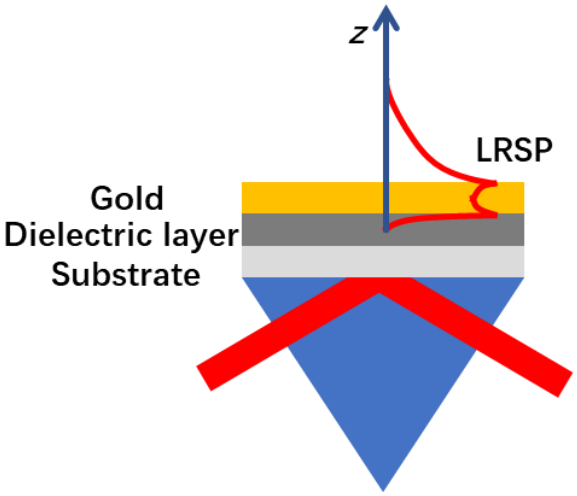

Fig. 2.8. A typical schematic of long-range SPR for sensing and its evanescent field.

2.3.3 Bloch Surface Wave (BSW) Sensors

Based on the same Kretschmann configuration as SPR sensors, one typical dielectric sensing scheme is Bloch Surface Wave (BSW) sensing. BSW can propagate at dielectric-dielectric interface [62] and has drawn extensive research interest for sensing applications with 1D photonic crystal structures[63, 64]. Compared with metal materials in SPR, the dielectric material in BSW has near-zero loss, which could significantly reduce the linewidth of the resonance dip, thus resulting in a higher FOM [65]. A typical BSW sensor consists of multiple bilayers of photonic crystal materials with designed thicknesses usually of λ/4 [66]. A typical schematic of an 8-layer BSW sensor is shown in Fig. 2.9. The excitation scheme is similar to that

of the SPR, which the mode can be coupled with a prism. In Ref. [66], six bilayers of 120 nm TiO_2 and 135 nm SiO_2 with a termination layer of 40 nm TiO_2 were used for aqueous sensing of NaCl solutions with refractive index varying from 1.3330 to 1.3482. The maximum bulk responsivity is up to 1933 nm/RIU with an FOM of 434 RIU^{-1}. Photonic crystals of 100-200 nm thick can easily be manufactured by E-beam evaporation or sputtering. However, for applications with higher wavelengths, i.e., 1550 nm, thicker layers of photonic crystals were needed, and the layers were prone to cracking and low yield due to residual strain inside.

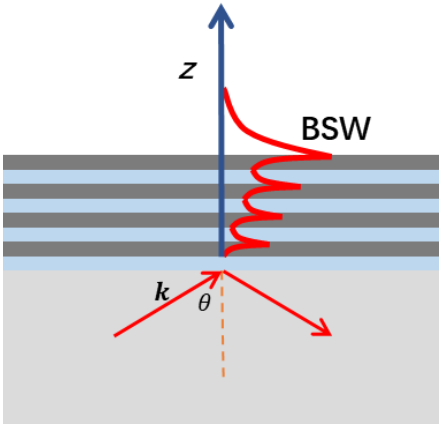

Fig. 2.9. A typical schematic of a multilayer structure with 8 stacked layers of photonic crystal structure that can excite BSW for sensing applications.

2.3.4 Nanostructure Enabled Localized SPR Sensors

In the preceding sections, homogeneous layered structures have been discussed. The main advantages of the said structures include high stability, convenient design and manufacturing. Most of the design could be done by Fresnel's equations, and

manufacturing could be done by sputtering and spin coating. The penetration depth of the SPR sensors varies from 200 nm to over 1000 nm [34, 67], which is desirable when sensing the bulk medium. However, for biomedical applications such as detection of monolayer protein [68], the penetration depth is larger than the size of most analytes, so the evanescent field only undergoes limited modulation. In this scenario, a smaller penetration depth is desired, so nanostructures are proposed to confine more energy close to the metal surface [6]. For the nanostructure to be discussed, the aim is to further increase the limitation on sensitivity and FOM. Metal patterns include nanoparticles and nanoholes including nanorods [69, 70], nanorings [71, 72], nanoprisms [73-75], nanowires [76], nanotubes [77] and etc [78]. Metal materials are noble materials that supports surface plasmons, e.g., Au, Ag [79] and novel 2D materials, e.g., borophene [80] and graphene [81]. The design and simulation of the said structures could be complicated, involving sophisticated programming or mature commercial methods, e.g., FEM, FDTD Solutions, COMSOL Multiphysics etc. Different metal and pattern combination could give varied results. Manufacturing methods usually include sputtering, various lithography technologies, e.g., DUV Lithography, electron beam lithography and nano-imprinting lithography for different feature dimensions, chemical vapor deposition (CVD), physical vapor deposition (PVD) and lift-off process. However, in terms of bulk responsivity and FOM, localized SPR sensors tend to have lower values than cSPR or LRSPR since the

latter two have more modulation from bulk analyte. Since cSPR and LRSPR have a higher Q and provided the evanescent field interacts fully with the change in refractive index, they are more sensitive. Metamaterials have lower bulk responsivity and FOM, but they can interact with the region where refractive index changes more efficiently.

2.4 Ultrasound and Photoacoustic Sensors

Photoacoustic imaging (PAI) is a fast-developing biomedical imaging tool with noninvasive and nonionizing capability enabled by acoustic sensors [5]. In the photoacoustic imaging process, acoustic sensors are used to detect acoustic waves generated by laser irradiated energy absorption of samples, typically biological ones. Combined with scanning methods, acoustic sensors can be utilized for Photoacoustic Imaging. For a long time, a piezoelectric-effect-based mechanism has been the dominant approach for detection of acoustic waves, which utilizes the piezoelectric effect within polarized materials like PZT and ZnO to convert energy between mechanical vibration and electric pulses. However, there is a trade-off between bandwidth and center frequency, both of which are critical metrics [5]. The center frequency determines sensitivity and acoustic penetration depth, whereas the bandwidth determines the detectable dynamic range. Lack of broadband sensitivity hinders the sensors' ability recover multiscale information [82]. Optical acoustic sensors have emerged as a novel approach to realize photoacoustic detection with

optical transparency, broad bandwidth and convenient device miniaturization and integration. There are fundamentally two approaches for acoustic waves to interact with optical sensors, the first of which is by modulating the thickness of the resonator, e.g., a Fabry-Perot Interferometer, the second by modulating the refractive index of the sensing analyte, e.g., SPR.

Generally speaking, a typical photoacoustic imaging system consists of two functioning beams with different working wavelengths to avoid cross talk, one excitation beam and one interrogation beam. The excitation beam is usually a pulsed laser focused onto the sample and therefore, generate the acoustic waves. The interrogation beam is usually a continuous wave laser with its measurement configuration tuned to maximum sensitivity to record the shift of resonance. Since the bandwidth of the photoacoustic signal generally exceeds tens of megahertz, data are collected with a fast oscilloscope or a DAQ card and are then processed by a computer to reconstruct the signal and image. To simply test the function of an optical detector, one could simply replace the excitation arm with an ultrasound transducer [83].

2.4.1 Fabry-Pérot Interferometer

A Fabry-Pérot (FP) interferometer is an optical cavity made of a spacer sandwiched between two reflecting mirrors. The reflecting mirror could either be a thin metal layer or a dielectric structure, e.g., 1D grating, meta surface or Bragg reflector.

The resonance condition of a FP mode is given by

$$2k_z d + \phi_1 + \phi_2 = 2m\pi, m = 1, 2, 3, \ldots \quad (2.42)$$

where $k_z = \frac{2\pi}{\lambda} n_s \cos\theta$ denotes the z-component of wave vector inside the spacer, d denotes to the thickness of spacer, ϕ_1 and ϕ_2 denote phase changes at the mirrors, m is a positive integer, λ is the incident wavelength and θ is the propagation angle inside the spacer.

It should be noted that ϕ_1 and ϕ_2 denote phase changes at the mirrors, which can be explicitly calculated with Fresnel's equations on reflection coefficients, e.g., Eqs. (2.19) to (2.22). ϕ_1 and ϕ_2 are the phase of the reflection coefficients at the interface of two semi-infinite media, i.e., the metal and the cavity. Therefore, the phase terms in Eq. (2.42) are related to permittivity of all the mirrors and cavity material.

It can be concluded from the resonance condition that the FP mode is sensitive to changes of light path, e.g., spacer thickness and refractive index, enabling it working as both an acoustic sensor [84] and refractive index sensor [37, 85, 86]. However, because of its closed form, in order to employ the significant refractive index responsivity in free space, a microfluidic channel has to be fabricated to introduce analyte into the spacer with sophisticated manufacturing process. It is easier to implement a Fabry-Pérot interferometer for refractive index sensing applications in optical fibers [87-89].

On the other hand, Fabry-Pérot (FP) cavities have been well-established in

photoacoustic sensing [84]. Other than their generic resonance properties, the sensing capabilities of the Fabry-Perot structures hugely relies on material properties of the spacer as well. Materials with smaller Young's Modulus have been favored, e.g., PDMS [90, 91], Parylene [84] as they could offer larger thickness response given the same ultrasound pressure. However, a lower Young's modulus may limit the working frequency and bandwidth since the sound velocity inside the structure is low, therefore the wavelength for a given frequency is shorter, thus limiting the bandwidth [84].

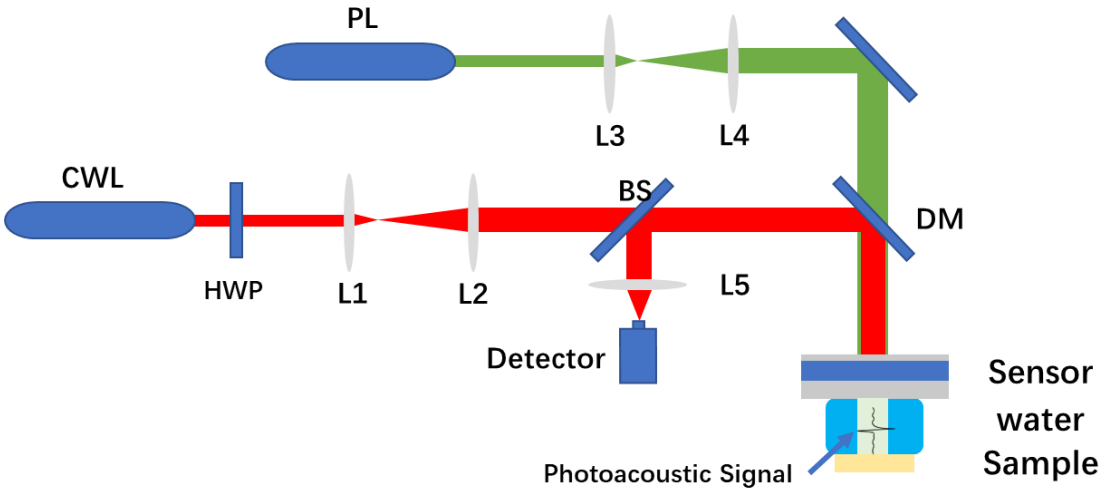

Fig. 2.10. A typical system diagram of optical transducers with normal incidence operating with reflection-mode excitation. PL: pulse laser; HWP: half waveplate; CWL: continuous-wave laser; DM: dichroic mirror; BS: beamsplitter. L1-L5 are lenses. Lenses L1-L2 and L3-L4 are lens pairs for beam expansion purposes for continuous-wave lase and the pulse laser.

Fig. 2.10 shows a typical photoacoustic sensing and imaging system for a Fabry-

Pérot working in backward reflection mode where the excitation beam (marked in green) and the interrogation beam (marked in red) are on the same side of the sample and the photoacoustic signal detected is travelling backward towards the sensor. For Fabry-Pérot structures, spectral interrogation is commonly used, therefore, CWL is a tunable continuous-wave laser and in order to calibrate for wavelength drift, the slow-varying component of the detector signal is connected to CWL for wavelength locking and fast-varying signals are recorded for sensing and imaging applications [92-96].

This system is applicable to other types of thin-film photoacoustic transducers with normal incidence and of high transparency. It can be seen that the other imaging modalities can be integrated into the system, e.g., microscopy or optical coherence tomography, to conduct measurements in parallel [97, 98].

2.4.2 Refractive Index Sensors for Photoacoustic Sensing and Imaging

As stated above, during propagation, mechanical waves can change the local pressure, therefore resulting in a small change in local refractive index. Therefore, sensors conventionally used for refractive index sensing can be transferred for photoacoustic sensing.

SPR is used in acoustic sensing as an extension to its refractive index sensing ability [16, 30, 31, 99, 100]. The basic working principle as an acoustic sensor is the same as a refractive sensor since, when acoustic waves propagate to the surface of a

surface plasmon resonator, the refractive index on the surface is modulated by the acoustic pressure. When used as an acoustic sensor, the modulation depth of the refractive index is comparatively low, therefore, high excitation power or low-noise-high-gain amplifier is needed. The bandwidth of the excited acoustic wave is wide; therefore, a fast sampling rate and broad bandwidth are demanded for the sensors. Thus, intensity and phase interrogation are favored in this field [31]. A similar working mechanism could also see BSW sensors as optical acoustic sensors [101, 102]. Fig. 2.11 shows a typical system diagram of SPR sensors for photoacoustic sensing and imaging. The excitation arm consists of a pulsed laser, an objective lens for focusing the laser beam and a pair of lenses for beam expansion for a smaller focus. This typical system is applicable to not only SPR but also BSW or critical angle sensors for photoacoustic refractive index since the excitation angles of the modes are similar [103, 104]. The interrogation beam is similar to the one used for refractive index sensing. Only the bandwidth of the photodetector should be higher. The penetration depth of the SPR is a few hundred of nanometers to 1 μm depending on the wavelength and mode angle, which is effectively the sensing field that relates to the bandwidth performance of the sensor and is on the same order as the acoustic wavelength in *z*-direction. With SPR working as an acoustic sensor in the Kretschmann configuration, theoretically, the bandwidth could be in the range of GHz [31]. In recent studies conducted by Song et al., a bandwidth of 173MHz was

experimentally demonstrated for a polarization-differential SPR acoustic sensor with a noise-equivalent pressure below 500 Pa where p-polarization serves as an interrogation beam as it experiences a phase change when SPR is excited and s-polarization serves as a reference with a constant phase [105].

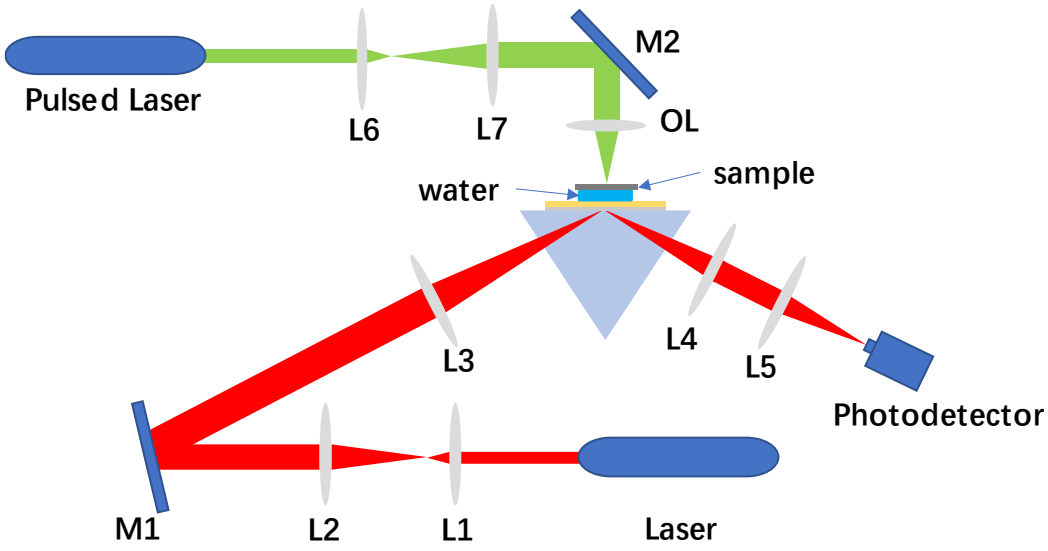

Fig. 2.11. A typical system diagram of the Kretschmann-configuration SPR sensor for photoacoustic sensing and imaging applications. The red beam represents the interrogation arm, and the green beam represents the excitation beam. The sample is mounted on top of the sensor with water between them forming liquid contact allowing acoustic waves to propagate.

Photoacoustic imaging applications are enabled in two ways, (i) the samples are placed on a 3-dimensional stage within a fixed optical system, (ii) the beam is

scanning with galvo mirrors [10, 13, 84, 96]. A scan with the sample on a motorized stage seems the straightforward solution. However, a complete scan can take up to hours because of the scanning speed. With a galvo mirror, the scanning time can be significantly reduced. To further increase the speed, the scanning can be done by a DMD or SLM to modulate the wavefront. However, this may sacrifice some of the energy and focus size.

As the modulation of refractive index induced by acoustic waves happens significantly only for a thin layer at the interface due to acoustic velocity mismatch, there could be more sensitivity for localized plasmonic sensors realized by meta surface. Zayats et al. demonstrated a plasmonic meta-surface excited with attenuated total internal reflection (ATIR) configuration, i.e., a prism, could yield an improvement with an order of magnitude over conventional SPR [106]. However, the experiment only demonstrated sensing applications. In photoacoustic imaging applications, consistency of response is required across the working area, which is relatively difficult for meta-surface sensors because of imperfect structure profiles. Careful calibration may be required over the whole active area.

Chapter 3 Refractive Index Sensing Analysis with High-Aspect-Ratio-Grating-based Fabry-Pérot Resonator

3.1 Introduction

Optical methods for refractive index sensing have wide applications in many fields, e.g., biomedicine [21, 107-110] and chemical analysis [45, 111-113] for label-free detection. For optical methods, classified based on the operating principle, there are resonant detection and non-resonant detection [106]. Non-resonant detection is based on meta-materials for its angle- or wavelength-dependent reflectivity [106, 114]. A resonant operating principle is to translate the perturbation of refractive index in the sample to a shift in resonance condition [115, 116]. Then, this shift in resonance condition can be reflected by a change in the resonant angle, wavelength and intensity [45, 117, 118]. Some techniques monitor phase and polarization rather than intensity for greater sensitivity [21, 24, 41].

To evaluate and compare the performance of different sensing mechanisms, bulk responsivity and FOM are introduced. In this thesis, the term “responsivity” is to refer to the change in measured quantity, e.g., angle, intensity, phase, with respect to a change in measurand, e.g., acoustic pressure, and in this thesis, refractive index, whereas the term “sensitivity” is reserved for the noise-equivalent minimum

detectable change of refractive index in the unit of refractive index unit (RIU). Thus, sensitivity is jointly determined by responsivity and noise level inside the system. Bulk responsivity and FOM are given by:

$$R_{bulk} = \frac{\Delta k_x / k_0}{\Delta n} \tag{3.1}$$

$$FOM = \frac{R_{bulk}}{FWHM} \tag{3.2}$$

where $\Delta k_x / k_0$ denotes the normalized *x*-component of the wave vector, effectively $n_0 \sin\theta$ with n_0 the refractive index of the substrate, and θ the incident angle, and FWHM denotes full width half maximum of a dip or a peak.

Generally speaking, high bulk responsivity R_{bulk}, narrow FWHM and high FOM are desired. There have been efforts made to increase the responsivity or narrow the FWHM with plasmonic sensors based on surface plasmon resonance (SPR) [21, 108, 111], long-range SPR [119], and photonic sensors, e.g., Bloch surface wave (BSW), i.e., based sensors photonic sensors [120] and whispering gallery mode (WGM) based sensors, e.g., ring resonators [121]. For SPR and BSW sensors, they can be excited conveniently with prism-coupled attenuated total reflection configuration, i.e., the Kretschmann configuration. These approaches allow label-free detection of proteins, viruses and various molecules found in human body that are indicative in disease diagnosis and treatment with high precision and sensitivity, but a trade-off exists for a given structure where a high quality factor (Q) is associated with poor responsivity [115]. It has been illustrated that strong coupling associated with high responsivity

corresponds to a low Q, which can be encapsulated by the transmission line resonant circuit model treating the analyte as an external load [115]. Therefore, the overall FOM does not change a great deal, so a sharp response is associated with a small change in the position of the resonance, i.e., low responsivity. One way to get around this trade-off is to design a resonator where the analyte is an intrinsic part of the resonator rather than just an external load.

With this consideration in mind, an open grating structure was theoretically analyzed with RCWA simulations [122]. In the structure, a Fabry-Pérot (FP) resonator was formed with the analyte and diffraction grating between n a thin gold layer and the analyte medium, therefore, the analyte becomes an intrinsic part of the resonator, and the trade-off between Q, i.e., FWHM, and responsivity is broken. In this chapter, it is demonstrated with experimental data that high-aspect-ratio-grating based FP (HARG-FP) can support high FOM and high Q with practical fabrication and real-world material properties. Therefore, with inevitable flaws and imperfections in the manufacturing process, the sample can still achieve performance that is far better than any prism coupled resonators. Moreover, equivalent transmission line resonant circuit model and Smith chart of the structure are proposed to give more intuition regarding the physical mechanisms of improved performance.

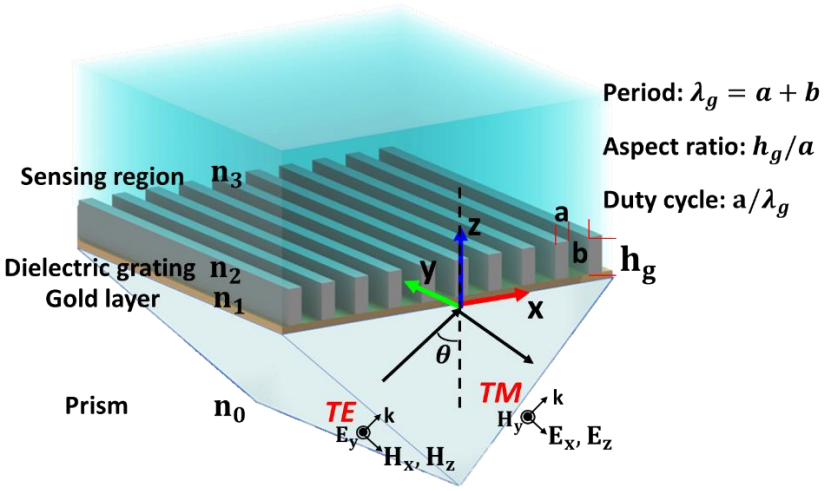

Fig. 3.1. Diagram of the grating structure of the Kretschmann configuration where λ_g is the grating period, a is width of the grating, b is the width between gratings and h_g is the height of the grating.

Fig. 3.1 shows the proposed HARG-FP resonator with sub-wavelength grating grown on top of a thin gold layer and its corresponding coupling mechanism, i.e., the Kretschmann configuration. A prism is used to couple the light with an angle of incidence above the critical angle. The structure is investigated in both simulation and experiment with both transverse magnetic (TM) and transverse electric (TE) polarizations. The prism-based coupling mechanism is also commonly used to excite conventional SPR modes, therefore, a direct comparison can be drawn experimentally between SPR and HARG-FP resonators. In the comparison, SPR resonators of a single 48-nm-thick Au layer were used as a benchmark. The SPR was chosen because its performance is well established and a comparison within the same system

eliminates the effect of system bias in terms of noise level and sensitivity.

Experimental results of the HARG-FP show a 44-fold improvement in FOM over SPR and suggest ultra-sensitivity. Theoretical analysis also suggests that the structure has huge potential in terms of label-free biosensing and chemical analysis.

3.2 Explanation of the Physical Mechanisms

The structure under investigation is an FP resonator based on an open grating. Generally speaking, the structure comprises a metal layer and a dielectric grating layer on top. In this analysis, gold is used as the metal material and polymethyl methacrylate (PMMA) is used as the dielectric material. Gold is chosen as it can provide adequate performance with sufficient stability against oxidization and PMMA is a commonly used lithography resist with sufficient chemical stability. A transmission line resonant circuit model and Smith charts are used to give new intuition and propose a layer-wise explanation of the physical mechanism. Responsivity is analysed in terms of in-grating and out-grating responsivity to represent that from FP mode inside the cavity and evanescent field of the FP mode in the liquid.

3.2.1 Overview of the Fabry-Pérot Resonance based on High-Aspect-Ratio Open Grating

The theoretical analysis starts with rigorous coupled wave analysis (RCWA) of the

proposed structure. The optimum structure thickness of the gold layer for different polarizations is first investigated. Of the two parameters determining the FOM of the structure, the thickness of the gold layer mainly affects the full width at half maximum (FWHM) rather than the bulk sensitivity. Therefore, it is desirable to have a thickness with sharp FWHM. The investigation is carried out by varying the thickness of the gold layer with a fixed dielectric FP layer of 1 μm thick. The substrate of the structure is glass with a refractive index n_{glass} of 1.52, and the superstrate is assumed to be water with a refractive index n_{glass} of 1.33. The results are shown in Fig. 3.2(a) for TM and Fig. 3.2(b) for TE, respectively.

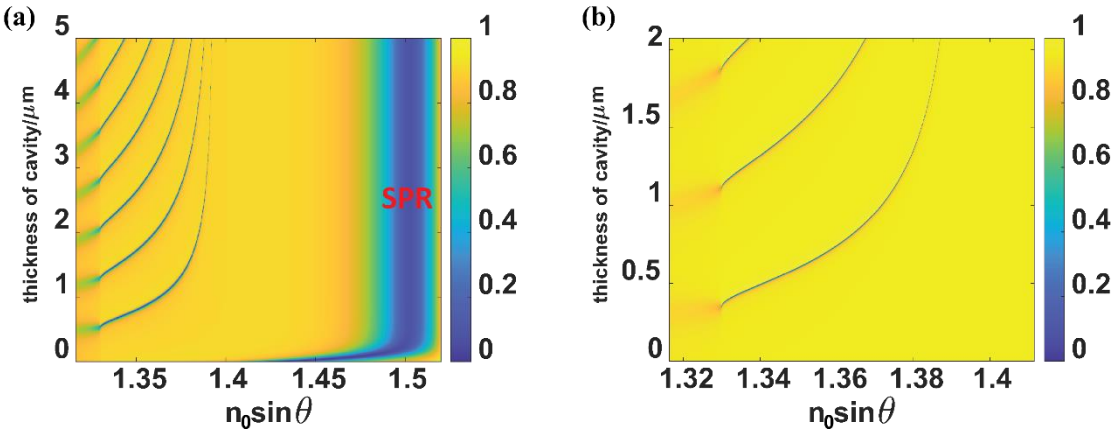

Fig. 3.2. Reflectivity for HARG-FP with (a) TM polarization and (b) TE polarization.

For the gold layer, optimum thickness for TM is 48 nm, whereas that for TE is 38 nm at an interrogation wavelength of 632 nm. It might be confusing that the optimum

thickness of HARG-FP is quite close to that of the conventional SPR. In the structure with TM polarization, SPR exists as marked in Fig. 3.2(a) but has little sensitivity since the sensing area is in the grating.

However, the excitation angle of HARG-FP does not correspond to SPR excitation within the structure. Then, reflectivity can be calculated with respect to the incident angle and thickness of the dielectric grating layer as shown in Fig. 3.2. From the diffraction equation of the grating, it can be concluded that the dielectric layer only supports a single dominant Bloch mode. Under this circumstance, simplification can be applied.

3.2.2 Effective Permittivity and Refractive Index of the Grating Layer

When the structure supports a single dominant Bloch mode inside the grating layer, analysis of the grating can be simplified by modelling the grating layer as an equivalent uniform layer with an effective refractive index (n_{eff}). This is the regime where the effective medium approximation (EMA) is valid for the present structure. Originally in studies of composite materials, EMA models macroscopic properties. Here, EMA is used to model effective permittivity and refractive index. With the help of EMA, it is possible to transform complicated RCWA calculations to transmission line model with less calculation resources while retaining an acceptable error. Three formulae for calculating n_{eff} are considered, i.e., weighted average permittivity,

Bruggeman's model and Maxwell-Garnett equation. The weighted average permittivity equation is shown in Equation 3.3.

$$\varepsilon_{eff} = (1 - c_i) \cdot \varepsilon_b + c_i \cdot \varepsilon_i \tag{3.3}$$

where FF is the fill factor, and ε_s is the permittivity of the filled medium (liquid) and ε_g is the permittivity of the grating material.

This approach is straightforward and helpful in terms of coarsely estimating the position of the dips.

Equation 3.4 shows the Bruggeman's model of the effective medium approximation.

$$\varepsilon_{eff} = \frac{1}{4}\left(H_b + \sqrt{H_b^2 + 8\varepsilon_s\varepsilon_g}\right), H_b = (2 - 3c_s)\varepsilon_g - (1 - 3c_s)\varepsilon_g \tag{3.4}$$

where ε_{eff} is the effective permittivity of the grating structure, c_s is the fill factor, and ε_g is the permittivity of the filled medium (liquid) and ε_s is the permittivity of the base material and grating, assuming grating is of the same material as the base material.

And Equation 3.5 shows the Maxwell Garnett (MG) equation [123, 124] of the effective medium approximation.

$$\varepsilon_{eff} = \varepsilon_g \frac{(\varepsilon_s + 2\varepsilon_g) + 2f(\varepsilon_s - \varepsilon_g)}{(\varepsilon_s + 2\varepsilon_g) - f(\varepsilon_s - \varepsilon_g)} \tag{3.5}$$

$$n_{eff} = \sqrt{\varepsilon_{eff}} \tag{3.6}$$

The EMA determined the refractive index of the dielectric layer. Therefore, the resonance angle was determined. A validity comparison of the three formulae was

carried out by comparing the calculated resonance angles with ground truth (results from RCWA) with different refractive indices of the grating and different fill factors. The refractive index of the grating varies from 1.34 to 1.7 with a step of 0.05 and the fill factor varies from 10% to 90% with a step of 5%. The deviation of the resonance angles from RCWA results are shown in Fig. 3.3. The orange line is for the Bruggeman equation, the yellow line is for the Maxwell-Garnett equation and the purple line is for the weighted average equation.

With both TM and TE polarizations, three formulae can offer close approximation to rigorous analysis while consuming much less computation power compared with RCWA. Of the three, Bruggeman and Maxwell-Garnett generally outperforms the weighted average method by a factor of three. In the following discussion, Maxwell-Garnett model is used to approximate the effective medium.

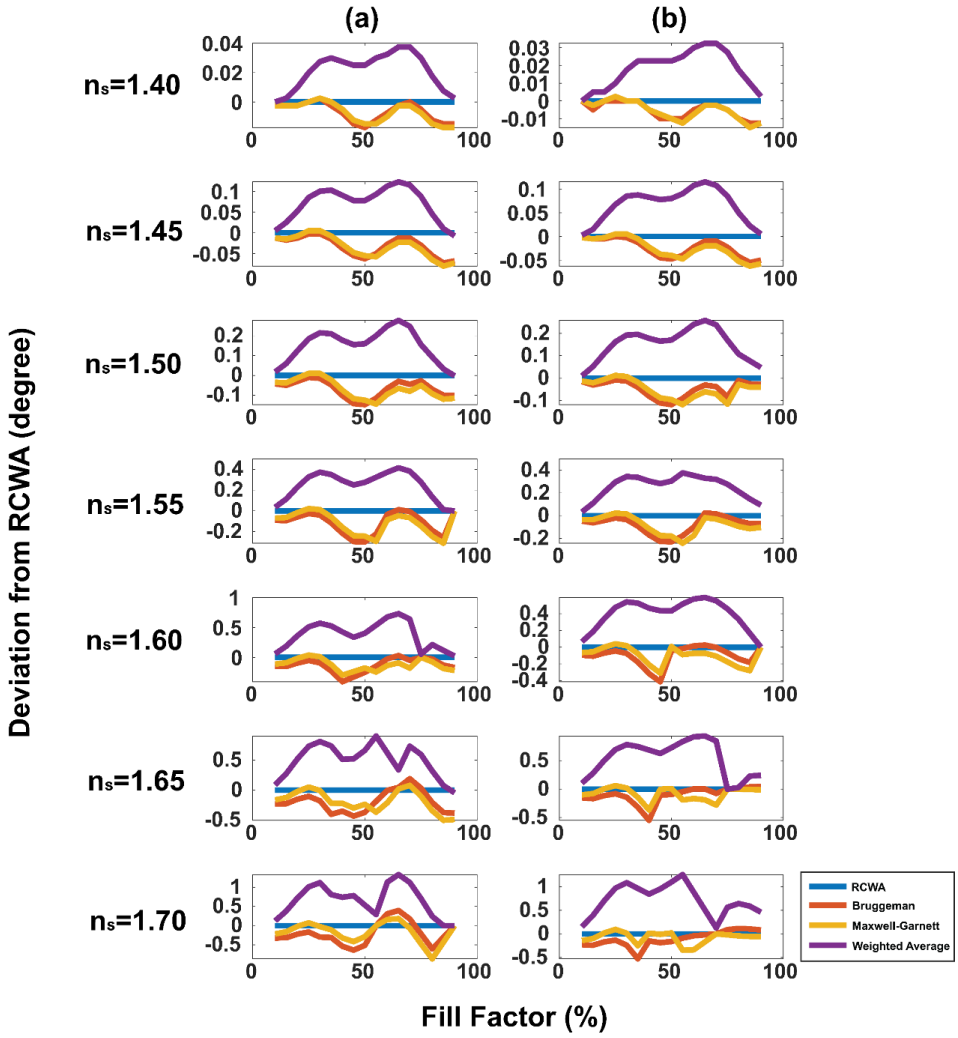

Fig. 3.3. Deviation of the resonance dip angles calculated with three effective medium approximation from RCWA calculations with sample refractive index varying from 1.40 to 1.70 and fill factor varying from 10% to 90%. Column (a) is TM polarization and (b) is TE polarization.

3.2.3 Transmission Line Model of HARG-FP

With EMA, all layers inside the HARG-FP can be considered homogeneous. Therefore, their characteristic impedance for TM and TE polarization are given by

[125]

$$Z_{TM} = \sqrt{\frac{\mu}{\varepsilon}} cos\theta, \;\; Z_{TE} = \sqrt{\frac{\mu}{\varepsilon}} \frac{1}{cos\theta} \tag{3.7}$$

where μ denotes permeability, ε denotes effective permittivity of the material and θ denotes the incident angle of investigation laser.

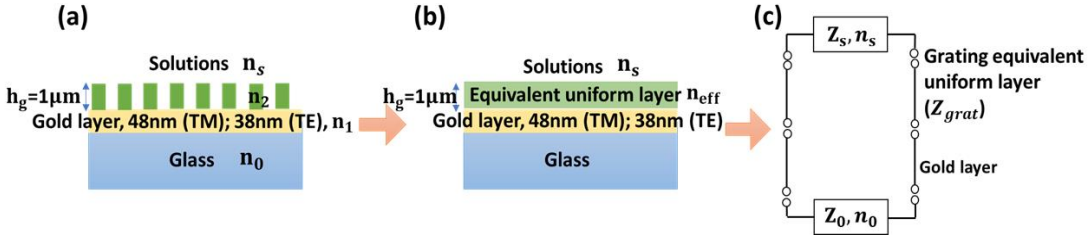

Fig. 3.4. (a) The high aspect ratio grating structure; (b) structure with equivalent uniform layer approximation; (c) transmission line model of the high aspect ratio grating structure.

Since all layers in the equivalent structure are homogenous, the transmission line model is applied to gain some insight [115]. Fig. 3.4 shows the schematics of the structure, its equivalent structure and equivalent transmission line circuit. Each homogeneous layer constitutes a two-node transmission line, and the sample layer is the load of the transmission line.

The transmission line circuit in Fig. 3.4(c) is formed where Z_0 and n_0 are characteristic impedance and refractive index of the prism, and Z_0 and n_0 are those of the sample.

In a transmission line circuit, reactance X_s and structure resistance R_s are two

factors affecting the resonance. The resonance condition is satisfied when the reactance in the circuit is cancelled out, which is $X_s = 0$, and thus k_x is real. At resonance position, the full width half maximum (FWHM) of the dip is given by:

$$\Delta k_x = 2(dk_x/dX_s)R_s|_{k_x=k_{sp}} \tag{3.8}$$

And Q factor is given by:

$$\mathrm{Q} = \frac{k_{sp}\frac{dX_s}{dk_x}}{2R_s} \tag{3.9}$$

Therefore, the FOM is given by:

$$FOM = \frac{\frac{dk_x}{dn_s}}{\Delta k_x} = \frac{\frac{dk_x dX_s}{dX_s dn_s}}{2(dk_x/dX_s)R_s} = \frac{dX_s}{dn_s}\frac{1}{2R_s}|_{k_x=k_{sp,o}} \tag{3.10}$$

In this chapter, the Q factor and FOM of the resonance are calculated with the transmission line model. The results are compared with RCWA for verification of the model. Fig. 3.5(a) and 3.5(b) are SPR Kretschmann configuration and approximated uniform layer structure, respectively. Fig. 3.5(c) is the structure reactance X_s at various k_x and n_s of the Kretschmann configuration. Fig. 3.5(d) and 3.5(e) are the plots of X_s at various k_x and n_s of grating structure at TM and TE modes, respectively. The position where $X_s = 0$ is the position satisfied resonance condition (as shown in red dashed line).

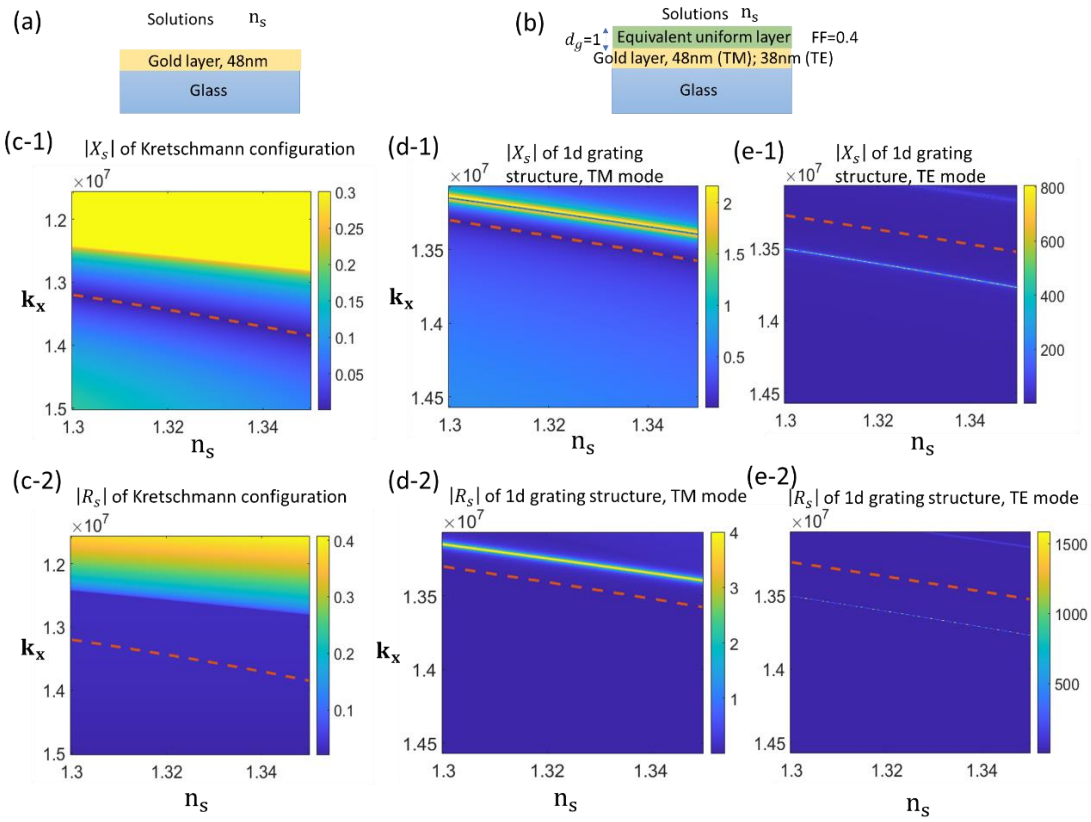

Fig. 3.5. (a) and (b) are SPR Kretschmann configuration and approximated uniform layer structure, respectively. (c) is the structure reactance X_s at various k_x and n_s of the Kretschmann configuration. (d) and (e) are the plots of X_s at various k_x and n_s of grating structure at TM and TE modes, respectively. The position where $X_s = 0$ is the position satisfied resonance condition (as shown in red dashed line).

Table 3.1 shows a detailed comparison of FOM and Q factor between SPR, TM and TE samples calculated by both transmission line model and RCWA. $\frac{dk_x}{dn_s}$ in RCWA results, which is the dip *k*-vector movement with respect to the change in the refractive index of the sensing region, are calculated with a small change in $\boldsymbol{n_s}$ of

0.001. FWHM of the TM dip is approximately $1/27$ of SPR dip, while TE mode $1/168$. The responsivity in transmission line model is predicted from the gradient of curve X_s vs k_x, while in RCWA model it is calculated twice to get two corresponding k_{sp} values, therefore, there is deviation between the results calculated from these two methods. For results of the grating structure, the deviation also comes from the approximation of the uniform layer.

Table 3.1 Comparison between SPR, TM and TE.

The FOM are calculated at $n_s = 1.33$.

		FOM $= \frac{\mathrm{d}X_s}{\mathrm{d}n_s}\frac{1}{2R_s}\|_{k_x=k_{sp}}$			Q Factor
Transmission Line Model		dX_s/dn_s	R_s	FOM	Q $= k_{sp}\frac{dX_s}{dk_x}/2R_s$
	SPR	1.88	0.03	31.33	33.19
	Grating TM	12.48	0.014	445.71	908
	Grating TE	292.31	0.053	2757.64	6159
RCWA ($\Delta n_s = 1.334 - 1.33 = 0.004$)		FOM $= \frac{\mathrm{d}k_x}{\mathrm{d}n_s}/\Delta k_x$			Q Factor
		$\frac{\Delta k_x/k_0}{\Delta n_s}$	FWHM $(\Delta k_x/k_0)$	FOM	Q $= k_{sp}/\Delta k_x$
	SPR	1.1695	3.93×10^{-2}	29.77	36.51
	Grating TM	0.6710	1.55×10^{-3}	433.70	881.46
	Grating TE	0.6359	2.33×10^{-4}	2724.11	5878.82

In this section, the effective medium approximation has been applied to the grating layer with n_{eff} calculated with Maxwell-Garnett equation. Then the structure was transformed into an equivalent transmission line model. The result of approximation shows excellent agreement compared with the rigorous analysis.

3.2.4 Smith Chart Representation of the HARG-FP

Besides the comparison between the transmission line model and RCWA analysis, the Smith chart has been utilized to reveal the effect of each layer for the HARG-FP and different polarizations. With the implementation of the Smith chart, phase and amplitude change in reflectivity can be apparent and separated since the nature of the Smith chart determines that the length from origin of the chart marks the modulus of reflectivity and the angle difference marks the phase shift of the reflectivity.

The well-established case of the SPR sensor is examined first. Fig. 3.6 shows the path along the Smith chart for detection of a refractive index change of 4×10^{-3} varying the thickness of the gold layer from 0 to 60 nm. The solid blue path shows the reflectivity change for refractive index of 1.33 and the dashed red path is that for refractive index of 1.334. The incident angle investigated for each thickness is set to the left half height angle for 1.33, which is $69.33°$. The yellow dot on the circumference marks the situation without a gold layer. There is a small difference in phase between refractive index of 1.33 and 1.334 since the incident angle is above the critical angle. The metal layer serves as an amplifier that magnifies this small

phase shift and thus gives a different reflectivity. In Fig. 3.6, red, green, blue, magenta and black represent the gold thickness of 12, 24, 36, 48, 60 nm, respectively. It can be drawn from the figure that 30 nm thick gold layer gives the largest phase shift for the given refractive index change, whereas 48 nm gives the largest change in reflectivity.

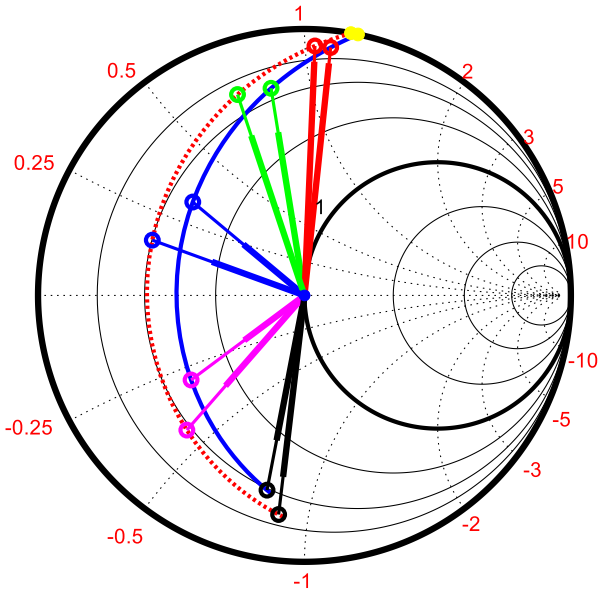

Fig. 3.6. The Smith Chart showing the sensing process of conventional SPR sample with the thickness of the gold layer being 12 (red), 24 (green), 36 (blue), 48 (magenta) and 60 (black) nm and change of refractive index from 1.33 (blue solid line) to 1.334 (red dashed line). Thick lines from the center, marking the reflectivity is the square of the respective thin lines, marking the reflection coefficient.

Similar procedures are followed when investigating the HARG-FP modes with TM and TE polarization. In the analysis, a 240 nm wide grating with a period of 600 nm and refractive index of 1.49 are used. The sensing process relating to TM modes are shown in the Smith chart in Fig. 3.7, which shows the reflectivity. The process is demonstrated by the paths marked in the Smith chart. The red and yellow paths around the circumference of the circle show the process where a pure grating with thickness increases from 0 up to 1 μm. As the incident angle is beyond the critical angle, the reflectivity is close to 1 when there is no gold layer. It should be noted that the analysis was conducted with RCWA, so the small deviation of the calculated reflectivity from unit reflectivity is caused by grating diffraction scattering into propagating modes. Then, a gold layer with thickness increasing from 1 nm to 60 nm was inserted as a coupling layer to modulate the reflectivity to make the reflected intensity vary close to resonance. The curves represent the reflectivity locus as the structure changes, the underlying impedance values, however, correspond to the impedance of a uniform structure with the same reflectivity.

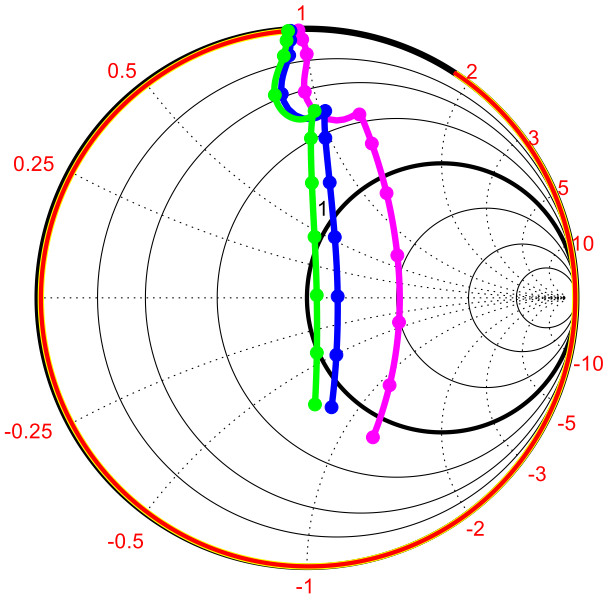

Fig. 3.7. The Smith Chart showing the sensing process of high aspect-ratio grating based plasmonic TM sensor with the thickness of the gold layer varying from 0 to 60 nm with steps of 6 nm and change of refractive index from 1.33 (green solid line) to 1.3304 (magenta solid line). The blue solid line represents the situation where the refractive index of the grating layer is not modulated and that of the superstrate is modulated from 1.33 to 1.3304. This allows separation of the different sensing mechanisms.

The structure was filled with liquid with refractive index of 1.33 which is then increased by 4×10^{-4} to 1.3304. The green curve marks the refractive index of the liquid being 1.33 and magenta 1.3304. The spots on the line represent changes in gold thickness of 6 nm starting from 0 nm therefore the last point is 60 nm. The optimum thickness for the maximum reflectivity change with refractive index was 48 nm. With

a grating layer of 1 μm thickness, the FWHM is 1.550×10^{-3} and bulk responsivity is $0.6807\ RIU^{-1}$. The FOM is 439.4.

Another case was considered where the viscosity and surface tension prevent the liquid from filling the gaps between the grating. In this case, internal perturbation and external perturbation were separated by uniform layer approximation. In the meantime, this case can reveal the relative effect of the index change within the grating and index change outside. To this end, the blue path in Fig. 3.7 was calculated, where the refractive index within the grating structure is 1.33 and the index outside is 1.3304. The FWHM is 1.550×10^{-3} and bulk responsivity is $0.1512\ RIU^{-1}$. The FOM is 112. The responsivity is reduced to 25%, but there is still substantial responsivity even if the impedance of the grating layer does not change. This indicates that approximately 75% of the refractive index sensitivity arises from perturbation inside the grating and the rest from external perturbation. For an unchanging grating, the FOM is 112 which is still 3 times more than the case of the conventional SP. This also indicates that even a homogeneous layer can form a reasonable sensor to detect, say, protein binding.

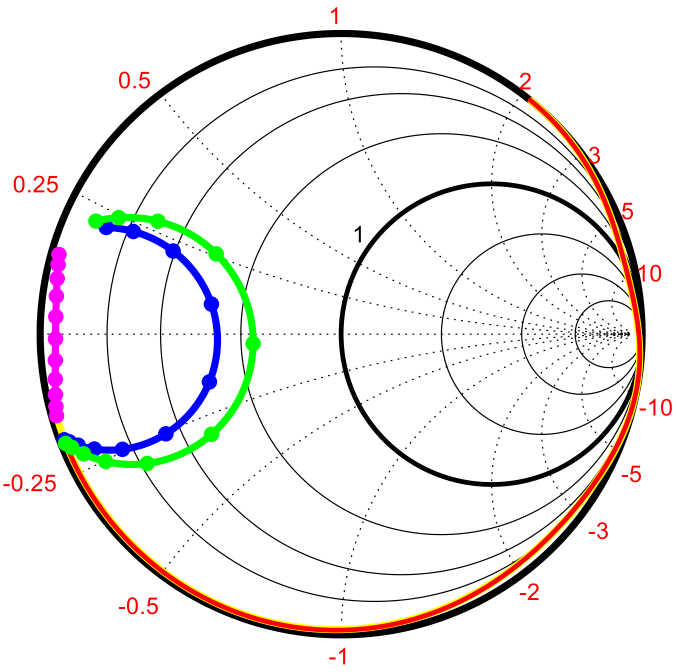

Fig. 3.8. The Smith Chart showing the sensing process of high aspect-ratio grating based plasmonic TE sensor with the thickness of the gold layer varying from 0 to 60 nm with a step of 6 nm and change of refractive index from 1.33 (green solid line) to 1.3304 (magenta solid line). The blue solid line represents the situation where refractive index of the grating layer is not modulated and that of the superstrate is modulated from 1.33 to 1.3304.

Fig. 3.8 shows the Smith chart for TE polarization. The major difference between the TM case and the TE case is that the impedance with pure grating is close to $Z = 0$ for TE rather than $Z = i$ for TM. But this is only because the phase shift for TE is different from that for TM. In Fig. 3.8, the green path represents the reflectivity with the sample refractive index of 1.33. The magenta path stands for the reflectivity with

sample refractive index of 1.3304. The blue path stands for the case where sample refractive index between the grating is 1.33 and that outside the grating is 1.3304. For TE polarization, the FWHM is 2.313×10^{-4} and bulk sensitivity is $0.6941\ RIU^{-1}$. The FOM with changing impedance between the grating is 3000, whereas for a constant grating, it is 500, which is still 17-fold improvement over the performance of the conventional SPR transducers.

The blue paths in Figs. 3.7 and 3.8 indicate that even with a uniform layer, it can be a decent sensor with considerable sensitivity enhancement. The considerable sensitivity is consistent with the field diagrams shown in Fig. 3.9 in which there is substantial leakage of field in the sample region. This also indicates that the phase of the reflection coefficient at the interface of grating and sample is sensitive to change in the refractive index of the sample region even above the critical angle and changing the resonant *k*-vector. This further indicates possible applications such as binding applications, multichannel refractive index sensing and ultrasound sensing [6, 43, 103, 126].

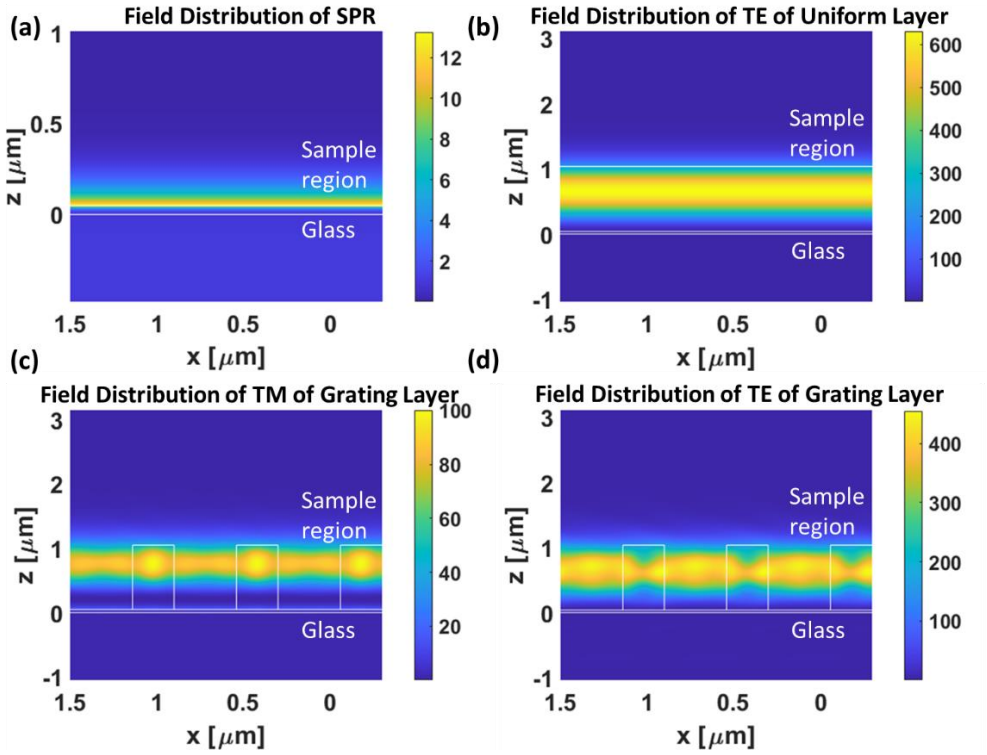

Fig. 3.9. In-resonance field distribution of (a) SPR, (b) TE with a uniform grating layer, (c) TM mode with a grating layer and (d) TE mode with a grating layer.

3.3 Sample Preparation and System Configuration

3.3.1 Sample Preparation

Two techniques were utilized for the fabrication of the proposed HARG-FP samples, i.e., sputtering and electron beam lithography (EBL). The substrate of the structure is N-BK7 coverslip (Thermo-Fischer, USA) with a refractive index of 1.515 at 633 nm (operating wavelength of the He-Ne laser). The coverslips were cleaned with an

ultrasonic cleaner while immersed in acetone and isopropanol (IPA) for 5 minutes, respectively. Then, they were rinsed with de-ionized (DI) water for 2 minutes. The cleaned coverslips were then sputtered with chromium and gold by a sputter (Nano 36, Lesker JLC). The RF gun was used to deposit a 2-nm-thick chromium layer. The DC gun was used to deposit the gold layer. With a power of 100 W, the linear growth rate of the gold layer was 0.44 nm per second. The sputter rate and the thickness of the resulted gold layer were calibrated and verified with a surface profiler to ensure optimized performance of the fabricated structures. The theoretical analysis also indicates that a thickness variation of 0.44 nm, which corresponds to 1 second error in sputtering time, would make no more than 1.5% variation in the FOM performance of the fabricated structure.

Then, the grating structure was fabricated on top of the gold layer by EBL. Prior to EBL process, a 15-nm thick layer of Adhesion Promoter 300-80 (Allresist GmbH, Germany) was deposited by spin-coating. The layer is critical for fabrication of high-aspect-ratio features since it promotes affinity between the substrate and e-beam resists and especially for surfaces with low adhesive properties, e.g., metal, and prevent the features being rinsed off during the EBL process [127]. AR-P 672.08 (Allresist GmbH, Germany) was selected as the resist for the EBL process. It is a positive PMMA e-beam resist with a molecular mass of 950 kg/mol with properties of high aspect ratio, high resolution and contrast with good adhesion to glass, silicon and

metals [128]. The resist was spin-coated on top of the AP 300-80 at a speed of 3000 rpm, which gives a desired thickness of 1 μm. The samples were pre-baked for 3 minutes at 150 °C before the lithography. The fabricated grating has a period of 600 nm and duty cycles of 23 and 42% for TM polarizations (with 48 nm gold layer), and 35% for TE polarization (with 38 nm gold layer). The exposure was conducted with EBPG 5150 (Raith GmbH, Germany). During the exposure, the voltage is 100 kV, the current is 5 nA and the dose is 850 mC/cm^2 determined with a dose test between 500 mC/cm^2 and 1500 mC/cm^2 for optimized grating profile. The grating profiles of the fabricated gratings were verified with FIB and SEM. After the exposure, the samples were then developed in AR 600-56 comprised of 1 MIBK and 3 IPA for 2 minutes and 15 seconds after which the samples were submerged into IPA for removal of developer residue. At last, the fabricated structures were baked for 1 minute at 130 °C to enhance the bond. Fig. 3.10 shows a typical cross section SEM image cut with FIB, from which the period and height of the grating can be confirmed to be 600 nm and 1 μm.

The actual writing area for EBL is around 1 mm x 1 mm, which is about the maximum non-stitching writing area for the EBL machine used. The substrates of the sensor are 22 mm x 22 mm coverslips made of N-BK7 glass.

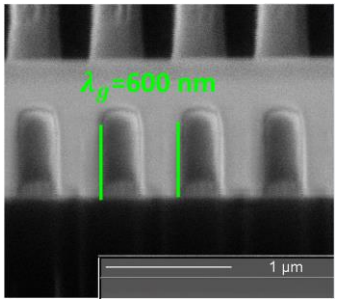

Fig. 3.10. A typical cross-section view of the fabricated grating viewed with a tilt of 45 degrees along the vertical direction; period of the grating is 600nm. The sample was produced with FIB and platinum was coated beforehand to increase conductivity contrast. Note that the 45-degree tilt results in a foreshortening by a factor of approximately $\sqrt{2}$ so the true height of the grating is ~1 µm.

3.3.2 System Configuration

The system configuration essentially adopts a prism-based attenuated total reflection (ATR) approach with angular fine-scanning capability enabled by a computer-controlled motorized stage as shown in Fig. 3.11. Since the significance of the designed HARG-FP is partially from the ultra-narrow resonance, conventional objective-lens-based focused system cannot identify the modes without complicated beam expansion, meticulous alignment and a fine camera. Moreover, the excitation angles of the HARG-FP modes are above the critical angle, which makes ATR with a prism (BK-7, OPRE32-22, Zolix, China) the most convenient approach. The source

used in the interrogation system was a linearly polarized He-Ne laser (33091, REO, US) with high output power, long coherence length, good beam quality and alignment. The beam goes through a linear polarizer and half waveplate for control of the interrogation polarization. Then, the beam is expanded by a factor of 20 with lenses L1 (f=10 mm) and L2 (f=200 mm). At the back focal length of L2 is a mirror mounted on a motorized stage (HDR50/M, Thorlabs, US). Lenses L3 and L4 are mode excitation lens pair. Lenses L5 and L6 are beam collection lens pair. The lens L3 is placed so that the mirror is at the front focal length and the sample on top of prism is at the back focal length of the lens L4 and front focal length of the lens L5. A CMOS camera (DCC3240/M) is placed at the back focal length of the lens L6. In this configuration, the camera sensor, the sample and the scanning mirror are conjugate to each other so that during scanning, the movement of the illuminated area on the sensor is minimized. L3-L6 are achromatic lenses with 50 mm focal length. In the system, minimum resolvable angle is determined by tuning step of the rotation mirror, and the excitation angle range is determined by the NA of L3 and L4, and collected angle range is determined by the NA of L5 and L6.

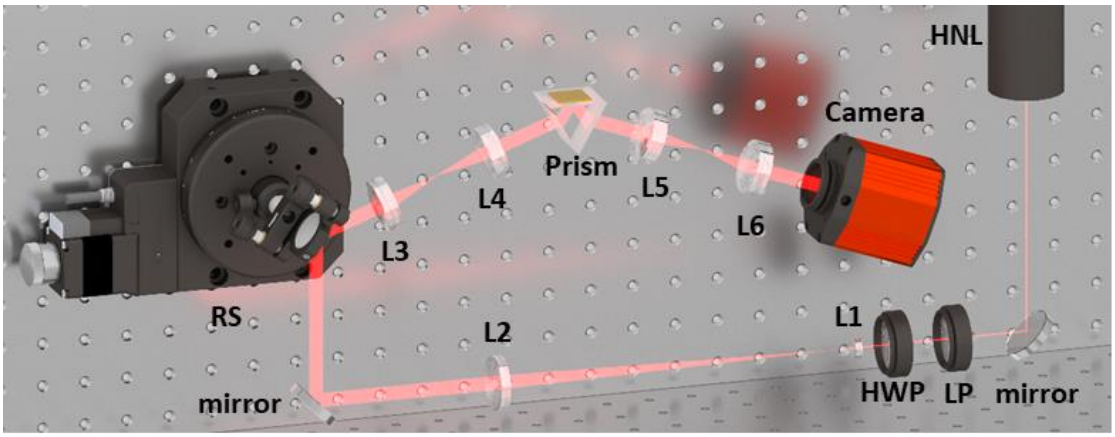

Fig. 3.11. Schematics of the system. HNL: Linearly Polarized He-Ne Laser at 633 nm wavelength; LP: Linear Polarizer, HWP: Half Waveplate at 633 nm; L1-L6: achromatic lenses; RS: motorized Rotation stage synced with camera by a computer.

The subjects of the experiment are mixtures of ethanol and DI water mixed with different mass ratios. Refractive indices of these solutions were calibrated with an ellipsometer (UVISEL Plus, Horiba, France). In the experiment, the angular scanning step of the rotating mirror was set to 0.01° for SPR and TM-polarization HARG-FP samples, and 0.005° for TE-polarization HARG-FP samples. The image acquisition sequence was developed with Python which enables the synchronized control of the stage and the camera. To completely plot the resonance over angle, the total acquisition time was less than 1 minute for a typical 400-step scan. A typical acquired image is shown in Fig. 3.12 with an angular increment of 0.02°. In the presentation of experimental data, reflectivity is plotted with respect to $n_0 \sin\theta$, minimizing the

effect of the refractive index of the substrate.

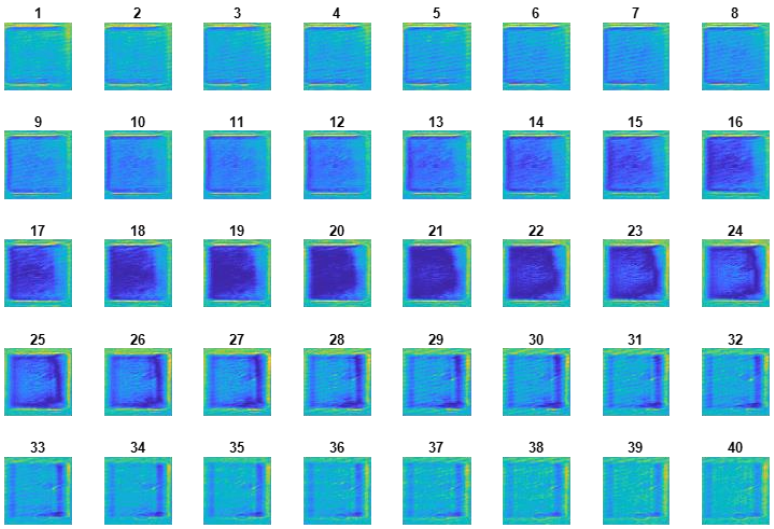

Fig. 3.12. A typical acquired image sequence covering a mode of TM polarization with 0.02° angular increments between each frame.

3.4 Experimental Result of HARG-FP

3.4.1 SPR Results

To begin with, the SPR samples with a 2-nm Cr layer and a 48-nm gold layer were measured first within the same system as a reference to benchmark the performance of HARG-FP. The samples were manufactured with the sputtering system (Nano 36, Lesker JLC, US). The chromium layer served as an adhesion layer between the gold layer and the glass substrate. The thickness of the chromium layer was estimated based on the sputtering speed calculated from bulk layer deposition. Complete

resonance dips (reflectivity curve) were recorded with the camera for each solution. Then, the curves were processed with a 3-order Savitzky-Golay (SG) filter with a 31-point window for smoothing and filtering out the parasitic interference in the optical path. The filter effect was demonstrated in Fig. 3.13(a) and all processed reflectivity curves are plotted in Fig. 3.13(b). Their dip positions are plotted with respect to solution refractive index in Fig. 3.13(c). Linear regression was performed and shown in Fig. 3.13(c). The slope of the linear regression is effectively bulk responsivity. The FWHM measured from Fig. 3.13(a) is 0.03458, and the bulk responsivity is $1.100\ RIU^{-1}$. The FOM is $31.8\ RIU^{-1}$.

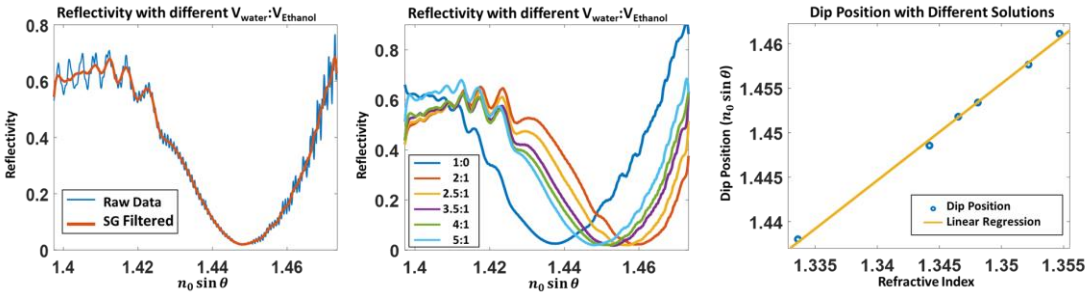

Fig. 3.13. Results from conventional SPR sample: (a) Reflectivity of a SPR sample and its SG filtered data, (b) reflectivity of the SPR sample with different aqueous solutions, (c) dip positions extracted from reflectivity and their linear regression.

3.4.2 TM and TE Mode Results

The acquisition workflow is similar to that of the SPR samples. One major difference is the wave vector corresponding to the modes. For SPR, the wave vector is around 1.45. But for TM and TE polarization with HARG-FP, the modes can be excited from 1.34, only slightly higher than the critical angle, which gives a larger range of excitation *k*-vector and a larger dynamic range. Therefore, the system was slightly modified to accommodate the difference in excitation wave vector.

For TM-polarization experiment, 2-nm chromium and 48-nm gold were sputtered the mixture ratios used were 1.5:1, 2:1, 2.5:1, 3:1 and 3.5:1 by volume. Two sets of TM samples with different duty cycles were prepared and investigated to demonstrate the effect of the perturbation inside the grating layer therefore affecting the bulk responsivity.

The first set of the TM samples has a fill factor of 42%. Fig. 3.14(a) shows the top-view grating profile, the width of the grating is 250 nm, and the period of the grating is 600 nm. As measured from Fig. 3.14(b), FWHM was 3.339×10^{-3}. The reflectivity of each mixture is shown in Fig. 3.14(c) and the wave vector of their minimum is plotted against the refractive index of the solution in Fig. 3.1(d). The linear regression of dip position indicates that the bulk responsivity of 42% was $0.4896\ \mathrm{RIU}^{-1}$. Therefore, the FOM of the 42% TM sample was $147\ \mathrm{RIU}^{-1}$, which is 4.7 times higher than that of the conventional SPR sample.

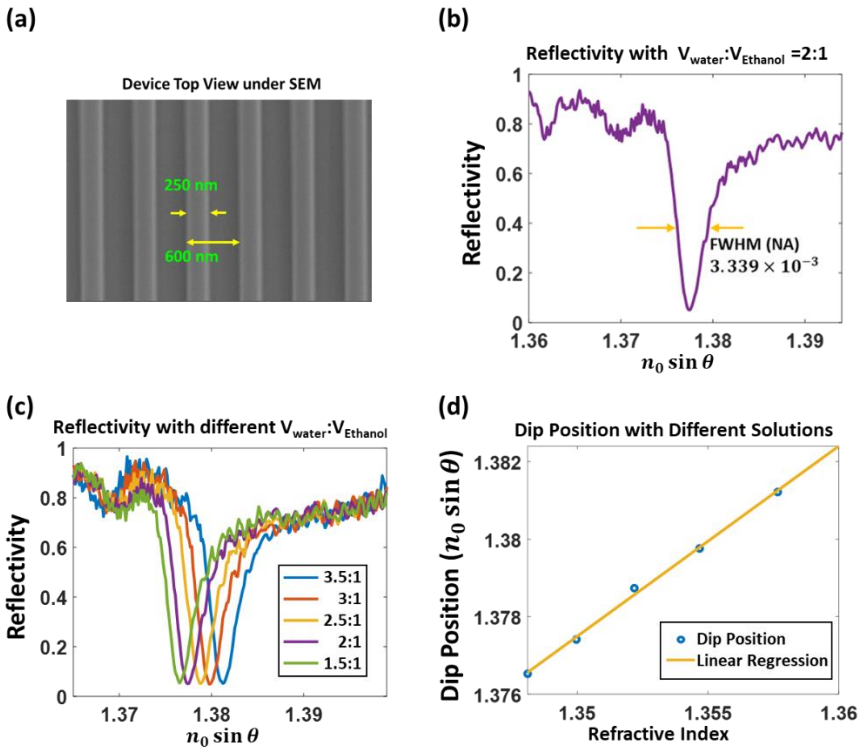

Fig. 3.14. Results from the TM sample with 42% duty cycle: (a) top-view SEM image, (b) reflectivity with V_{water}:$V_{ethanol}$ 2:1, (c) reflectivity with different aqueous solutions and (d) dip position and their linear regression.

The second set of the TM sample has a fill factor of 23%. Measured from the top view SEM image in Fig. 3.15(a), the grating is 182 nm wide with a period of 800 nm. Measured from reflectivity in Fig. 3.15(b), FWHM was 2.959×10^{-3}, 11.5% narrower than that of 42% fill factor sample. The reflectivity of all tested mixtures is displayed in Fig. 3.15(c) and their resonance minimum is plotted in Fig. 3.15(d) against the refractive index of the tested mixtures. The linear regression in Fig. 3.15(d) indicates a bulk responsivity of 0.9809 RIU^{-1}. Thus, the FOM was 331 RIU^{-1}, 10-

fold enhancement over the reference SPR sample. The experimental result of the pair of samples confirms that the decrease in fill factor of the grating results in narrower FWHM and higher bulk responsivity, thus, in increase in the FOM.

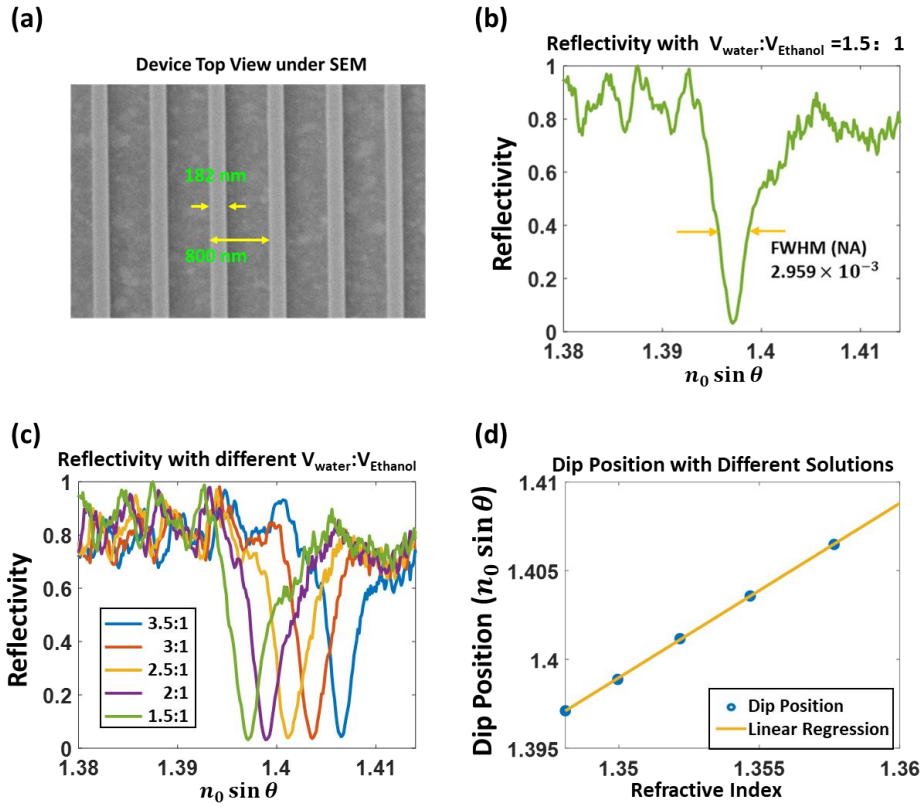

Fig. 3.15. Results from the TM sample with 23% duty cycle: (a) top-view SEM image, (b) reflectivity with Vwater:Vethanol 1.5:1, (c) reflectivity with different aqueous solutions and (d) dip position and their linear regression.

For TE-polarization samples, 2 nm chromium and 38 nm gold were sputtered, and the grating was fabricated by EBL technique. The mixture ratio of water and ethanol

was from 1:1 to 5:1 by volume.

Fig. 3.16(a) shows the grating profile with width of 205 nm and period of 600 nm. Therefore, the fill factor is 34%. Fig. 3.16(b) shows the reflectivity of a solution with a volume mix ratio of 3:1. the FWHM was 6.166×10^{-4} in $n_0 \sin\theta$. The value corresponds to a 56-fold improvement over the conventional SPR and a 5-fold improvement over TM samples. The reflectivity of all tested mixtures is summarized in Fig. 3.16(c), with their dip minimums plotted against the refractive index of the tested solutions in Fig. 3.16(d). The bulk responsivity was $0.8598\ \mathrm{RIU}^{-1}$. Therefore, the FOM was $1394\ \mathrm{RIU}^{-1}$, which corresponds to an improvement of 44 times compared with that of the conventional SPR acquired measured using the identical system and an improvement of 4 times compared with the TM grating samples.

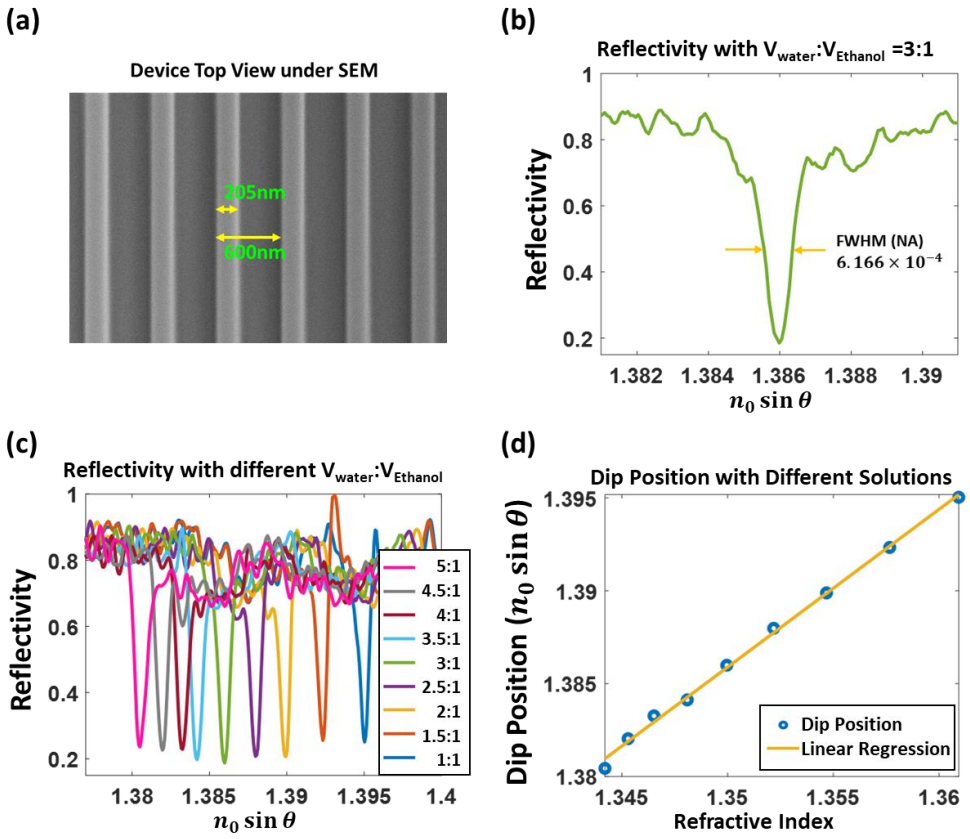

Fig. 3.16. Results from the TE sample: (a) top-view SEM image, (b) reflectivity with V_{water}:$V_{ethanol}$ 3:1, (c) reflectivity with different aqueous solutions and (d) dip position and their linear regression.

The results of TM and TE grating samples together with the conventional SPR sample are summarized in Table 3.2.

Table 3.2 Comparison of Results Between TM, TE And Conventional SPR

	Bulk Responsivity (RIU^{-1})	FWHM	FOM (RIU^{-1})
TM w/ 42% duty cycle	0.4986	3.339×10^{-3}	147
TM w/ 23% duty cycle	0.9809	2.959×10^{-3}	331
TE w/ 35% duty cycle	0.8598	6.166×10^{-4}	1394
Conventional SPR	1.100	3.458×10^{-2}	31.8

3.4.3 Sensitivity Analysis

Sensitivity of a refractive index sensor, S, is defined as minimum detectable change of refractive index, which is equivalent to noise equivalent change in RIU. This is jointly determined by noise level in the system (NEP) and the slope of the reflectivity curve, the latter of which is related to the FWHM and dip prominence. The sensitivity is given by:

$$S = \Delta n = NEP \Big/ \left(\frac{dI}{dn_0 \sin\theta} \cdot \frac{dn_0 \sin\theta}{dn_s} \right) \tag{3.11}$$

where S denotes the sensitivity of the system, Δn denotes the minimum detectable change in RIU, NEP denotes the system noise level, $\frac{dI}{dn_0 \sin\theta}$ denotes the maximum slope of the reflectance, and $\frac{dn_0 \sin\theta}{dn_s}$ denotes the bulk sensitivity of the structure.

There are two major noise sources identified in the system, i.e., power fluctuations from the laser and camera noise, including dark noise and shot noise. Therefore, camera noise level, laser noise level and total noise level are investigated separately.

During the evaluation, the camera was set to low read noise mode, frame rate was set to 719 frames per second and region of interest was set to 30 pixels × 30 pixels.

The dark noise was measured with about 17000 frames. The laser fluctuation was measured with 20,000 frames. The total noise level was measured with 15,000 frames. In the following calculations, $\frac{dI}{dn_0 \sin\theta}$ is set to 1030.6, the maximum slope for TE samples as measured, and $\frac{dn_0 \sin\theta}{dn_s}$ is 0.8498, the bulk responsivity for TE samples.

Noise from the camera is the hard cap for sensitivity performance of the designed system. The camera used in the system was DCC3240/M, 16-bit sCMOS camera with passive cooling. The measured standard deviation of normalized dark noise was 7.50×10^{-8}. Therefore, the noise-equivalent refractive index change is 8.57×10^{-11} RIU.

Power fluctuations in the laser constitute most of the noise in the system as it is amplified by the optics and electronics in the system as light propagates. Power fluctuations were measured by placing a mirror temporarily after the beam expansion lenses and pivoting the beam into a DCC3240/M. The measured standard deviation of fluctuations was 1.15×10^{-5}. Therefore, the noise-equivalent refractive index change is 1.31×10^{-8} RIU.

The total noise equivalent sensitivity measured in the system is 1.87×10^{-8} RIU without frame averaging. As shown in Fig. 3.17, averaging 794 frames (approximately 1 second acquisition time) further improves the sensitivity to 1.61×10^{-9} RIU.

Although averaging improves the sensitivity by a considerable amount, the improvement is less rapid than $\sqrt{N}$, where N denotes the frames averaged, which is the improvement rate for completely random sequence. This is attributed to a degree of correlation between successive frames.

Extra measures during the experiment can be carried out to compensate for the laser fluctuations temperature drift, including a reference beam to cancel out common-path noise. The thermal optic coefficient for water can be -1.20×10^{-4} RIU/°C. Phase detection or polarization detection are also expected to contribute considerable improvement with the same structure [21, 41, 129].

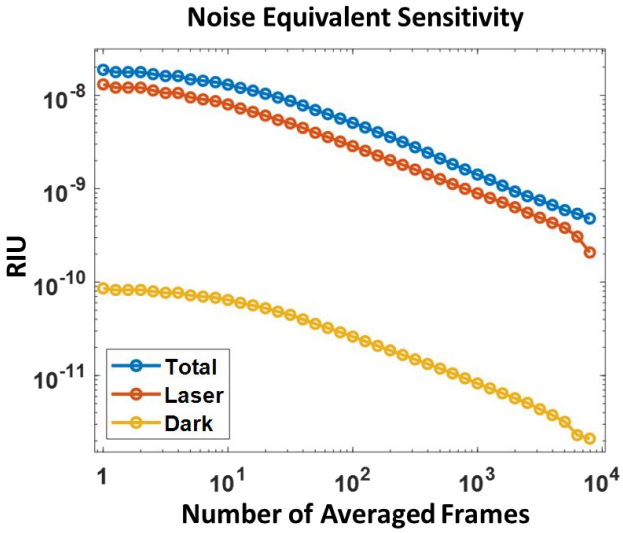

Fig. 3.17. Noise-equivalent RIU (sensitivity) measured respectively from the laser, the camera and entire system.

3.5 Summary

In this chapter, high-aspect-ratio-grating-based Fabry-Pérot (HARG-FP) resonators have been presented and investigated both theoretically and experimentally with TM and TE polarization for high-FOM refractive index measurement. The parameters of the high aspect-ratio grating are carefully chosen so that there is no propagating diffracted order. Therefore, the grating can be treated as a uniform layer with an effective refractive index n_{eff} calculated with Eqs. (3.3) to (3.5). The advantage of the HARG-FP is that the sensing region also forms part of the grating by filling the grooves between the grating bars. Therefore, change of the refractive index in the sensing region directly interacts with the field in the grating region by modulating the effective refractive index as well as the evanescent field above the grating region.

Theoretically, transmission line model and Smith charts was used to present a more intuitive understanding on layer-wise physical mechanism and show the relative contributions of different mechanisms. Experimentally, a direct comparison between conventional SPR, TM- and TE-polarization HARG-FP were drawn within the same experiment system. An FOM of 1394 was recorded with TE-polarization samples with a fill factor of 34%, which outperformed SPR by a factor a 44. A factor of 10 improvement in FOM for TM-polarization was recorded for TM samples. Noise-equivalent sensitivity of 1.874×10^{-8} RIU was observed for TE-polarization without frame averaging. Averaging 794 frames (approximately 1-second acquisition time)

can improve the sensitivity to 1.609×10^{-9} RIU. It is expected that with the use of phase detection and polarization detection techniques, the sensitivity can be further improved to 10^{-10} RIU.

Chapter 4 Theoretical Analysis of Total-Internal-Reflection-based Fabry-Pérot Resonator

4.1 Introduction

Ultrasound and photoacoustic techniques for sensing and imaging have been developing rapidly over the last few decades as a non-invasive and non-destructive approach for applications in industrial evaluation, clinical diagnosis and biomedical analysis [2, 130-133]. The emphasis of the research into these techniques is directed towards great sensitivity, broader bandwidth in order for higher precision and accuracy for sensing and higher resolution and image quality for imaging [106, 134, 135]. For generation and detection of the ultrasound, the piezoelectric effect has been the most widely adopted approach by using piezoelectric materials that have no inversion symmetry to convert between mechanical energy and electrical energy [136, 137]. There have been research breakthroughs in successfully producing piezoelectric transducers with center frequencies above 1 GHz and wide bandwidth, but there are several intrinsic constraints to this approach: (i) the bandwidth is narrow for the conventional approach without careful control of the damping process; (ii) high center frequencies require ultra-thin piezoelectric material [138, 139], which is demanding for transducer fabrication and gives low yield; (iii) optimal sensitivity and bandwidth requires fastidious control over electrical and acoustic impedance matching [140]; (iv)

bulky size and optical opacity of the said transducers further improve the difficulty for integration with other modalities [82, 141]. There has been continued research on alternative approaches to overcome the abovementioned constraints [7, 82, 142].

Optics has arisen as a convenient method for generation and detection of ultrasound with wide bandwidths, with easy integration and miniaturization potential [7, 10, 104]. Moreover, optical sensors can circumvent the requirement for electrical impedance matching encountered with conventional piezoelectric methods. Furthermore, polymer materials have an acoustic impedance closer to water, which is commonly used as the couplant of acoustic wave, therefore, acoustic impedance mismatch can be ameliorated [141].

Two mechanisms used in optical sensors for detection of acoustic waves are: (i) acousto-optic effect, i.e., detection of acoustic pressure induced refractive index change, e.g., surface plasmon resonators (SPR), and (ii) detection of cavity length change in a resonator that results from acoustic pressure, e.g., Fabry-Pérot (FP) resonator [84, 143-145]. Because of acousto-optic effect, certain conventional refractive index sensors, e.g., SPR, ring resonators and various critical-angle-based resonators, can be adapted as pressure sensors and be used to detect ultrasound [31, 103, 146-148]. Since the sensing depends on the evanescent field, which is usually less than 1 μm extent, theoretical bandwidths can reach the gigahertz regime [31, 82]. Indeed, experimentally, over 170 MHz has been realized with the refractive-index-

sensing-based acoustic sensors, where the limit is the electronics rather than mechanism [103, 149]. Nevertheless, sensitivity performance of these devices is limited by the acousto-optic coefficient, which is 1.35×10^{-10} RIU $\cdot$ Pa^{-1} for water. As the resulted refractive index change is small, so high sensitivity detection demands more a complex experiment system [148].

The FP resonator structure is well-established in ultrasound and photoacoustic applications, e.g., sensing and imaging [150-153]. The conventional structure comprises two reflecting mirrors and an optical cavity in between [84]. The round-trip resonance condition of an FP mode is given by [37, 154]

$$2k_z d + \phi_1 + \phi_2 = 2m\pi, m = 0 \text{ (for TE)}, 1, 2, 3, \ldots \quad (4.1)$$

where $k_z = \frac{2\pi}{\lambda} n_s \cos\theta$ denotes the z-component of the wave vector inside the spacer, d denotes the spacer thickness, i.e., the cavity length, n_s denotes the refractive index of the spacer, ϕ_1 and ϕ_2 denote the phase changes at the upper and lower interfaces of the cavity, respectively, m is a non-negative integer denoting the FP orders, where m can be 0 with TE polarization (but not TM), λ is the incident wavelength, and θ is the propagation angle inside the spacer.

The acoustic wave perturbs the thickness of the FP cavity, i.e., d, resulting in a change of the resonance condition and this change is reflected in a change in reflected/transmitted amplitude, phase or polarization. The change in thickness caused by acoustic stress inside the cavity also implies a change in local refractive index,

which is the acousto-optic effect, and thus affects k_z. However, this effect is generally ignored in the study of FP [93, 155].

Extensive research has been conducted on planar FP transducers. Typically, metal has been used as the material for the reflecting mirror, e.g., gold, silver or copper [156-161]. However, this can make the transducer opaque and less compatible with other modalities. To address this, transparent structures, e.g., Bragg reflectors and meta-surfaces have been used, which increases the compatibility [7, 84]. Transducers with polymer substrate and soft dielectric mirrors have been investigated, which further decreases acoustic impedance mismatch, thus yielding a broader and flatter frequency response [84, 162, 163].

Besides planar FP transducers, plano-concave FP transducers have been proposed for high sensitivity photoacoustic imaging applications, with sensitivity down to 2.6 Pa over 2.8 MHz bandwidth [7]. The transducer comprises cured free-standing spherical caps sandwiched between two eight-layered alternate stack of λ/4 thickness of ZnS and Na_3AlF_6, both of which are dielectric [84]. Compared with metal, dielectric materials have no loss, therefore can give an optical resonance with higher Q and better optical transparency, but the resulted layers are thicker. Therefore, the acoustic mismatch between water and reflecting mirrors is more pronounced. Moreover, the deposition process is more complicated, and the deposited layer stacks are prone to cracking and low yield.

When assessing the performance of different optical detection mechanisms for ultrasound, there are three crucial factors: bandwidth, responsivity and sensitivity. Responsivity is a measure of the change in the measured parameter with respect to incident pressure. In this chapter, reflectivity is the parameter used as a proxy for the measurand (pressure). Sensitivity is related to noise equivalent pressure (NEP), which is related to both the noise level of the experimental system and the responsivity of the transducer.

In this chapter, a total-internal-reflection-based Fabry-Pérot resonator (TIR-FP) is proposed and assessed theoretically. The operating optical wavelength is 1550 nm, which is convenient for both spectroscopy and angular interrogation. In the analysis, optimal thickness for each layer is determined by optimizing responsivity with simulations. It is also shown that the use of an open resonator structure confers advantages for both the refractive index sensing mechanism (wide bandwidth) and the FP mechanism (improved sensitivity). Fig. 4.1 shows the schematics of the proposed total-internal-reflection based FP (TIR-FP) structure and the conventional Kretschmann configuration for coupling and interrogation. The proposed structure comprises two layers, a metal layer and a homogeneous dielectric spacer acting as the FP cavity. Fig. 4.1(b) shows an illustration of different mechanisms of the TIR-FP, where variation of both thickness change and refractive index change within the evanescent field above the spacer-water interface. The incident light is above the

critical angle, so total internal reflection occurs when light reflects off the water interface. With a thin layer of gold as a partial reflector, an FP cavity is formed. This setup avoids another reflecting layer and allows the use of very soft polymers, e.g., polydimethylsiloxane (PDMS), which would be difficult in conventional FP due to strength mismatch. The greater compliance of these materials means that for a given thickness, the resulting resonator is much more sensitive, and the corollary is that for a given sensitivity, the smaller resonator thickness confers a greater bandwidth [164].

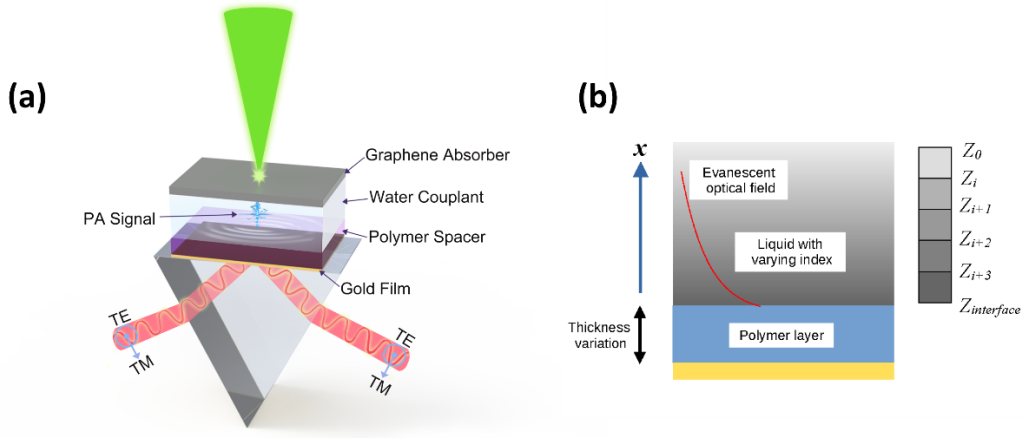

Fig. 4.1. (a) Layout of the proposed total-internal-reflection-based Fabry-Pérot structure and the prism-based Kretschmann configuration. Also shown is the photoacoustic generation system used for system evaluation. PA: photoacoustic; TM: transverse magnetic; TE: transverse electric. (b) An illustration of the transduction mechanisms of the TIR-FP.

4.2 Overview Analysis of TIR-FP Resonance

The proposed TIR-FP structure operates as an FP cavity. Two reflectors in the structure are a gold layer as the first partial reflector and the interface between the spacer and water as a perfect reflector. The operating principle is that a portion of light incident from the prism passes through the gold layer and propagates in the spacer layer; the propagation angle is such that light is totally internally reflected at the spacer/water interface. Therefore, no wave is propagating in water and an evanescent wave is formed above the interface. For light to propagate in the polymer and be totally internally reflected off water, the refractive indices must satisfy the following relationship:

$$n_w < n_s, n_w < n_{gl} \tag{4.2}$$

where n_w is the refractive index of water, n_s is that of spacer and n_{gl} is that of the prism.

A sound wave interacts with the structure essentially with two mechanisms: (i) modulating the local refractive index in the region of the evanescent field above the interface of the spacer and water; (ii) squeezing and contracting the cavity in *z*-direction, *d* in Eq. (4.1).

First, the cavity is considered without perturbation of sound. Under the round-trip resonance conditions described in Eq. (4.1), ϕ_1 and ϕ_2, which represents the change of phase at the top and bottom boundary of the spacer, can be calculated as the phase

angles of the reflectivity at the interfaces of spacer-water and spacer-gold, respectively.

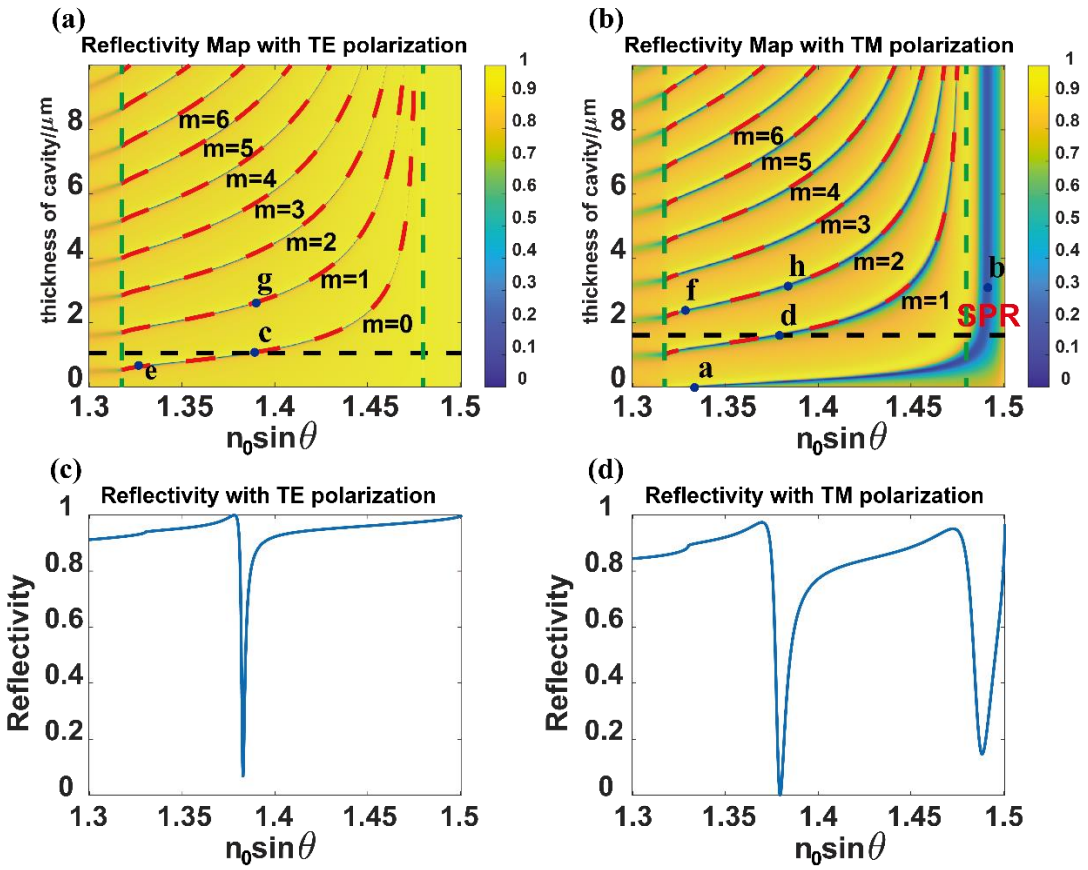

Fig. 4.2. Reflectivity maps for PMMA-based structure varying $n_0 \sin\theta$ and cavity thickness values for (a) TE and (b) TM polarizations. (c) Reflectivity with the 1-μm-thick cavity and the TE polarization. (d) Corresponding reflectivity with the 1.6-μm-thick cavity and the TM polarization.

Figs. 4.2(a) and 4.2(b) show reflectivity maps for TIR-FP varying cavity thickness and incident angle for TE and TM, respectively. Reflectivity is plotted with respect to

wave vector, $n_0 \sin\theta$, rather than θ, as this is independent of material of the prism (n_0). The gold layer thicknesses are 12 nm and 30 nm for TE and TM polarizations, respectively. In calculation, the refractive indices used were 1.501, 0.84991 + 10.925i, 1.4771, and 1.3180 for substrate glass, gold, spacer and water, respectively [165-167]. Therefore, the wave vector for the critical angle of the water is 1.3180, and that for PMMA is 1.4771, which are shown in green dashed vertical lines in Figs. 4.2(a) and 4.2(b). In between is where the FP modes exist. Since all layers in the setup are homogenous, calculation is performed with the Fresnel equations. Superposed dashed red curves are calculated with Eq. (4.1) with m as non-negative integers. For TE polarizations, since the sum of ϕ_1 and ϕ_2 is negative, there is the zeroth mode between the critical angles. Figs. 4.2(c) and 4.2(d) show reflectivity for TE and TM polarization with 1 μm and 1.6 μm, respectively. The thicknesses were chosen so that the wave vectors of the resonance are similar, because the linewidth and responsivity of the resonance depends on the angle of the mode. In Figs. 4.2(b) and 4.2(d) of TM polarization, it can be noted that the SPR mode is present since the thickness of gold is similar to optimal thickness of SPR design at the same wavelength. It can be confirmed that the operating modes are FP modes since the dips calculated with Fresnel calculations overlaps with that calculated with Eq. (4.1).

The difference between SPR and FP with different orders can be easily demonstrated with on-resonance field distribution as shown in Fig. 4.3.

In Fig. 4.3, eight subplots of on-resonance field distribution are displayed with their corresponding resonances marked in Figs. 4.2(a) and 4.2(b). For TM polarization, H_y component was drawn, whereas for TE polarization, E_y was drawn.

It can be concluded that an evanescent field is formed on top of the spacer layer. For resonance close to the critical angle, e.g., the cases shown in Figs. 4.3(f) and 4.3(g), the penetration depth of the evanescent field is larger, which would result in a wider bandwidth. SPR can be excited even with a thick spacer, but as its field decays quickly and barely interacts with the acoustic pressure in the fluid, little sensitivity can be expected.

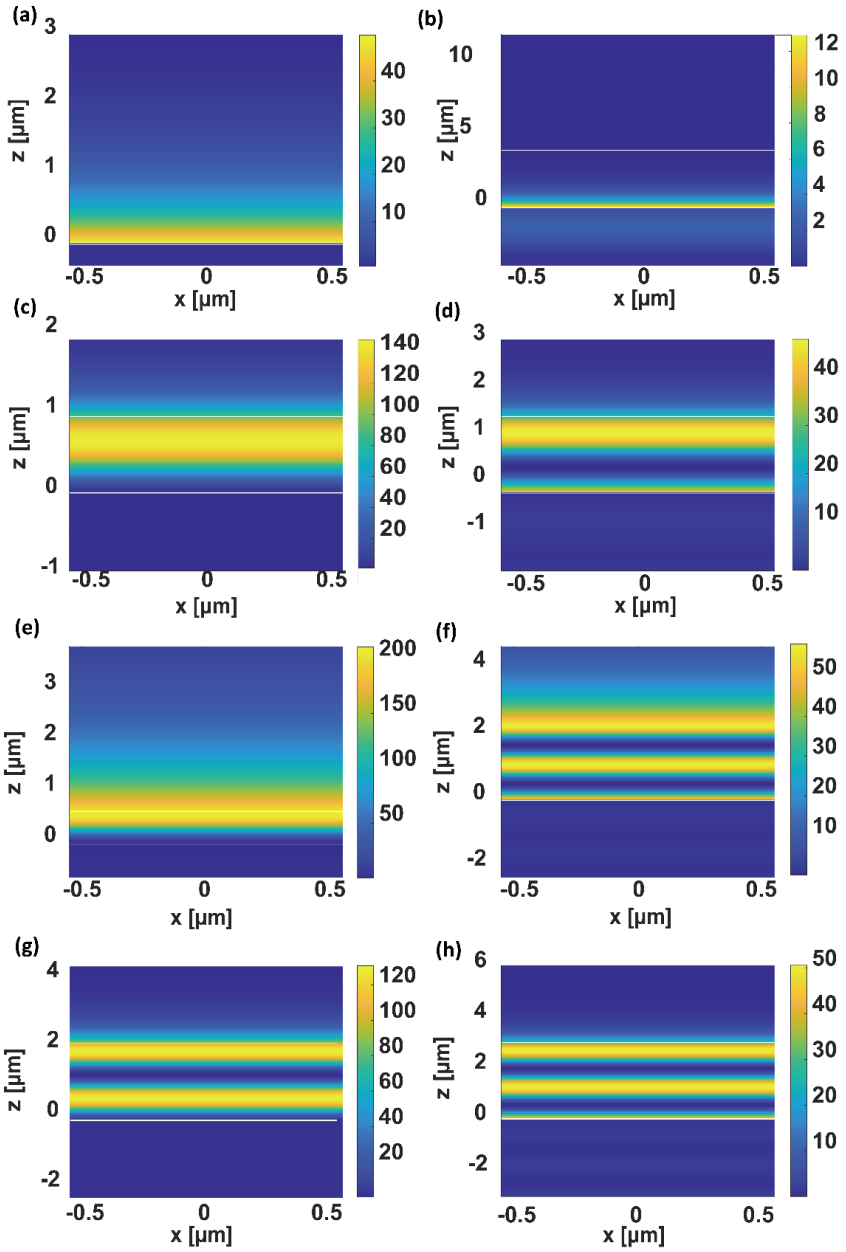

Fig. 4.3. On-resonance field distributions: (a) SPR with no spacer layer, (b) SPR with 4 µm spacer layer, (c) TE_{00} mode with 1 µm thick spacer, (d) TM_{01} mode with 1.6 µm thick spacer, (e) TE_{00} mode with 0.62 µm thick spacer, (f) TM_{02} mode with 2.3 µm thick spacer, (g) TE_{01} mode with 2.2 µm thick spacer, (h) TM_{02} mode with 3 µm thick spacer.

4.3 Acousto-Optic Effect based Sensing Mechanism

Two dominant detection mechanisms are considered for TIR-FP next, i.e., acousto-optic-effect-based sensing mechanism and cavity length sensing mechanism. In practice, it is a plausible simplification to regard these two mechanisms as separate and not related when analysing ultrasound responses at practical levels since acousto-optic effect happens at the interface modulating the refractive and the cavity length sensing mechanism happens within the cavity modulating thickness. They affect the different aspects of the resonance and, therefore, can be considered independent and the effects can be cumulative.

First, assuming no thickness change occurs in the FP cavity, the acousto-optic-effect-based sensing mechanism is considered. This mechanism is analogous to the detection mechanism of SPR sensors, where a change in local refractive index of the liquid changes the resonance conditions at the gold-water interface and eventually converts to a fluctuation in reflectivity. Here, the factor that determines the resonance is the phase, ϕ_1 in Eq. (4.1).

TE polarization is considered first. The reflection coefficient at the spacer-water interface is given by:

$$r_s = \frac{n_s \cos\theta_s - n_w \cos\theta_w}{n_s \cos\theta_s + n_w \cos\theta_w} \tag{4.3}$$

where subscript s and w denote spacer and water, respectively.

Incident angle θ_s and refracted angle θ_w follow the Snell's Law:

$$n_s \sin\theta_s = n_w \sin\theta_w \tag{4.4}$$

Since the incident angle is above the critical angle for spacer-water interface, therefore,

$$\cos\theta_w = i\sqrt{\left(\frac{n_s \sin\theta_s}{n_w}\right)^2 - 1} \tag{4.5}$$

This indicates that in Eq. (4.3), $n_s \cos\theta_s$ is real and $n_w \cos\theta_w$ is imaginary. Phase of the numerator ϕ_{top} can be worked out by an inverse tangent of the imaginary part over real part:

$$\phi_{top} = \text{atan}\frac{-\sqrt{(n_s \sin\theta_s)^2 - {n_w}^2}}{n_s \cos\theta_s} \tag{4.6}$$

And the numerator and denominator are complex conjugate to each other. Thus, ϕ_1, phase of r_s, can be worked out as twice the phase, ϕ_{top}, of the numerator.

$$\phi_1 = phase(r_s) = 2\phi_{top} \tag{4.7}$$

Phase change with respect to n_w, refractive index of water, can be given by:

$$\Delta\phi_1 = 2\frac{d\phi}{dn_w}\Delta n_w = \frac{2n_w n_s \cos\theta_l \Delta n_w}{\sqrt{n_l^2 \sin^2\theta_s - n_w^2(n_s^2 - n_w^2)}} \tag{4.8}$$

The analytical result calculated with Eq. (4.8) is shown in Fig. 4.4 with PDMS as spacer material and the incident angle corresponds to θ_l. The figure shows that the sensitivity decreases as the angle of incidence increases above the critical angle of spacer/water interface, i.e., 72.7°.

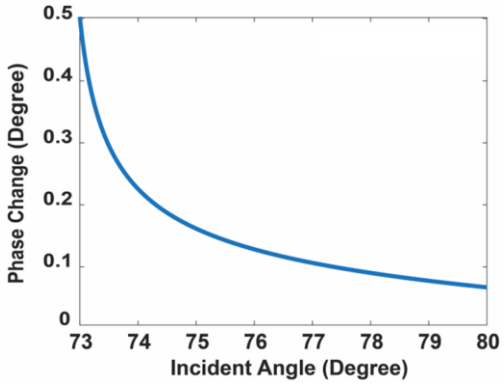

Fig. 4.4. Phase change calculated using the analytical expression in Eq. (4.8) with a refractive index of 10^{-4} and the optical parameters associated with PDMS. Note that the incident angles on the *x*-axis refer to the incident angle from the spacer not the glass prism.

For TM polarization, following the same procedure, the phase change with respect to n_w, refractive index of water, can be given by:

$$\phi_1 = phase(r_s) = \pi - 2\phi_{top} \tag{4.9}$$

$$\Delta\phi_1 = \frac{-2n_s \cos\theta_w n_w \Delta n_w}{{n_w}^2 (n_w \cos\theta_s + n_s \cos\theta_w)} \tag{4.10}$$

where $\cos\theta_w = \sqrt{(n_l \sin\theta_l / n_w)^2 - 1}$.

By working out the derivative of Eq. (4.10), it can be confirmed that above the critical angle, $\Delta\phi_1$ is monotonically decreasing with increasing angles.

Consider an acoustic pressure of 1 MPa with normal incidence at the top surface, which leads to a refractive index shift in water (n_w) from 1.318 to 1.318135 with an acousto-optic coefficient of $\Delta n_w/\Delta p = 1.35 \times 10^{-10}$ Pa^{-1}. Figs. 4.5(a) and 4.5(b) shows the response maps varying spacer thickness and wave vector for TE and TM

polarizations, respectively. Figs. 4.5(c) and 4.5(d) show the responses of 1 μm and 1.6 μm spacer for TE and TM polarization, respectively. It can be concluded that sensing with TIR-FP and TE polarization can give more responsivity.

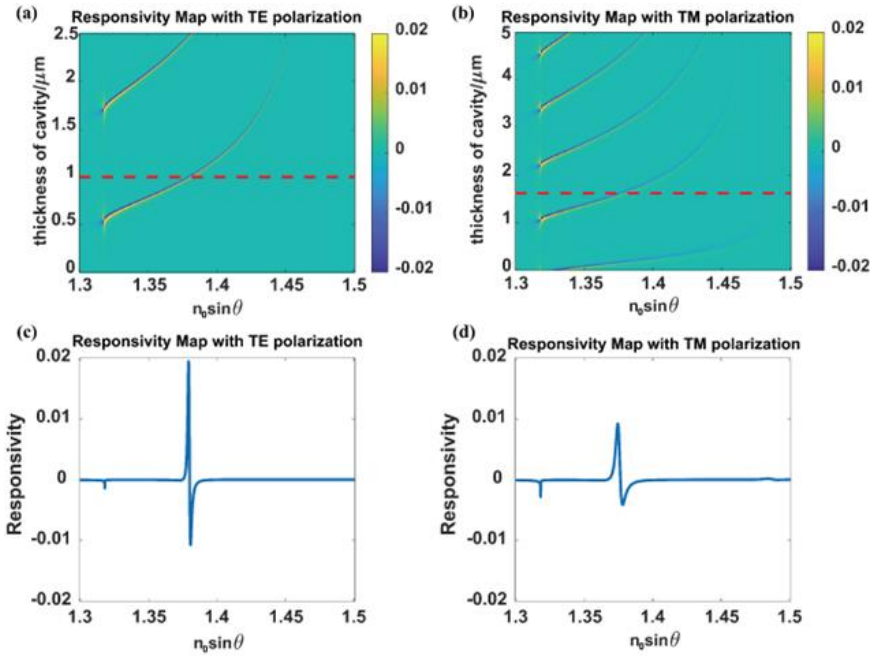

Fig. 4.5. Responsivity maps showing variation with $n_0 \sin\theta$ and cavity thickness for (a) TE and (b) TM polarizations. (c) Responsivity with a 1-μm-thick cavity and TE polarization. (d) Responsivity with a 1.6-μm-thick cavity and TM polarization.

As shown in Figs. 4.5(c) and 4.5(d), the FWHM for TE polarization is narrower than that for TM polarization. This is due to the absorption in the gold layer. With the same thickness of gold, loss for TM is always greater than that for TE polarization.

Since for TM polarization, gold thickness is 30 nm, whereas that for TE is 12 nm, this is even more pronounced.

The bandwidth of this mechanism can be estimated considering the situation in Fig. 4.1(b). In Fig. 4.1(b), the red curve represents the evanescent field that is excited by a totally internally reflected beam in the spacer layer. The extent of this field depends on the wavelength and incident angle of the incident light in the spacer. If the incidence is slightly above the critical angle, the depth of the field will be deep in the water, whereas if the incidence is well above the critical angle, the field will be more tightly confined to the surface. The grey scale represents variations of refractive index for water caused by acoustic perturbation. If the wavelength of the acoustic wave is substantially longer than the penetration depth of the evanescent field, the field sense almost constant refractive index. But if the wavelength of the acoustic wave is on the same order as the penetration depth of the evanescent field, the refractive index change sensed by the field will cancel out over the penetration depth, therefore, reflectivity change cannot reflect the profile of the acoustic wave.

In order to estimate the bandwidth of the mechanism, two quadrature phasors are introduced to describe the refractive index variation in the water caused by acousto-optic effect.

$$n(x) = n_0 + \Delta n \cos(k_{ac}\, x) \tag{4.11}$$

$$n(x) = n_0 + \Delta n \sin(k_{ac}\, x) \tag{4.12}$$

where n_0 is the base refractive index, Δn is the maximum refractive index change caused by acoustic pressure, k_{ac} is the wave vector of the acoustic wave and x is the distance from the spacer/water interface.

Variation in refractive index is then converted to an impedance change which is propagated back to the spacer/water interface. Frequency responses with different incident angles in the glass are shown in Fig. 4.6. This is simply performed by propagating the impedance piecewise through extremely thin layers as depicted schematically in Fig. 4.7. Modulus of the impedance change is then projected onto the interface, and this is the perturbation seen by the cavity.

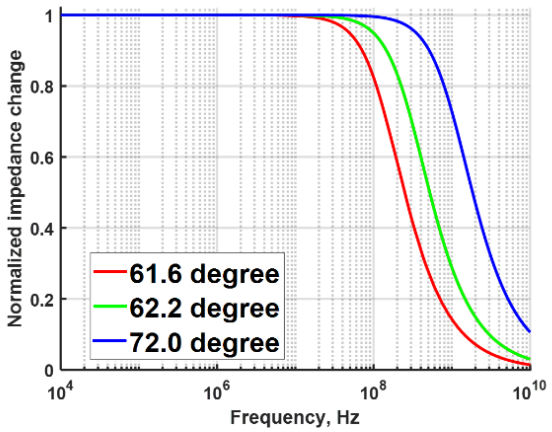

Fig. 4.6. Frequency response of normalized impedance change considering TIR-FP modes at various incident angles above the critical angle.

The curves in red, green and blue are for 61.6°, 62.2° and 72.0°, the first value is just above the critical angle. Impedance change with red curve falls to half maximum

at 250 MHz. The green curve rolls off to half maximum at approximately 500 MHz, whereas for blue curve, the half maximum is at around 2 GHz. Note that the analysis is indifferent to materials, however, for PDMS with 72° incidence, no FP modes will exist in the spacer since it is above the critical angle for the prism and PDMS, but for PMMA, this is realizable.

A classic trade-off can be observed between responsivity and bandwidth within TIR-FP. It was shown that, above the critical angle of the interface between the spacer and water, as the angle increases, the responsivity, which is solely related to the phase change $\Delta\phi_1$, decreases. However, as the incident angle increases, *z*-component of the *k*-vector is decreasing since $k_z = k\cos\theta$. Therefore, the penetration depth of the evanescent field decreases, therefore, the bandwidth is monotonically increasing with respect to the incident angle.

4.4 Cavity Length Sensing Mechanism of TIR-FP

A change in cavity length, *d*, can shift the resonant condition of the cavity. To calculate the change in cavity dimensions, strain distribution throughout the cavity is calculated. Take $P(x)$ as the pressure distribution in the cavity and strain is represented by $\varepsilon(x)$. Therefore, the total deformation Δl in the cavity is given by

$$\Delta l = \int_0^d \varepsilon(x)\,\mathrm{dx} = \int_0^d \frac{P(x)}{M}\,\mathrm{dx} \tag{4.13}$$

where the polymer occupies the space between 0 and d, and M is the modulus c_{11}, because the layer is constrained from dimensional changes in the plane of incidence.

Note here that the pressure and the strain are phasor quantities, and when the wavelength of the acoustic wave in the layer is comparable with the thickness of the layer *d*, variation will occur in the phase that will decrease the total deformation in the cavity, thus setting the bandwidth limit of the structure.

It is possible to analyse the pressure distribution numerically with available finite element method software packages, e.g., COMSOL Multiphysics. However, the configuration of the TIR-FP structure lends itself to a more straightforward and highly computation-efficient approach based on acoustic impedance.

4.4.1 Calculation of the Pressure Distribution and the Associated Strain in the Spacer Layer

The method is essentially adapted from that provided by Azzam and Bashara [20], but with an addition to allow that the pressure field distribution can be obtained at arbitrary positions with forward and backward propagating pressure waves [164].

Normally, there is no need to consider any obliquity factors since acoustic waves propagate normally through the structure and interact with all interfaces. In this case, the acoustic impedance, Z, can be given by the product of its density, ρ, and the sound velocity, v, in the material:

$$Z = \rho v \tag{4.14}$$

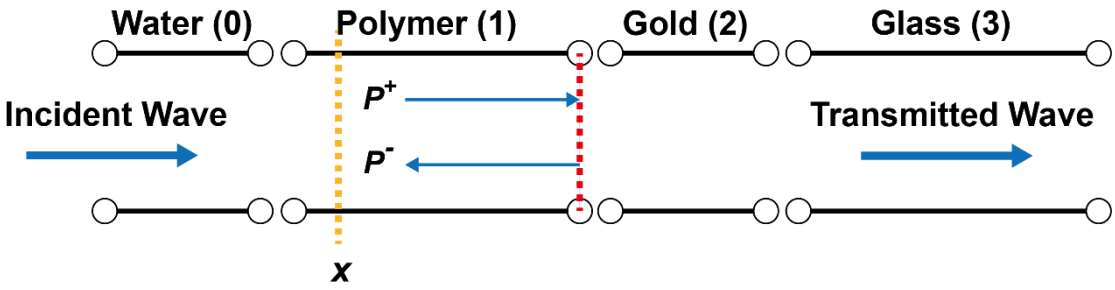

Fig. 4.7. Transfer matrix model of acoustics in the TIR-FP.

Fig. 4.7 shows the acoustic transmission line model of our transducer, where the different layers and materials are numbered as labelled. The transfer matrix of the model which give describe the relationship between the input pressure from water and the transmitted wave in the glass as follow:

$$\begin{bmatrix} P_0^+ \\ P_0^- \end{bmatrix} = [\boldsymbol{S_{tot}}] \begin{bmatrix} P_3^+ \\ P_3^- \end{bmatrix} \tag{4.15}$$

where $\boldsymbol{S_{tot}}$ represents the field propagation through the structure.

$$\boldsymbol{S}_{tot} = \boldsymbol{I}_{01}\boldsymbol{\Phi}_1\boldsymbol{I}_{12}\boldsymbol{\Phi}_2\boldsymbol{I}_{23} \tag{4.16}$$

where $\boldsymbol{\Phi}$ refers to the propagation matrix.

In Eqs. (4.14) and (4.15), subscripts refer to the layer as numbered in Fig. 4.7, and I_{ij} refers to the transfer matrix from the j-th layer to the i-th layer. The transfer matrix I_{ij} is given in terms of the acoustic impedance of the layers as:

$$\boldsymbol{I_{ij}} = \frac{1}{2Z_j}\begin{bmatrix} Z_j - Z_i & Z_j + Z_i \\ Z_j + Z_i & Z_j - Z_i \end{bmatrix} \tag{4.17}$$

The propagation matrix $\boldsymbol{\Phi}_i$ is given by:

$$\boldsymbol{\Phi_i} = \begin{bmatrix} \exp -ik_i\, d_i & 0 \\ 0 & \exp ik_i\, d_i \end{bmatrix} \tag{4.18}$$

where k_i and d_i are the acoustic wave vector and the thickness of the i^{th} layer,

respectively.

Thus, we have:

$$P_3^+ = P_0^+ / \boldsymbol{S_{tot}}(1,2) \tag{4.19}$$

The value of P_3^- is considered to be zero as the medium is considered to be semi-infinite.

Then, the field can be propagated toward the spacer-gold interface as marked in Fig. 4.7 with the dashed red line. The pressure distribution at this interface is given by:

$$\boldsymbol{I}_{12}\boldsymbol{\Phi}_2\boldsymbol{I}_{23}\begin{bmatrix} P_3^+ \\ 0 \end{bmatrix} \tag{4.20}$$

The forward- and backward-propagating waves in the spacer layer can be determined by multiplying the pressure field by a propagation matrix, in which the thickness term d_i is replaced with x as indicated in Fig. 4.7, the distance from the interface.

The sum of the forward- and backward-propagating waves at x gives the total pressure at a specific distance, and the strain can be calculated with Eq. (4.12).

4.4.2 Responsivity and Bandwidth Analysis for PMMA and PDMS Spacer

PMMA and PDMS were readily available and widely used for optical and acoustical research because of their outstanding optical transparency and mechanical properties as listed in Table 4.1 [166, 168-170]. Here, they are considered for spacer material of TIR-FP.

Table 4.1 Optical and mechanical properties of PMMA and PDMS

	PMMA	PDMS
Refractive Index n	1.4958 @ 532 nm	1.3976 @ 532 nm
	1.4771 @ 1550 nm	1.3804 @ 1550 nm
Density ρ	1180 kg/m^3	965 kg/m^3
Sound Velocity (longitudinal) c_l	2757 m/s	1076.5 m/s
Bulk Modulus M	8.97 GPa	1.08 GPa

The acoustic pressure distribution inside the spacer layers made from 2.5-μm-thick PMMA and PDMS, calculated with the methods described above are shown in Figs. 4.8(a) and 4.8(b), respectively. The gold layer is much thinner than the acoustic wavelength, thus, it has little impact on acoustic performance of the structure. However, it is taken into consideration for completeness.

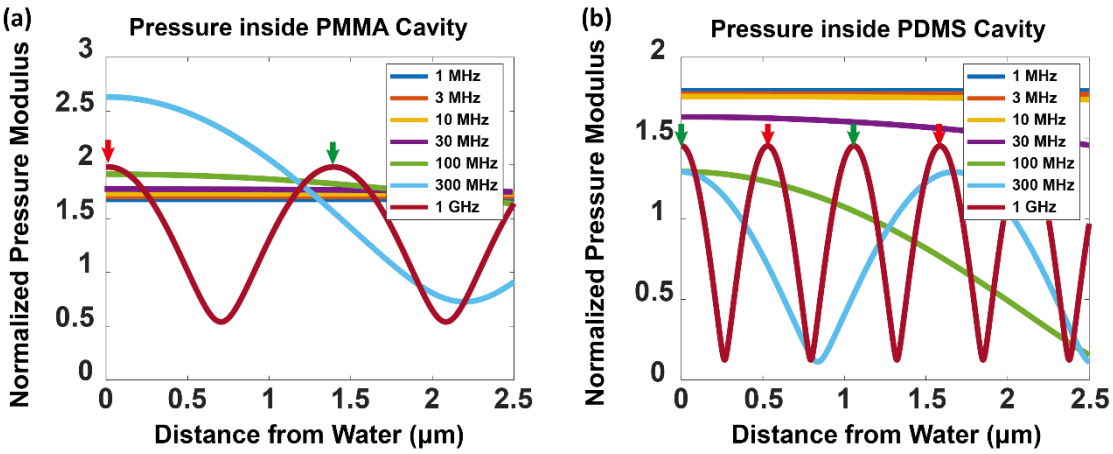

Fig. 4.8. Acoustic pressure distributions of (a) PMMA and (b) PDMS as cavity materials. The cavity-water interface is at 0 μm and the cavity-gold interface is at 2.5 μm. Blue, orange, yellow, violet, green, cyan, and brown represent input frequencies of 1 MHz, 3 MHz, 10 MHz, 30 MHz, 100 MHz, 300 MHz, and 1 GHz, respectively.

At low frequencies, the spacer layer is thin (2.5 μm) compared with the acoustic wavelength, thus, the field looks uniform. However, as the frequency increases, and the wavelength deceases to the same order as the thickness of the spacer layer, which is 300 MHz for PMMA and 100 MHz for PDMS, periodic patterns can be observed, and phase starts to cancel.

The vectorial sum of the acoustic field integrated through the structure divided by the modulus gives the total displacement per pascal at each frequency as shown in Fig. 4.9(a), where displacement is plotted against the acoustic frequency for PMMA and PDMS. Within the bandwidth, the PMMA cavity gives a displacement response of

4.95×10^{-7} nm · Pa^{-1} and PDMS gives a displacement response of 4.05×10^{-6} nm·Pa^{-1}. The 3-dB bandwidth for a 2.5-μm PMMA cavity measured in Fig. 4.9(a) is 390 MHz, whereas that for PDMS is 100 MHz.

The intrinsic trade-off between bandwidth and displacement response is demonstrated in Fig. 4.9(b) where different thicknesses of the PMMA cavity are investigated. When the thickness of the PMMA cavity increases to 25 μm, the structure can give a displacement of 4.05×10^{-5} nm·Pa^{-1}, which is comparable to 2.5-μm PDMS layer. However, the 3-dB bandwidth falls to less than 30 MHz.

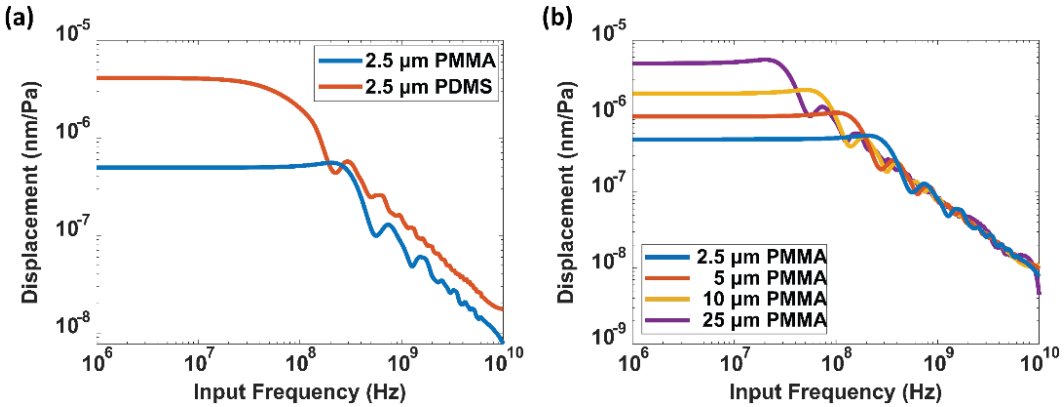

Fig. 4.9. (a) Displacement per Pa vs. input frequency for 2.5 μm PDMS and PMMA layers. (b) Displacement per Pa vs. input frequency for PDMS layers of 2.5 μm, 5 μm, 10 μm, and 25 μm.

The displacement of the structure is then combined with the optical analysis for TE polarization. The Fresnel calculations indicate that the responsivity can be considered

to be proportional to the displacement when displacement is much less than the total thickness of the spacer layer. Therefore, the optical responsivity is 3.12×10^{-7} Pa^{-1} for a 2.5-μm PMMA layer whereas that for a 2.5-μm PMMA layer is 3.04×10^{-6} Pa^{-1}.

SPR based sensors have been used in many photoacoustic sensing and imaging applications as optical detection probes [149, 171]. Theoretically, a conventional SPR produces an optical responsivity of 3×10^{-8} Pa^{-1} with an acousto-optic coefficient of 1.35×10^{-10} $\mathrm{RIU} \cdot \mathrm{Pa}^{-1}$. Therefore, the PMMA- and PDMS-based TIR-FP structures can provide orders of magnitude improvement over conventional refractive index sensing mechanism under the same excitation and detection configuration, and thus, can offer an immediate upgrade for ultrasound and photoacoustic sensing and imaging applications with competitive bandwidth performance. It should be noted that most of the mechanical properties, e.g., sound velocity, are frequency-dependent and there has been no thorough investigation in the literature of these critical mechanical properties of PDMS and PMMA in terms of frequency. Therefore, the analysis in this chapter aims to provide the theoretical framework but there may be some deviation to in the predictions due to inaccuracy in mechanical property values.

4.5 Summary

In this chapter, the concept of TIR-FP is proposed and explained. TIR-FP comprises a thin gold layer as coupler and a spacer layer to support the Fabry-Perot modes above

the critical angle for both TM and TE polarizations. Two dominant mechanisms for TIR-FP to detect acoustic waves have been discussed. Both evanescent field and propagating FP modes can be used for detection of sound waves. An acoustic pressure in the liquid interacts with the optical evanescent field, resulting in a change in local refractive index, and thus, perturbing the reflectivity. Similarly, an acoustic wave penetrating within the FP perturbs the resonant condition by changing the thickness of the spacer layer. This perturbs the resonant conditions so that the optical reflection mirrors the instantaneous pressure field from the acoustic wave.

The chapter considers the effects that limit the bandwidth of the two detection mechanisms when the wavelength of the acoustic field is commensurate the dimensions of the evanescent field (for perturbation in the couplant) with or the polymer thickness (for the mechanism based on dimensional change of the resonator).

Chapter 5 Ultrasound and Photoacoustic Sensing with TIR-FP

5.1 Introduction

Following the theoretical analysis of the total-internal-reflection based Fabry-Pérot (TIR-FP), this chapter presents the experimental evaluation of TIR-FP for ultrasound and photoacoustic sensing capability. The proposed TIR-FP structures comprise a metal layer and a polymer spacer layer deposited on top of coverslips. For a conventional Fabry-Pérot structure, there is usually an additional layer or stack of layers on top of the polymer spacer layer to provide perfect reflection, which are usually metals or crystals [13, 172, 173]. Therefore, for selection of spacer material, the compatibility between mechanical properties has to be considered, otherwise, the fabricated layers may be prone to cracking. Thus, in the applications, materials chosen for spacer are usually relatively hard, e.g., polyethylene terephthalate (PET), parylene or glass.

A major structural advantage is that there are no layers on top of the polymer spacer layer. Therefore, soft materials with small elastic modulus can be used, e.g., PDMS [174-176].

Regarding the performance, three main factors were evaluated in the experiment, i.e., responsivity, bandwidth and sensitivity. Sensitivity is related to the minimum

detectable signal in the system and is usually defined as the noise-equivalent pressure (NEP) in the unit of Pascal ($N \cdot m^{-2}$) and is given by the standard deviation of noise in the unit of Volt divided by responsivity of the transducer in the unit of V/Pa.

5.2 System Configuration

5.2.1 Experimental Setup

As discussed in Chapter 3, the incident optical beam for TIR-FP modes is above the critical angle. Therefore, two possible experimental systems were considered. The first is illumination with high-numerical-aperture (NA) objective lenses with high-NA oil for coupling, which is often used for investigating SPR based systems. With NA above 1, beams focused with objective lenses will illuminate some angles above the critical angle. However, complicated supportive components have to be included in the system in order to have a fine profile of the modes and the angle range from 0 to critical angle is not used in this experiment. As the optical wavelength is 1550 nm, infrared objective lenses with high NA tend to be more expensive than ones at visible wavelengths.

The other possible experiment configuration is prism based attenuated total internal reflection (ATR) actuated with scanning galvo mirror. Optical resonance of the TIR-FP highlights narrow FWHM in angular and wavelength domain and high responsivity to input acoustic pressure. A scanning mirror can be used in the system to

resolve the narrow linewidth of the resonance, and the incident angle can be fixed when recording the intensity variation with respect to the input acoustic wave. Wavelength profiles of resonances can be recorded by tuning the tunable laser.

Fig. 5.1 shows a schematic of the experimental system and Fig. 5.2 shows a photograph of the experimental system. The source of the interrogation was an infrared tunable laser (TSL-710, Santec Corp., Japan) with fiber-coupled output. The beam was linearly polarized, and the wavelength can be tuned from 1480 nm to 1620 nm with a maximum flat output of 20 mW. The polarization can be adjusted using an achromatic half waveplate (AHWP10M-1600, Thorlabs, USA) for pure TM or TE output. Then, the beam was expanded with lenses L1 (f=100mm, Thorlabs, USA) and L2 (f=150mm, Thorlabs, USA) for a more uniform intensity distribution at the center. After beam expansion, the beam is reflected onto the customized galvo mirror (GM in Fig. 5.1). The galvo mirror consists of a silver mirror (PF10-03-P01, Thorlabs, USA) mounted on the center of a motorized rotation stage (HDR50/M, Thorlabs, USA). The motor was connected to a controller and computer interface (BSC201, Thorlabs, USA) and then connected to a computer for synchronized acquisitions. The beam was then projected onto the sample and split with a beam splitter and collected with two photodetectors (PD). PD1 (PDF10C2, Thorlabs, USA), with a bandwidth ranging from DC to 20 Hz, was designed to monitor and compensate for drift of the DC signal and PD2 (PDA05CF2, Thorlabs, USA), with a bandwidth of 150 MHz, was connected

to an oscilloscope and used for data acquisition.

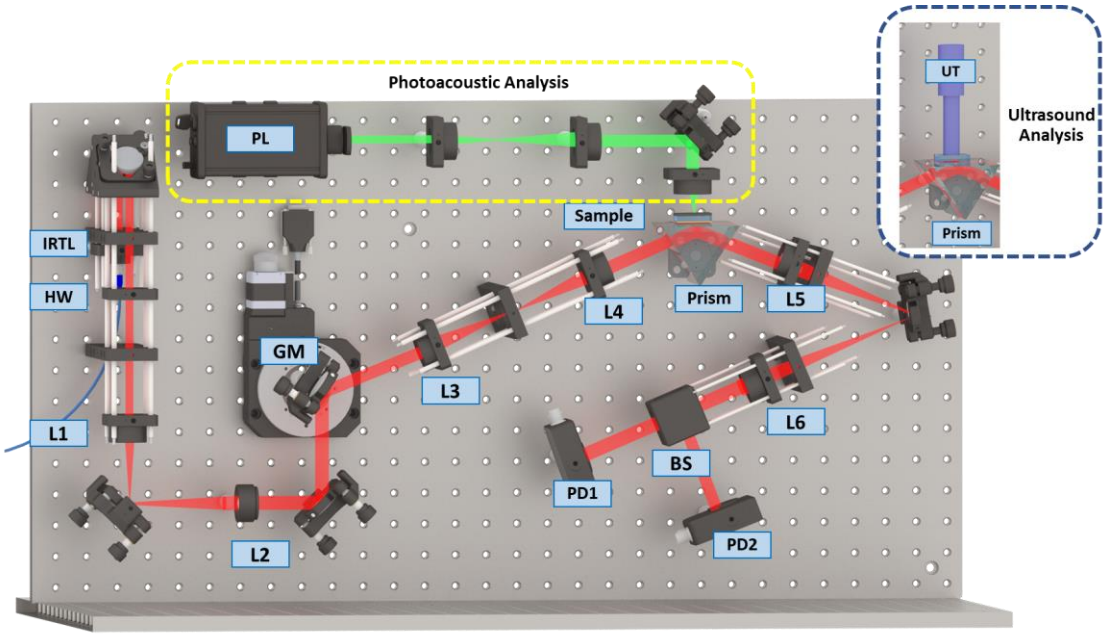

Fig. 5.1. Experimental setup. IRTL: infrared tunable laser; HW: half waveplate; GM: galvo mirror; PL: nanosecond pulse laser; UT: ultrasound transducer; BS: beam splitter; PD: photodetector.

Lenses L3-L5 were achromatic lenses with 100 mm focal length. Lens L6 were 200 mm focal length. L3 and L4 were used to project the beam onto the structure. L5 and L6 were used to collect the beam. Essentially, two lens pairs formed two 4f systems, therefore, the GM, the structure and photodiodes of PD were on the conjugate plane of each other, so that when GM rotated, illuminated areas on PD almost did not change significantly. A small change may be introduced since the prism is equilateral, light paths may differ by a small amount for different incident angles.

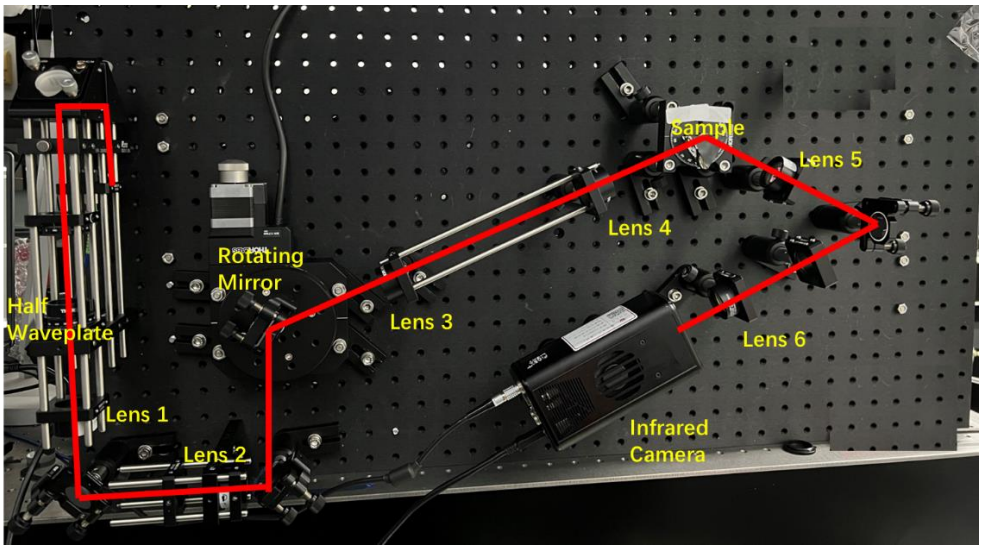

Fig. 5.2. A photograph of the experimental system.

Resonance profiles in angular and wavelength domain were achieved by rotating the rotation stage or tuning the laser wavelength, respectively. A Python script was developed to issue a command for tuning or rotation while triggering the oscilloscope to record the data and transmit back to the computer for processing. Another commonly used approach would be to use LabView and DAQ cards. However, the oscilloscope is more straightforward for optimizing the system. The acquired profiles were temporal sequences. Knowing the tuning speed, the measurement time may be converted to angle or wavelength.

Responsivity analysis was carried out with an ultrasound transducer (UT) as indicated in the blue square of Fig. 5.1. The ultrasound transducer was connected to a pulser-receiver (DPR300, Imaginant, USA). The ultrasound transducer was calibrated with a PVDF hydrophone (HMB-200, Onda Corp., USA). The generated ultrasound

signals have a center frequency of 15 MHz with 16 amplitude levels. 16 amplitude levels correspond to 129 kPa, 161 kPa, 198 kPa, 232 kPa, 265 kPa, 299 kPa, 332 kPa, 364 kPa, 390 kPa, 422 kPa, 452 kPa, 479 kPa, 509 kPa, 534 kPa, 560 kPa and 585 kPa acoustic pressure, respectively. The acquisition sequence was synchronized with the sync signal out of the pulser-receiver. 16 responses were recorded for each structure. An automated program was developed with Python 3.9 to control the rotation stage, the oscilloscope and the pulser-receiver via Thorlabs APT and Visa interfaces.

Bandwidth analysis was implemented with photoacoustic sensing as indicated in the yellow square of Fig. 5.1. This is needed because the generated photoacoustic signal has a much larger bandwidth compared to the commercial ultrasound transducers. The ultrasound transducer was replaced with a nanosecond pulse laser at 532 nm (CGGC, China) with 5kHz repetition rate. The pulse width of the nanosecond laser was 3.4 ns as measured with the oscilloscope. Laser pulses were focused onto an absorbing layer located a few millimeters above the structures with a 50-mm achromatic lens.

Sensitivity analysis was carried out with the UT. The driver of the UT was switched to a function generator rather than the pulser-receiver since the amplitude of the pulser receiver was on the order of magnitude of 10^5 Pa, which is far above the scale of the estimated sensitivity. On the other hand, a function generator can generate

nanosecond pulses with as low as 0.1 V amplitude, which corresponds to an acoustic amplitude of ~100 Pa.

In responsivity and bandwidth analysis, conventional SPR sensors were used to benchmark the proposed TIR-FP transducer since all other elements of the system are similar. An alternative is to use conventional Fabry-Perot structure as the reference. However, there would be many uncontrolled variables affecting the results as they would be investigated in two separate systems and the optical path would be different for different incident angles. Thus, the comparison would be much more difficult to control. SPR can be investigated within the shared system as the mode excitation angle is similar to TIR-FP. Although SPR was mainly used for refractive index sensing based applications, there have been continued research interests with it in the related area [82]. Therefore, SPR was chosen as the benchmark reference.

5.2.2 Sample Preparation

Three batches of samples were prepared. SPR samples were prepared by depositing a 38-nm-thick gold layer on top of the N-BK7 coverslip substrate with a sputter (Nano 36, Lesker, USA). The dimensions of the samples were optimized for 1550 nm wavelength.

For TIR-FP samples with TE polarization, a 12-nm gold layer was deposited first with the sputter on top of coverslips. Theoretically, for TE polarization, the thickness of the gold layer varying from 5 nm up to 15 nm can support TIR-FP resonance with

high Q and good variation between minimum and maximum intensity as shown in Fig. 5.3. However, practically, there are several constraints limiting minimum thickness of the gold layer, e.g., surface roughness, surface tension and deposition techniques, and ultra-thin films (<10 nm) are subject to island formation resulting in deviation of optical properties from simulation [177]. Therefore, 12 nm was chosen in a good compromise between film quality and theoretical performance.

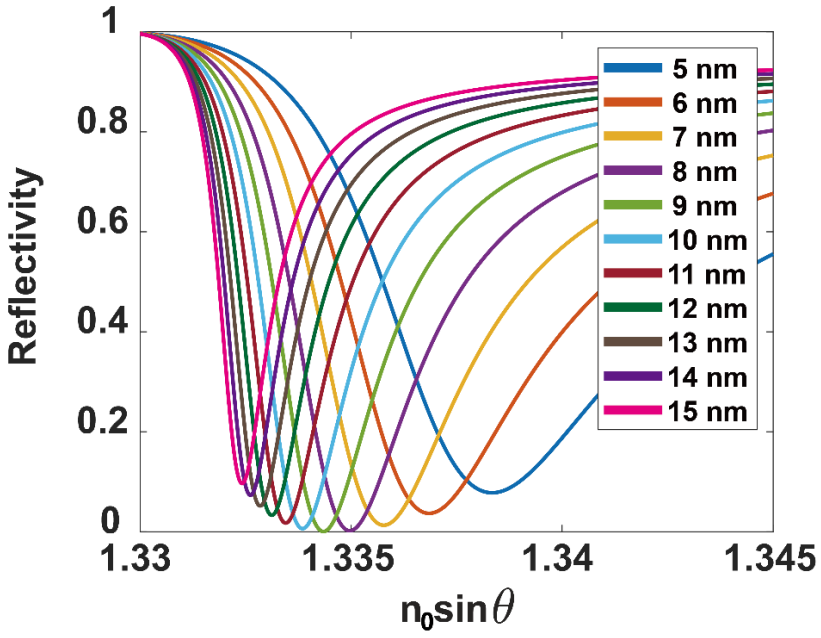

Fig. 5.3. TIR-FP resonance with gold thickness varying from 5 nm to 15 nm.

Two batches of TIR-FP samples were fabricated with PMMA 950k and PDMS as the spacer layer, respectively. PMMA used was AR-P 672.08 from Allresist GmbH and PDMS used was Sylgard 184 with 10:1 base elastomer/curing agent mixing ratio.

The polymer layers were coated with a spin coater and their thickness was measured with a surface profiler. The thickness of the PMMA layer was 1.9 μm, and the thickness of the PDMS layer was 3.4 μm.

5.3 Responsivity Analysis

5.3.1 SPR

Results for the conventional SPR sample are presented first in Fig. 5.4 for future comparison and reference of the proposed TIR-FP. The angular profile of the SPR sensor is shown in Fig. 5.4(a). The wavelength profile is not displayed because the linewidth of the wavelength profile for the resonance is broad. The angular profile was acquired via a Python script which triggered the motorized stage to rotate at a speed of $0.1°{\cdot}s^{-1}$ continuously. Meanwhile, the oscilloscope was triggered to record the data at a sampling rate of 50k points per second.

The displayed profile in Fig. 5.4(a) was normalized with respect to the maximum value of the measurement. The FWHM of the measured profile is 1.08×10^{-2} in the unit of $n_0 \sin\theta$ (equivalent to 0.89°) as indicated in Fig. 5.4(a). Marker A in Fig. 5.4(a) indicates the operating point for responsivity analysis, which is the point with the maximum slope.

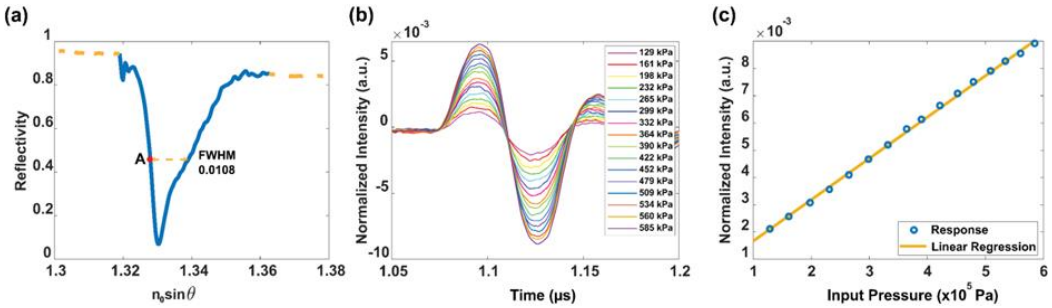

Fig. 5.4. Results for SPR sensor. (a) Reflectivity measured via angle scanning, (b) responses of 15 MHz ultrasound transducers to various input acoustic pressures, and (c) maximum recorded responses with respect to the input acoustic pressures.

Fig. 5.4(b) shows the 16 normalized temporal responses acquired with the 15 MHz UT corresponding to 16 input amplitudes. The absolute values of maxima in temporal responses are plotted against the input acoustic pressures in Fig. 5.4(c) and a linear regression is performed. The result shows excellent linearity with an R^2 of 0.9985. The slope of the linear fitting can be converted to the responsivity of the SPR transducer, which is 1.517×10^{-8} Pa^{-1}. The value agrees with the maximum responsivity of 1.63×10^{-8} Pa^{-1} reported in Ref. [100, 143].

5.3.2 PMMA-based TIR-FP

SPR can be excited solely using TM polarization. Therefore, SPR samples also function as a tool to calibrate the axis of the half waveplate and control the polarization in the system.

For TIR-FP, both TM and TE can be used for sensing. However, with the same thickness of gold layer, the TE polarization tends to show a smaller loss than the TM polarization, thus resulting in a narrower FWHM of the resonance compared to the TM mode. The TE polarization thus exhibits better performance compared with TM. This advantage is even more enhanced in practice, where gold thickness of TE is thinner than that of TM. Therefore, experimental studies of the designed TIR-FP structure were implemented with TE polarization.

In the experiment, after TM polarization was used for SPR excitation, the waveplate was further rotated 45 degrees to ensure TE polarization. The wavelength of the laser was initially fixed at 1550 nm, and the angle was then fixed and fine-tuned so the wavelength was tuned slowly until the operating point with maximum response was reached. The operating point is roughly at the value where the reflectivity is halfway between the maximum and minimum corresponding to the largest gradient.

For angular profiles, the rotation stage rotated at a speed of $0.01°{\cdot}s^{-1}$, which is 10-time slower than the scanning for the SPR measurement, since the FWHM for TIR-FP is much narrower than that for SPR. Wavelength profiles of TIR-FP sensors were acquired with a wavelength tuning speed of 5 nm per second.

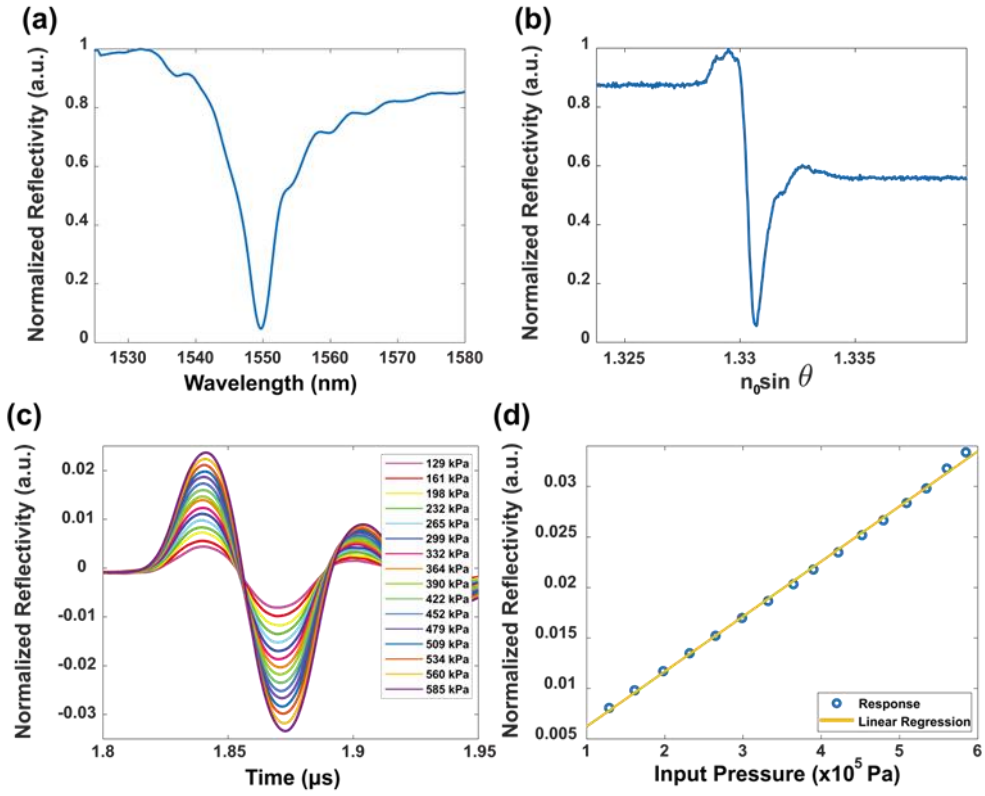

Fig. 5.5. Results for PMMA-based TIR-FPs. (a) wavelength and (b) angular scanning profiles for Reflectivity of PMMA measured at 1550 nm, (c) response of 15 MHz UT to various input acoustic pressures, and (d) maximum recorded responses vs. the input acoustic pressure.

Fig. 5.5(a) shows the wavelength profile of the TIR-FP resonance with a 1.9-μm PMMA layer. As measured from the profile, the FWHM of resonance is 8.68 nm. Fig. 5.5(b) shows the angular profile of the PMMA-based TIR-FP resonance, the FWHM of which is 9.5×10^{-4} in units of $n_0 \sin\theta$. 16 temporal responses are illustrated in Fig. 5.5(c) corresponding to 16 pressure amplitudes from the 15 MHz UT controlled by the pulser. The absolute values of maximum values in the temporal responses are

marked in Fig. 5.5(d) with respect to the input pressure. A linear regression is performed to extract the responsivity with excellent linearity ($R^2 = 0.9999$). The responsivity is 5.45×10^{-8} Pa^{-1}, which is a 3.6-fold improvement compared with the conventional SPR sensor measured in the same system.

5.3.3 PDMS-based TIR-FP

For the investigation of TIR-FP with a PDMS layer, polarization was maintained as TE polarization. Fig. 5.6(a) shows the normalized spectral profile of resonance and the spectral FWHM measured is 12.8 nm. Fig. 5.6(b) shows the normalized angular profile of resonance, the FWHM of which is 3.8×10^{-4} in units of $n_0 \sin\theta$. Compared with PMMA based structures, the spectral FWHM is about 50% wider and the angular FWHM is about 60% narrower. For better display of the results, a 3-order Savitzky-Golay filter and down-sampling were applied in all angular and spectral profiles regarding PMMA and PDMS structures, otherwise, there would be too many points of data from the oscilloscope to process. The filter effectively smoothed the data and filtered out random noise and interferences of small period in the optical system due to multiple reflection, which overlapped with the resonance of interest. The resonance dip of PDMS is shallower than that of PMMA and SPR. This can be partly explained by a recent study where a small imaginary part has been observed in the refractive index of PDMS at 1550 nm [166].

Fig. 5.6(c) shows the normalized temporal responses with the UT. Their maximum

values were plotted in Fig. 5.6(d) against the calibrated input pressure. A responsivity of 4.6×10^{-7} Pa^{-1} at 15 MHz was observed from the linear regression in Fig. 5.6(d), which is a 30-fold improvement over the conventional SPR structure.

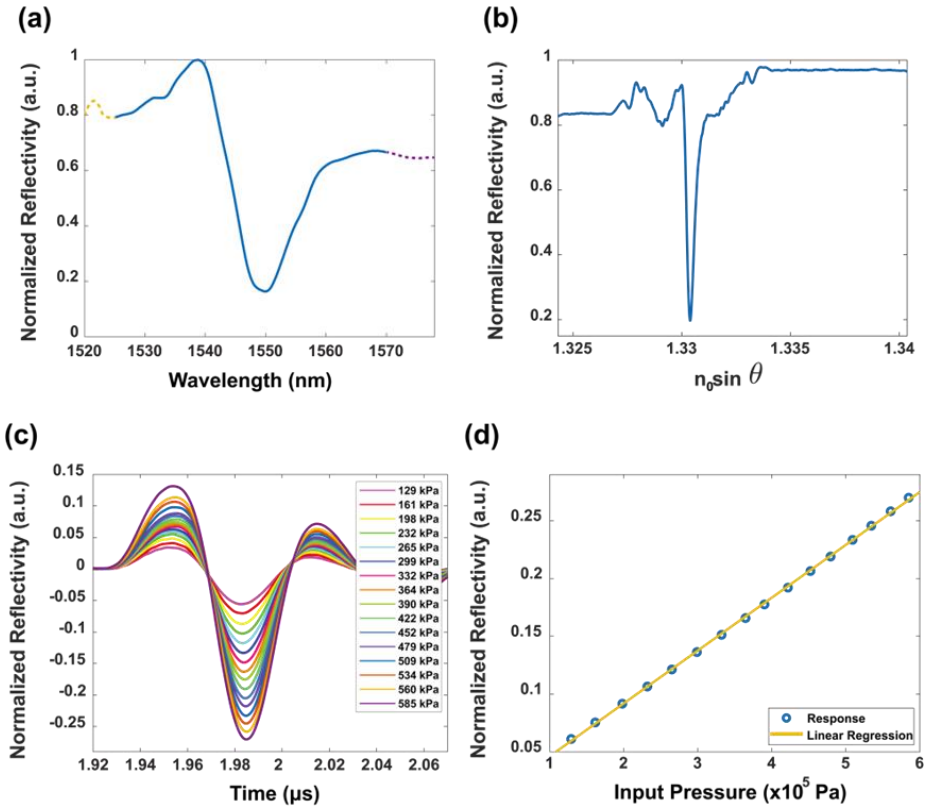

Fig. 5.6. Results for PDMS-based TIR-FPs. (a) wavelength and (b) angular scanning profiles for Reflectivity of PMMA measured at 1550 nm, (c) response of 15 MHz UT to various input acoustic pressures, and (d) maximum recorded responses vs. the input acoustic pressure.

For a conventional FP structure, consisting of a 20-μm thick polyethylene

terephthalate (PET) layer between 10 nm and 100 nm gold layers, the typical responsivity is approximately 4.6×10^{-7} Pa^{-1} [143]. The result is comparable with that of the proposed PDMS-based TIR-FP, although the mentioned conventional FP structure usually has a bandwidth of only 40 MHz or less due to the much greater thickness. It will be seen in Section 5.3 that bandwidth of the proposed transducer is considerably greater.

5.4 Bandwidth Analysis

Bandwidth is another important parameter characterizing an acoustic sensor. However, commercial piezoelectric UTs usually have narrow bandwidths. In the case of the 15 MHz UT from Olympus, the bandwidth is 4 MHz. So usually, in order to characterize the performance with a bandwidth of 100 MHz, the conventional approach would require multiple UTs centered at different frequencies [100]. The process can be tedious and the different UTs need careful placement and alignment. Another approach is to detect a photoacoustic signal excited from an absorbing layer. A spectral comparison between the generated signal with the acquired signals gives the bandwidth performance of the structures. For this method, the bandwidth of the generated photoacoustic signal is dependent on the material and the duration of the exciting laser pulse. Generally speaking, soft materials generate narrow bandwidth signal with low center frequency. Therefore, graphene is selected as the absorbing material for its stiffness and high absorption.

Figs. 5.7(a)-5.7(c) shows the normalized temporal responses of the generated photoacoustic signal for the SPR, PMMA- and PDMS-based TIR-FP resonators, respectively. Fast Fourier transforms (FFT) were performed for the three responses and displayed in Fig. 5.7(d). As a reference of the TIR-FP, the acquired bandwidth for the SPR is 113 MHz measured from FFT in Fig. 5.7(d). The bandwidth for PMMA-based TIR-FP is 110 MHz and that for PDMS-based TIR-FP is 75 MHz.

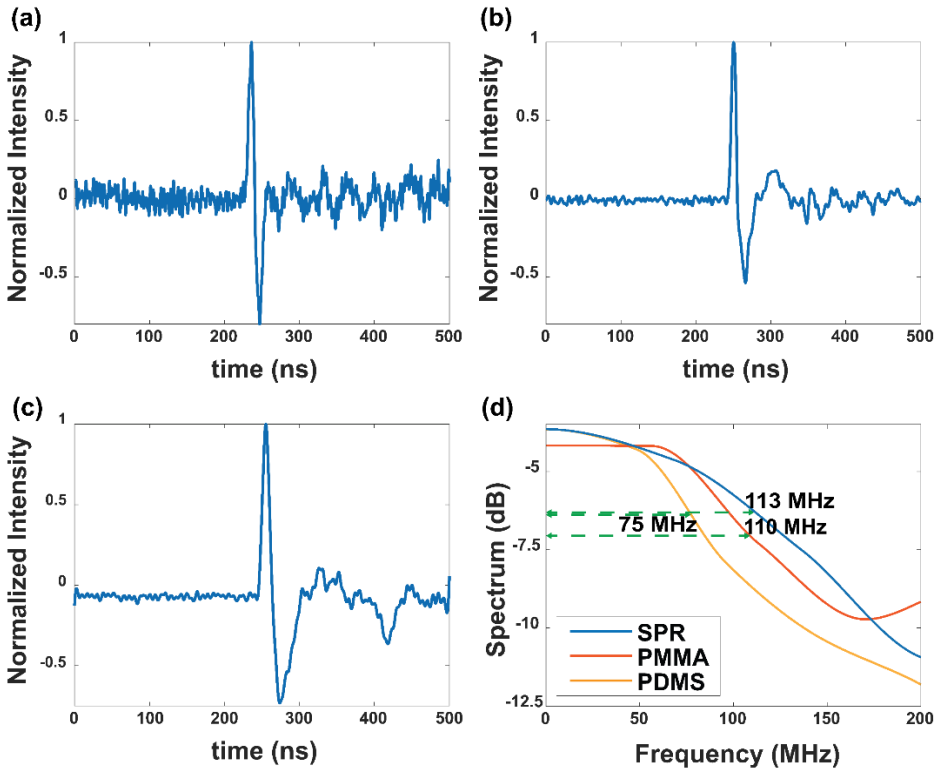

Fig. 5.7. Photoacoustic results for the (a) SPR, (b) PMMA-, and (c) PDMS-based TIR-FPs and (d) their FFTs for the bandwidth analysis.

5.5 Sensitivity Analysis

For sensitivity analysis, NEP was evaluated. NEP effectively means the pressure level at a signal-to-noise ratio (SNR) of 1. The value cannot be directly measured but can be calculated by extrapolating response versus pressure down to the noise level. In general, small NEP is desired since it optimizes the precision of the measurement and also allows the use of lower power for a given SNR and fast scanning for photoacoustic imaging.

A typical NEP of acoustic transducers based on SPR is of the order of thousands of Pascals. Given the improvement in responsivity, an NEP of a few hundred can be expected for PDMS-based TIR-FP. However, the amplitude of pulse generated by pulser is huge as input pressure of Section 5.4 ranges from 129 kPa to 585 kPa, which differs from the estimated NEP by three orders of magnitude. Therefore, the pulser was replaced with a function generator (33622A, Keysight, USA), which can generate pulses with an amplitude as low as 0.1 V with good SNR. To avoid quantization error of the oscilloscope for small signals, a DC blocker and an analog amplifier was added between the PD2 and the oscilloscope. The sensitivity measured with this approach is more convincing compared to extrapolation directly from the responsivity measurement in Section 5.2.

The combination of the function generator and the ultrasound transducer was calibrated with the hydrophone (HMB-200, Onda Corp, USA) for the amplitude

voltage range of 1 V to 9 V. For amplitudes lower than 1 V, responses of the hydrophone fall far below the voltage per division limit of the oscilloscope, which is 1 mV/div and the signal was blurred by quantization error, and random noise became significant compared to the hydrophone signals. Therefore, we have to extrapolate the pressure values for amplitude levels below 1 V assuming a linear relationship between pressure and voltage. Since the response of the TIR-FP in this range appeared linear, we can confidently say that the extrapolation to low voltage level for noise-equivalent sensitivity is valid.

The response maximums of the PDMS-based TIR-FP is plotted against each incident pressure from calibration or extrapolation as shown in Fig. 5.8(a). The results demonstrate excellent linearity of TIR-FP response and incident pressure with small values from 180 Pa up to 10 kPa. The response of the system was measured to be 301.75 mV per 1 kPa. In order to reduce effects of noise and evaluate responses of the TIR-FP with small signals with more precision, a temporal averaging of 9 was applied during the evaluation. This averaging should provide a 3-fold improvement in SNR, and this allows us to make a valid measurement of the signal at the single-shot noise level. It must be emphasized that although averaging was used to assess the sensitivity, any values of NEP were converted to single shot measurement.

In a separate measurement of the noise levels, no averaging was applied. The noise levels were recorded from -1.26 μs to -0.26 μs. The minus sign indicates time before

the pulses were generated. The noise level was 48.47 mV as shown in Fig. 5.8(b). Therefore, the NEP of the system is about 160 Pa. The main noise type in the system was additive Gaussian noise since no obvious increases in NEP was observed when increasing the gain of the amplifier. A comparable sensitivity level was measured after an interval of 7 days. Therefore, no obvious deterioration in responses and sensitivity was observed.

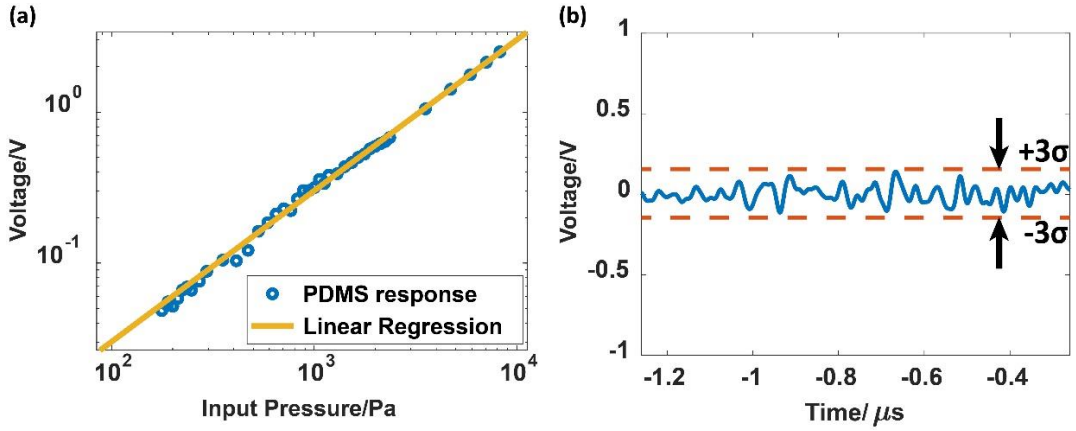

Fig. 5.8. (a) Response of PDMS based TIR-FP with a function generator as the driver of the ultrasound transducer. The data is marked in blue dots and its linear regression is marked in a yellow line. (b) Single-shot noise level recorded before ultrasound trigger with no averaging.

5.6 Discussion

In the current system, PMMA- and PDMS-based TIR-FPs were examined for responsivity, bandwidth and sensitivity. In the analysis of responsivity and bandwidth,

an SPR sample was also tested as a benchmark against the TIR-FP samples within the same experiment system. A 30-fold improvement in responsivity over SPR was observed with slightly a deteriorated bandwidth of 75 MHz for PDMS. For PMMA, a 3.6-fold improvement in responsivity was observed with a comparable bandwidth of 110 MHz. An NEP of 160 Pa was observed for PDMS-based TIR-FP. These results indicated huge potential of TIR-FP for ultrasound and photoacoustic sensing and imaging applications. Compared with conventional FP structures, incidence above the critical angle means longer light path for a given thickness of cavity, which gives more responsivity, while remaining the same thickness, which means the comparable acoustic bandwidth performance. Compared with the SPR-based photoacoustic transducers using similar investigation systems, the responsivity of TIR-FP is significantly greater.

Further improvements can be made to further enhance the performance. As previously discussed, NEP is dependent on both SNR of the system and responsivity of the transducer, and an intrinsic trade-off exists for responsivity and bandwidth. Therefore, two possible approaches to improve sensitivity would be (i) to improve SNR and (ii) to improve responsivity.

Since the nature of the noise within the system is mainly additive Gaussian white noise, adopting phase interrogation or an additional reference beam for cancellation of noise would significantly reduce noise and improve SNR [103, 178]. Since sensing

with TM and TE has different resonance angles, the counterpart polarization can be used as *in-situ* reference for reduction of common-path noise [148].

Given the current bandwidth of the transducer is 75 MHz for PDMS-based TIR-FP, if a thicker spacer was used, the NEP can be estimated to be less than 50 Pa in the same interrogation system, while still maintaining a respectable bandwidth (>20 MHz) for microscale photoacoustic imaging applications. It is worth noting that the current bandwidth for the PMMA transducer is somewhat restricted by the bandwidth of the PD and the amplifier. Further improvement over the current bandwidth can be achieved with a faster PD and amplifier.

In these experiments, two widely used materials were coated, i.e., PMMA and PDMS. Mechanical properties set the baseline of the trade-off between responsivity and bandwidth. Further fine control over the spacer thickness can allow fine tuning of the trade-off. Other materials, e.g., parylene, can potentially provide more durability and be more appropriate for mass production than PMMA [179, 180]. The spacer can serve as a protective layer for the metal layer, preventing oxygen and water, therefore, silver or silver-gold alloys can be used to avoid oxidation [181-183].

It should be noted that since the pulse repetition rate of these experiments were relatively low (1 kps), the thermal-optic effect was not significantly observed. However, for future experiments including high-speed photoacoustic imaging, additional measures should be taken to control the local temperature drift on the

sample and to compensate for temperature drift with an additional reference beam and related electronics.

5.7 Summary

In this chapter, TIR-FP structures with PMMA and PDMS spacer layers were experimentally demonstrated. The structures were investigated in an intensity-interrogation based system with Kretschmann configuration for investigation above the critical angle, which is similar to that used for other optical surface wave based optical sensors [100, 104]. An SPR sample was also tested within the same experimental system as a benchmark against the TIR-FP samples. The proposed TIR-FP structures with PMMA and PDMS exhibited responsivities of 5.45×10^{-8} Pa^{-1} and 4.5×10^{-7} Pa^{-1}, respectively, indicating an enhancement of 3.6- and 30-fold over the conventional SPR sample measured in the same system. The structures showed estimated bandwidths of 75 MHz and 110 MHz for PDMS and PMMA respectively when investigated with broadband photoacoustic signals. An NEP of 160 Pa was recorded with the transducer driven by the function generator.

Chapter 6 Grating based Fabry-Pérot Resonator as an Ultra-Sensitive Ultrasound and Photoacoustic Transducer

6.1 Introduction

As non-destructive and non-invasive evaluation techniques, ultrasound and photoacoustic sensing has been developing rapidly and draws increasing research interests towards more sensitivity and broader bandwidth. The field was conventionally dominated by piezoelectric transducers. In recent years, optical detection mechanisms have emerged as a contender for ultrasound and photoacoustic sensing and imaging because of their high sensitivity and wide bandwidth capability. One well-established sensing mechanism discussed in this thesis is the Fabry-Pérot resonator.

A typical Fabry-Pérot resonator is a simple structure with a polymer layer sandwiched between one highly reflecting layer and one partially reflecting layer and the resonator is usually excited with a laser source of normal incidence [184]. The typical reflecting layers include metal layers, e.g., gold, silver, and dielectric structures, e.g., Bragg reflectors, where pairs of two types of photonic crystal with different refractive indices and thickness equivalent to λ/4 stack [93, 96]. For adequate reflectivity from the reflecting layers, there are usually more than 4 pairs, that is 8

layers of photonic crystal with a total thickness exceeding 1 μm [155]. However, compared with simple metal layers, fabrication process of the lossless Bragg reflectors can be complex and have low yield, especially when the layers are fabricated on top of a soft polymer layer, since there are at least two orders of magnitude difference in elastic modulus between a conventional polymer material and the constituents of photonic crystals. Another issue is with the intrinsic dynamic range. Bragg-reflector based resonances tend to have good sensitivity performance. However, sensitive detection can be easily saturated. Therefore, variable intrinsic dynamic range is needed to accommodate signals with large amplitude variation.

The principal sensing mechanism for Fabry-Pérot (FP) structures to detect acoustic waves arises from the deformation of the polymer layer as discussed in the previous two chapters. Another mechanism is the refractive index of the polymer layer is modulated by the acoustic pressure, which is essentially the elasto-optic effect. However, for conventionally used polymers, e.g., PET or Parylene, this effect is less significant compared to the former mechanism. Regardless of the mechanisms, the acoustic wave induces a change in optical path length, which results in a shift in resonance condition and can be detected with a photodetector. Sensitive FP transducers based on the mechanism have been developed and applied to ultrasound and photoacoustic imaging.

There has been extensive work on guided mode resonance, where the diffraction

grating is one of the most fundamental elements. Two of the widely used optical gratings are deep subwavelength grating and diffraction grating, where the period of grating is far less or larger than the interrogation wavelength, respectively. The following is diffraction relation of the grating vectors and wavevectors of different diffracted orders.

$$\frac{2\pi}{\lambda_0} n_{out} sin\theta_{out} = \frac{2\pi}{\lambda_0} n_{in} sin\theta_{in} + mk_g, m = 0, \pm 1, \pm 2, \ldots \quad (6.1)$$

where *n* is the refractive index of the medium, *m* is the diffracted order, $k_g = 2\pi/d$ is the grating vector and d is the grating period; subscript in and out denotes the incident medium and exit medium.

As a specialized structure with well-defined dimensions, high contrast grating (HCG) was proposed and has gained significant attention in the field of photonics and integrated optics [185-187]. The concept of HCG arises from the field of diffraction gratings, which are periodic structures that convert energy between different diffracted orders of light [186]. Unlike the conventional diffraction gratings, HCG are designed to have very high refractive index contrast between the grating bars and the surrounding media. This high contrast of refractive index enables precise control over the manipulation of light. By adjusting the period, duty cycle, grating depth, HCG can be engineered to reflect or transmit light with high efficiency (nearly 100%) at a desired wavelength with high quality factor Q or within specific bandwidth functioning as an optical filter. The key feature of the HCG is that it allows only two

modes to propagate in the grating structure and just a single propagating mode outside. This places severe constraints on the energy partition which leads to powerful properties. This places well defined constraints on dimensions and properties of the structure. The period of the grating has to fall in a well-defined range between the wavelength inside the high refractive index medium and the low refractive index medium.

In this chapter, a grating based FP (GFP) structure is presented with the aim for ultrasound and photoacoustic sensing. Although this structure is quite different from the high contrast grating it shares the feature that few modes exist in the cavity and only a single mode exists outside. In the structure, no lossy components (metal) are used, instead, two subwavelength grating layers are used as reflectors. The period of the grating is well defined so that only two modes propagate inside the FP cavity and only the zero-th order propagates outside the structure. In the structure proposed the zero order and the two first order diffracted beams propagate, since these have the same phase velocity the condition for two modes withing the cavity is satisfied. The structure is capable of operating as a high-Q resonator, a broadband reflector and 100% transmission. Within the same structure, among different resonance peaks, variation of Q can be greater than 3 orders of magnitude. Simulation is obtained with a proposed coupled-Bloch-mode model and always compared with rigorous coupled wave analysis (RCWA) for verification in the defined wavelength range.

6.2 Theoretical Analysis of GFP

6.2.1 Brief Revisit of the Fabry-Pérot Resonator

Fig. 6.1 shows a simplified schematic of the FP resonator where a polymer layer is sandwiched between a partial reflector for light coupling and a total reflector to allow maximum light reflection. FP resonators operate by a change in thickness *h* marked in Fig. 6.1 as the acoustic wave impinges on the resonator.

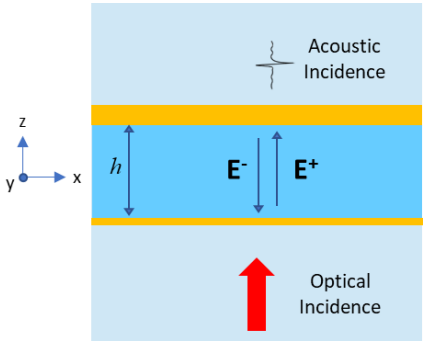

Fig. 6.1. Schematic diagram of the conventional Fabry-Perot resonator.

Two major issues faced by the conventional FP that affect the acoustic field distribution inside the polymer cavity: the backing material and the thickness of the transducer. For metal reflectors, the thickness of the partial reflector is less than 20 nm and that for the total reflector is more than 100 nm. The thickness is significantly less than the acoustic wavelength. A stiff backing layer means the acoustic pressure that is seen by the transducer is almost doubled compared to the input pressure. For a backing layer with similar acoustic impedance to the transducer, the pressure imparted

onto the transducer similar to the incident pressure of the sound wave [184]. The thickness issue resembles the trade-off argument between sensitivity and bandwidth discussed in Chapter 4 [164]. As the thickness increases, strain is integrated over a larger range, and transducer response is increased. However, as the thickness increases to a comparable level to the wavelength, the strain, as a phasor, starts to cancel out, therefore, the detection bandwidth of the transducer is limited.

Fig. 6.2 shows the integrated pressure with total thickness normalized to the acoustic wavelength of 2π and the acoustic impedance of the incident medium (water) normalized to 1. Green curve represents the case with a normalized transducer impedance of 2 and a very hard backing layer with a normalized acoustic impedance above 1000, the red curve represents the case with a normalized transducer impedance of 2 and a backing layer with a normalized acoustic impedance of 1, and blue curve represents the case with a normalized transducer impedance of 4 and a backing layer with a normalized acoustic impedance of 1. It can be seen from Fig. 6.2 that for thicknesses less than $\pi/6$, the gradient of the red curve is about half that of the green curve.

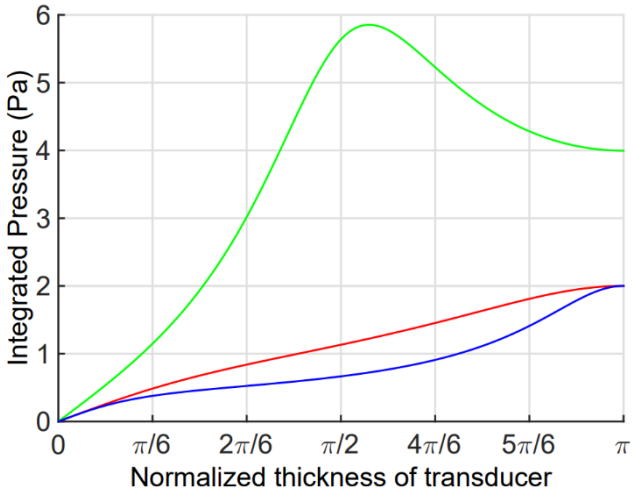

Fig. 6.2. Integrated pressure vs. normalized thickness of transducer (acoustic phase delay) across the transducer for a unit pressure wave input. The incident medium has a normalized impedance of 1. The green curve represents the case where normalized transducer impedance is 2 and backing normalized acoustic impedance is above 1000. The red curve represents the case where normalized transducer impedance is 2 and backing impedance is 1. Blue curve represents the case where normalized transducer impedance is 4 and backing impedance is 1.

With the estimation of the mechanical responses to a given pressure, a change in optical reflectivity can be determined. Fig. 6.3 shows the relative change in reflectivity for an FP resonator with 0.1 nm thickness displacement and various thickness of thin metal layer, i.e., 5 nm, 10 nm and 15 nm for the red, green and blue curves, respectively. The input refractive index used in the calculation is 1.52,

whereas that of the polymer cavity is 1.57. It can be seen that the thickness of the thin metal layer affects the Q of the resonator peak sensitivity. In practice, most transducers operate with a 10 nm or 15 nm gold since below 10 nm, gold thin film is prone to island formation. Therefore, the peak response is approximately 0.04 nm^{-1} and 0.08 nm^{-1} for 10 and 15 nm gold, respectively.

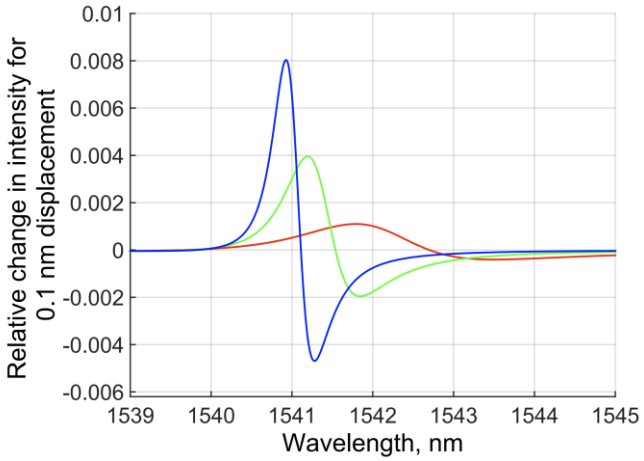

Fig. 6.3. Response of 50 μm thick Fabry-Perot resonator as a function of wavelength. Red, green and blue curves represent the cases with 5, 10 and 15 nm for thickness of the thin metal layer.

6.2.2 Condition for GFP Modes

Fig. 6.4 shows a schematic of a simplified GFP structure where the schematic is separated into three regions. Region 1 is the substrate with a refractive index of n_1 and the interrogation optical beam illuminates the structure from region 1. Region 2 is

the GFP consisting of a homogeneous polymer layer sandwiched between two grating layers of an identical period. For simplicity, it is assumed that the grating dimensions of the two grating layers are the same. Here, the grating and homogeneous layer are considered to have the same refractive index of n_2. Region 3 with a refractive index of n_3 is the superstrate of the structure and where the acoustic wave is projected onto the structure.

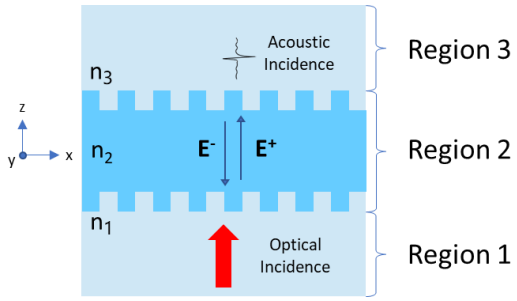

Fig. 6.4. Schematic diagram of the double-layer grating Fabry-Perot resonator. Essentially, compared with conventional FP resonators, the mirror reflectors are replaced by a diffraction grating.

Assuming normal incidence, since only one propagating wave is allowed in regions 1 and 3, and two non-degenerate modes are allowed in region 2, relationships between the refractive indices and wavelength can be worked out from Eq. (6.1).

Because there is only one propagating diffracted order, i.e., zero-th order, in region 1 and region 3, this means that any diffracted beam must be evanescent. That is

$$sin\theta_1 = \frac{\lambda_0}{n_1 d} > 1, sin\theta_3 = \frac{\lambda_0}{n_3 d} > 1 \quad (6.2)$$

$$\lambda_0 > n_L d \tag{6.3}$$

where θ_1 is the incident angle from the region 1 and θ_3 is the exit angle into the region 3 of the zero-th order, λ_0 is the free-space interrogation wavelength and n_L is the largest of n_1 and n_3.

There are at only the ± 1 diffracted orders inside the polymer layer, i.e., zero-th and first orders, so the first order is propagating, and second order is evanescent, therefore,

$$sin\theta_2 = \frac{1\lambda_0}{n_2 d} < 1, sin\theta_2 = \frac{2\lambda_0}{n_2 d} > 1 \tag{6.4}$$

$$n_2 d > \lambda_0 > \frac{n_2 d}{2} \tag{6.5}$$

where θ_2 is the propagation angle of the diffracted ± 1 orders.

To summarize,

$$\lambda_0 > n_L d \; and \; \frac{n_2 d}{2} < \lambda_0 < n_2 d \tag{6.6}$$

where n_2 and n_L are the refractive indices for the polymer layer and surrounding media, respectively.

The major difference between the GFP and a conventional FP resonator is that the grating layer scatters the incident light into two (or fewer) propagating modes that resonate inside the cavity. The mode conversion enabled by the grating allows far richer behavior than a conventional FP.

6.2.3 Coupled Bloch Mode Model of GFP

A coupled-Bloch-mode model is utilized when studying the GFP structure, which is similar to the approach by Lalanne et al. studying deep lamellar gratings [188] which

is a huge simplification compared to RCWA.

The field inside the cavity is considered to be a superposition of two fields, one propagating in the positive z-direction and one in the negative z-direction. The field propagating in the positive z-direction inside the resonator is represented as $\boldsymbol{E}^{+}$, which is a 3×1 matrix representing the propagating modes only, i.e., -1, 0 and +1 diffracted orders. The propagation of the evanescent waves is completely neglected, since its intensity is far smaller than the propagating waves and its penetration depth is far smaller than the polymer thickness. Because energy conversion between different modes only happens at the grating, therefore the evanescent waves can be neglected. Similarly, the field propagating in the negative z-direction inside the resonator is represented as $\boldsymbol{E}^{-}$, which is also 3×1 matrix. A 3×3 diagonal matrix is defined as $\boldsymbol{\Phi}$ to represent the accumulated phase for each mode propagates from the interface of regions 1 and 2 to the interface of regions 2 and 3 as follow:

$$\boldsymbol{\Phi} = \begin{bmatrix} e^{ik_z h} & 0 & 0 \\ 0 & e^{i\frac{2\pi n_H}{\lambda}h} & 0 \\ 0 & 0 & e^{ik_z h} \end{bmatrix} \tag{6.7}$$

where $k_z = \sqrt{(2\pi n_H/\lambda)^2 - {k_g}^2}$, h is the thickness of the resonator and k_g is the grating vector.

Similarly, another 3×3 diagonal matrix $\boldsymbol{\Psi}$ is defined to account for the shift between the grating layers without time-consuming recalculation.

$$\boldsymbol{\Psi} = \begin{bmatrix} e^{-i\psi} & 0 & 0 \\ 0 & 1 & 0 \\ 0 & 0 & e^{i\psi} \end{bmatrix} \tag{6.8}$$

where ψ is the phase shift between the grating layers on each surface.

The developed model offers two significant benefits in comparison to directly calculating with RCWA. Firstly, the terms used in our model are more explicit, making it easier to analyze the underlying physical mechanisms. Secondly, once the canonical problem of scattering at the interface is solved, it can be easily solved for various structures with different thicknesses and relative phases between the upper and lower gratings, without having to restart the electromagnetic calculation from scratch.

Since only one mode exists in regions 1 and 3, reflectivity ref and transmissivity $trans$ are scalars and can be expressed as

$$ref = \boldsymbol{r}_{12} + \boldsymbol{t}_{21}\boldsymbol{\Phi}\boldsymbol{E}^{-} \tag{6.9}$$

$$trans = \boldsymbol{t}_{23}\boldsymbol{\Psi}\boldsymbol{\Phi}\boldsymbol{E}^{+} \tag{6.10}$$

where subscript indicates the direction of the term from region of the first digit to the region of the second digit.

And according to definition, the fields propagating in positive and negative z-direction can be expressed as

$$\boldsymbol{E}^{-} = \boldsymbol{\Psi}^{*}\boldsymbol{r}_{23}\boldsymbol{\Psi}\boldsymbol{\Phi}\boldsymbol{E}^{+} \tag{6.11}$$

$$\boldsymbol{E}^{+} = \boldsymbol{t}_{12} + \boldsymbol{r}_{21}\boldsymbol{\Phi}\boldsymbol{E}^{-} \tag{6.12}$$

Substituting Eq. (6.10) into Eq. (6.11) gives

$$\boldsymbol{E}^{+} = \boldsymbol{A}^{-1}\boldsymbol{t}_{12} \tag{6.13}$$

where $\boldsymbol{A} = \boldsymbol{I} - \boldsymbol{r}_{12}\boldsymbol{\Phi}\boldsymbol{\Psi}^{*}\boldsymbol{r}_{23}\boldsymbol{\Psi}\boldsymbol{\Phi}$.

Further substituting Eq. (6.12) into Eqs. (6.8) and (6.9) gives

$$ref = \boldsymbol{r}_{12} + \boldsymbol{t}_{21}\boldsymbol{\Phi}\boldsymbol{\Psi}^{*}\boldsymbol{r}_{23}\boldsymbol{\Psi}\boldsymbol{\Phi}\boldsymbol{A}^{-1}\boldsymbol{t}_{12} \tag{6.14}$$

$$trans = \boldsymbol{t}_{23}\boldsymbol{\Psi}\boldsymbol{\Phi}\boldsymbol{A}^{-1}\boldsymbol{t}_{12} \tag{6.15}$$

$\boldsymbol{r}$ and $\boldsymbol{t}$ can be calculated with RCWA for scattering from a single isolated grating. In this discussion, it is assumed that refractive index for region 1 and region 3, therefore, calculated values for subscript 12 and 32, 21 and 23 is the same. For the waves incident from the resonator medium, it is also necessary to consider the oblique incidence that represents the ± 1 diffracted orders as shown in Fig. 6.5.

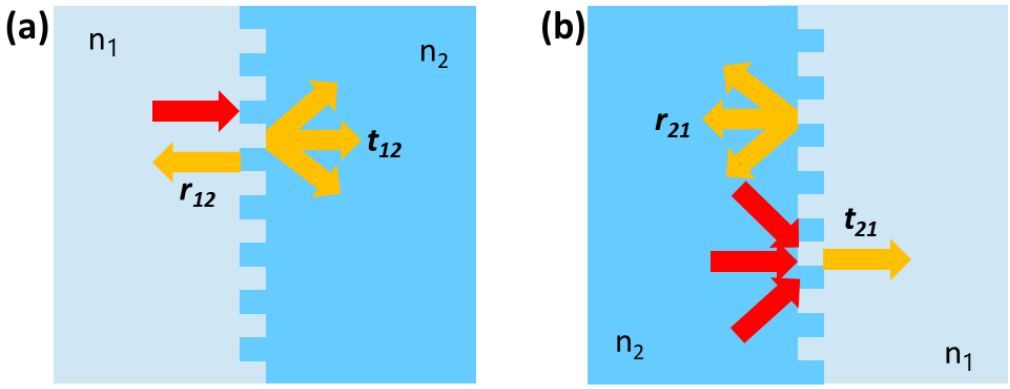

Fig. 6.5. Required RCWA calculation of coefficients of two semi-infinite media. (a) From substrate to structure, calculate $\boldsymbol{r}_{12}$ and $\boldsymbol{t}_{12}$ for the zero-th order of the incident beam, and (b) from structure to substrate, calculate $\boldsymbol{r}_{21}$ and $\boldsymbol{t}_{21}$ for the propagating zero-th order and ± 1 diffracted orders inside the structure.

The dimensions of the $\boldsymbol{r}$ and $\boldsymbol{t}$ terms are listed in Table 6.1. Assuming ψ in Eq. (6.7) equals 0 or π, which effectively means two grating layers have the same or opposite phase, the values for ± 1 diffracted orders are the same, therefore, the dimensions of matrix can be shrunk down to 2×2. But the utilization of the 3×3 formulation is more convenient when arbitrary displacement of the grating layers needs to be retained where the two diffracted orders typically exhibit a non-zero phase shift. The phase shift can be then represented with by a 2×2 matrix. Canonical solutions then can be solved for all thicknesses of grating.

Table 6.1 Dimensions of r and t Terms

Terms	Dimensions	Grating in phase
$\boldsymbol{r}_{12}$	scalar	scalar
$\boldsymbol{r}_{21}$	3×3	2×2
$\boldsymbol{r}_{23}$	3×3	2×2
$\boldsymbol{t}_{12}$	3×1	2×1
$\boldsymbol{t}_{21}$	1×3	1×2
$\boldsymbol{t}_{23}$	1×3	1×2

In another case with single grating layer at the bottom of the structure, ± 1 diffracted orders will experience total-internal-reflection at the interface of the polymer cavity and superstrate. Therefore, $\boldsymbol{r}_{23}$ becomes a 3×3 diagonal matrix with the first and last elements as unity; the first and the last elements of $\boldsymbol{t}_{23}$ become zero.

Similar arrangements can be defined for the case with single grating layer at the top of the structure.

It should be mentioned that the evanescent diffracted orders are not represented in the model, but they are considered in the calculation for $\boldsymbol{r}$ and $\boldsymbol{t}$ in RCWA in order to match the boundary conditions. This is the only role of the evanescent waves when the thickness is greater than the penetration depth.

Comparison with 81-order RCWA shows that within the wavelength well-defined by Eq. (6.6), the model can give complete agreement with RCWA for both the double grating layer structure and the single grating layer structure. Once the scattering with a single isolated grating layer is calculated, the matrix approach significantly reduces computing time by at least two orders of magnitude, enabling faster exploration of parameter domains.

6.3 Performance Analysis

6.3.1 Single Layer Grating FP Structure

The analysis starts with GFP with a single layer of grating at the bottom where the light illuminates. Fig. 6.6(a) shows a schematic diagram of the single layer GFP. The results are calculated for a structure with a single grating layer with grating period of 1.1 μm, resonator thickness of 10 μm, refractive index of resonator of 1.7 and surroundings 1.33.

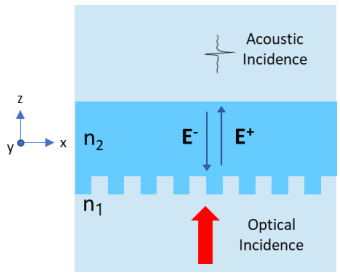

Fig. 6.6. Schematic diagram of the single-layer grating Fabry-Perot resonator.

Fig. 6.7(a) and Fig. 6.7(b) illustrate the reflectivity for TE polarization and TM polarization, respectively. Because there is only a single layer of grating, the behavior of the structure is a high-Q resonator with limited variation on the dynamic range of resonance. These figures are not valid for wavelengths less than 1.463 μm, since the $\pm 1^{st}$ diffracted order propagating inside the cavity at smaller wavelength, and above 1.87 μm since the second diffracted orders would be propagating inside the cavity at larger wavelength, because there will be more than one diffracted order propagating outside the resonator. At these wavelengths, the results from the coupled Bloch mode model do not agree with the RCWA.

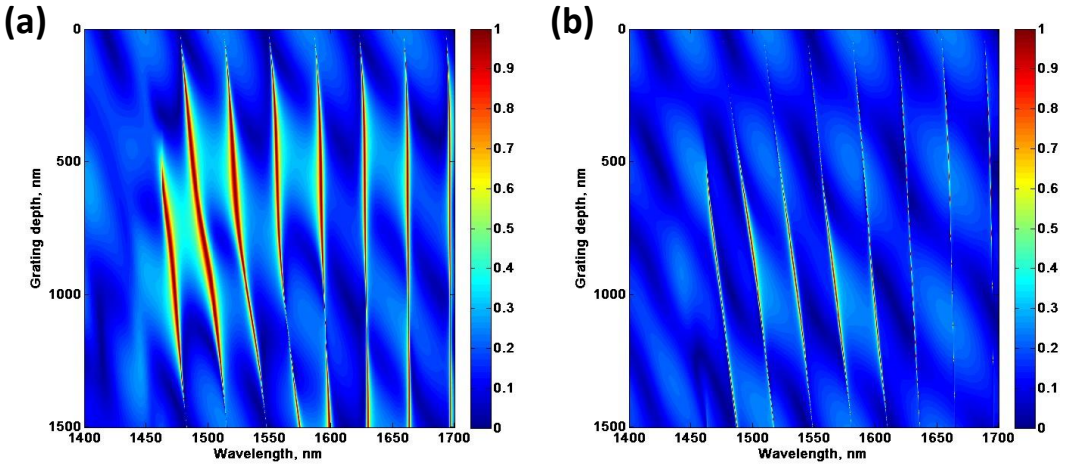

Fig. 6.7. Modulus of reflection coefficient for single-layer grating Fabry-Perot structure as a function of grating depth and incident wavelength for (a) TE polarization and (b) for TM polarization. The grating period was 1.1 μm and the resonator thickness was 10 μm.

Fig. 6.8 shows a wavelength scan with a 750 nm thick single grating layer and its response to 0.1 nm change in cavity thickness. The maximum response is 2.2 nm^{-1}, which is 55-fold improvement over conventional FP with 10 nm thick gold layer and 28-fold improvement over conventional FP with 15 nm thick gold layer.

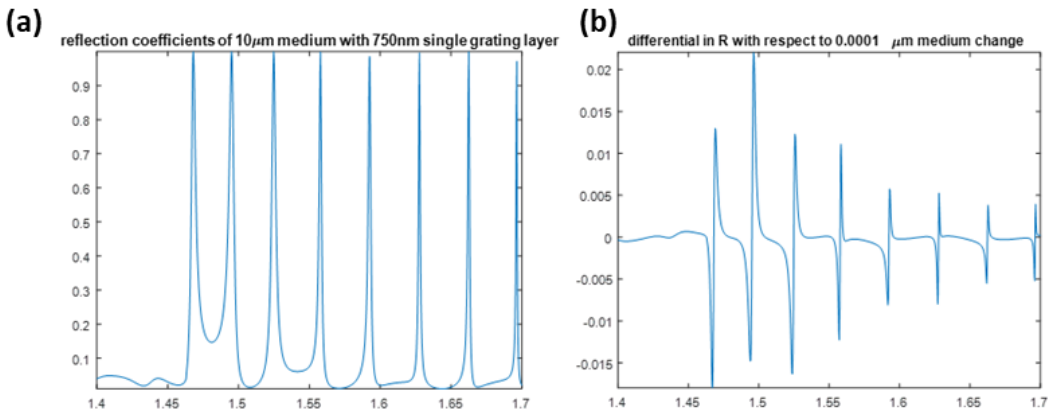

Fig. 6.8. (a) Modulus of the refraction coefficients for 750 nm single layer grating Fabry-Perot structure as a function of incident wavelength for TE polarization. (b) Response to 0.1 nm thickness displacement of the resonator thickness.

6.3.2 Double Layer Grating FP Structure

The double-layer GFP structure shows more varied behavior compared to single-layer GFP structure. Fig. 6.9 shows the modulus of reflection coefficient for double layer GFP structure with TE polarizations. It can be seen from Fig. 6.7 and Fig. 6.9 that TE polarization offers a richer behavior compared with TM polarizations, therefore, the discussion is more focused on TE polarization.

The mode hybridization is more obvious as marked with white arrows and white square because of the additional grating layer. Points marked with white arrows indicate mode hybridization between GFP mode and faint conventional FP modes in the background, forming a high-Q resonance, which can be potentially used for

sensing applications. The white squared area marks the interaction between different GFP modes, forming a broadband reflector.

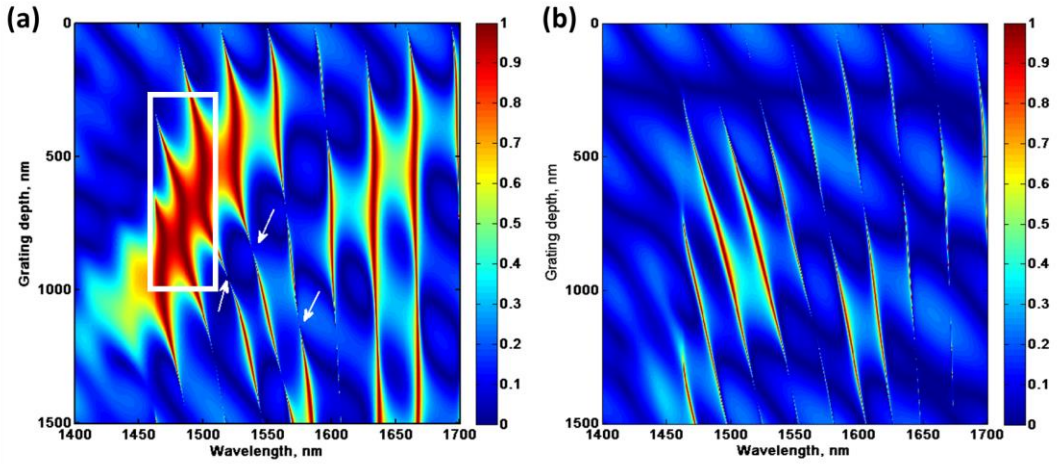

Fig. 6.9. Modulus of reflection coefficient for double-layer grating Fabry-Perot structure as a function of grating depth and incident wavelength for (a) TE polarization and (b) TM polarization. The grating period is 1.1 μm and resonator thickness is 10 μm.

Fig. 6.10 shows the reflectivity for double-layer GFP with 50 μm polymer cavity. It can be seen that the behavior is even richer compared to the 10-μm-thick case. The thickness offers the potential for greater acoustic sensitivity and allows for direct comparison with the conventional FP discussed earlier.

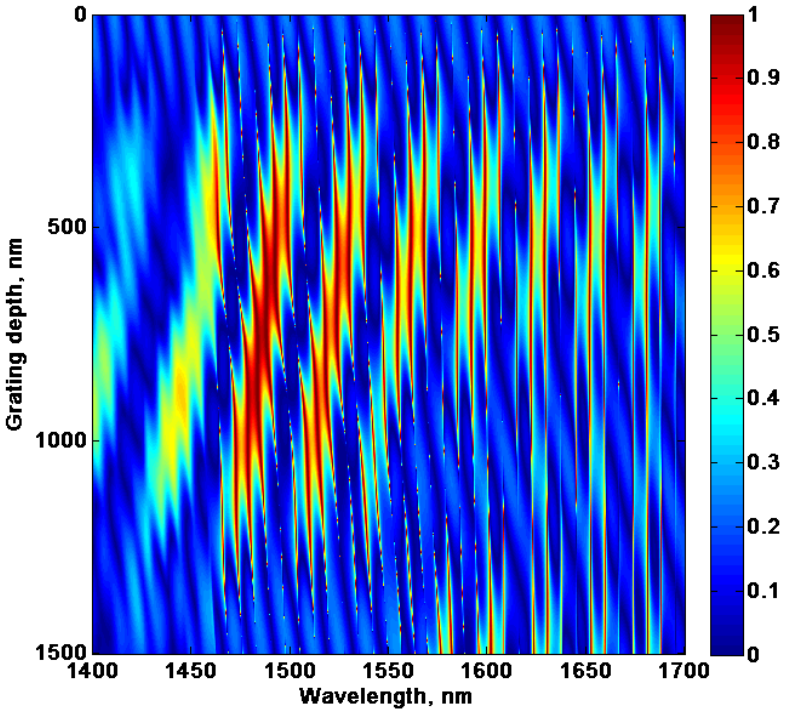

Fig. 6.10. Modulus of reflection coefficient for double-layer grating Fabry-Perot structure as a function of grating depth and incident wavelength for TE polarization. The grating period is 1.1 μm and resonator thickness is 50 μm.

For a direct comparison with the conventional FP, selected peaks obtained at 840 nm grating depth for TE polarization are analyzed as marked in Fig. 6.11 with ‘a’ - ‘e’. Fig. 11 shows the reflectivity of double-layer GFP with 840 nm grating depth and TE polarization. Response calculated with 0.1 nm displacement in thickness for peak ‘a’-‘c’ are plotted in Fig. 6.12(a)-12(c), respectively.

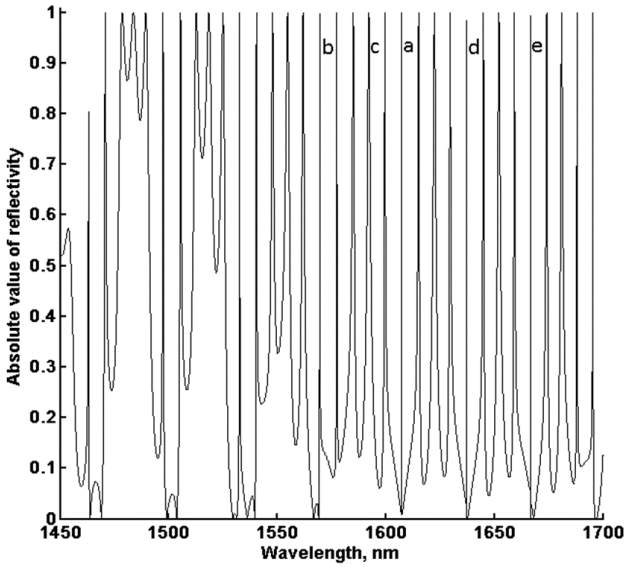

Fig. 6.11. Modulus of reflection coefficient for double-layer grating Fabry-Perot structure with 840 nm grating depth and TE polarization. Peaks referred to in the text are marked ‘a’, ‘b’, ‘c’, ‘d’ and ‘e’.

Fig. 6.12(a) is calculated for one of peaks with very high Q, which is centered at 1607.3 nm. Because of its sharpness, the responsivity is plotted against the relative deviation from the center wavelength. The peak response is around 0.72, therefore, the responsivity is about 7.2 nm^{-1}, a 180-fold improvement over the conventional FP with 10 nm gold layer and approximately 90-fold improvement over the conventional FP with 15 nm gold layer. Naturally, the intrinsic dynamic range of this peak is much less than that of the conventional FP. The peak ‘b’ has sensitivity about a factor of two better than the conventional FP with 15 nm gold layer and the peak ‘c’ has sensitivity about a fifth of that for the conventional FP. Therefore, since we have a peak with 5

times less sensitivity compared to a conventional FP and one with 18 times improvement, we have a powerful 900-fold improvement in dynamic range. Therefore, a total of 900-fold improvement for double-layer GFP in intrinsic dynamic range can be estimated over the conventional FP with 10 nm gold layer. Intrinsic dynamic range is an important feature for applications, e.g., photoacoustic sensing, where generated signals of different objects can vary by order of magnitude. Otherwise, the detector can suffer from signal saturation or signal quantization error. Having a detector with resonances of different responsivity can also ensure that the signal-to-noise ratios for signals of different scales remain on similar levels.

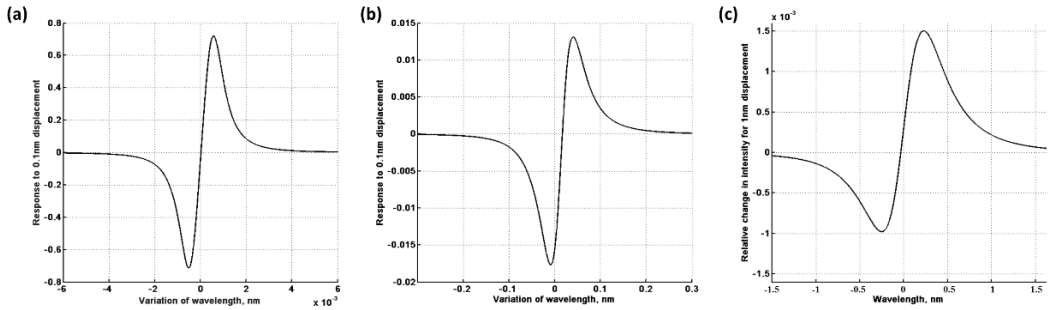

Fig. 6.12. Responsivity to 0.1 nm displacement for different peaks. (a) Response around peak ‘a’ at approximately 1607.3 nm. (b) Response around peak ‘b’ at approximately 1569.5 nm. (c) Response around peak ‘c’ at approximately 1585 nm.

The improvement in dynamic range can be beneficial in situations where signals of different orders of magnitude exist in the same experiment. For a practical material,

e.g., PMMA, with a thickness of 50 μm, a sensitivity of 7.2 nm^{-1} can be well-saturated with a pressure of 22 kPa. For signals of higher amplitudes, a resonance with lower sensitivity can be used. Moreover, in terms of the additive Gaussian noise from the detectors, conventional sensors suffer more from noise in the case of small signals compared to large signals. Using sensors with various resonances and different Q values can ensure that signals of order-of-magnitude different amplitudes have a similar level of signal-to-noise ratio (SNR). Therefore, the compatibility of the sensor can be greatly improved to accommodate different samples.

6.4 Proposed Fabrication Process

In the simulation of GFP structures, it is assumed that superstrate and substrate have the same refractive index as water. Low refractive index of the substrate is required to satisfy the inequality Eq. (6.6) so that there is only one propagating wave in the substrate and the first orders propagating inside the polymer are partially diffracted by the grating and totally internally reflected at the interface of the substrate and the structure.

It may seem counter-intuitive that the structure is suspended in water. In reality, there are multiple options for the choice of the substrate with suitable refractive index below 1.4. The refractive index below 1.4 combined with a grating period of 1 μm or 1.1 μm gives a low cut-off wavelength 1.4 μm to 1.54 μm, which would still allow a broad operating wavelength range for a commercially available tunable laser centered

at 1550 nm [189].

6.4.1 Fabrication Process for Single-Layer GFP

The plan is to fabricate the structure on top of transparent coverslips. The substrate material with low refractive index plays a significant role in GFP to totally internally reflect the first diffracted orders coming from the polymer. The case is somewhat similar to the HARG-FP structure.

It is worth noting that when the first diffracted order is reflected, an evanescent field is established at the interface and dissipates in the substrate. Therefore, the thickness of the substrate layer is a key factor, and it has to be considerably larger than the penetration depth of the evanescent wave so that the evanescent wave cannot reach the backing material, e.g., glass, and becomes a propagating wave again. For interrogation wavelengths around 1550 nm, a minimum thickness of 2 μm is suggested for the substrate layer so that there is enough separation between the polymer cavity and the backing material.

For the choice of the substrate layer, both polymer and photonic crystal can be considered. For polymer, a fluoropolymer named Cytop (AGC Chemicals, Japan) is considered for its low refractive index of 1.33 at 1550 nm. The polymer can be spin-coated. At a spin speed of 1000 rpm, the film thickness is about 3.5 μm for CTX-809A and 2 μm for CTX-809L. However, if polymer is used as substrate, the bottom layer grating is difficult to fabricate on top of the substrate.

For photonic crystals, wide selection of fluoride crystals is available with low refractive index, i.e., MgF_2, LiF and NaF [190, 191]. The material can be sputtered with an RF gun or deposited with an electron-beam evaporator.

Of the two choices, photonic crystal is more feasible for bottom grating layer, since with a combination of E-Beam Lithography (EBL) and lift-off process, Enhanced control over grating profiles can be achieved.

For GFP structures with a single grating layer, the grating layer can be on either side of the polymer cavity, in contact with the substrate or water, respectively. For both cases, the performance does not differ much. But the grating layer at the bottom can allow more options for cavity materials since there is no need for the cavity to uphold another layer on top. Soft materials such as PDMS with excellent optical and mechanical properties can be used.

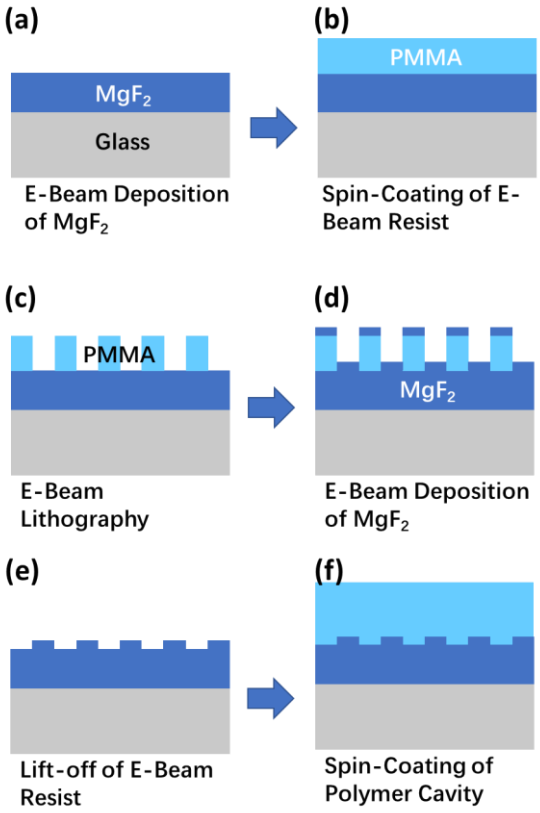

Fig. 6.13. a diagram for single-layer GFP fabrication. (a) E-beam deposition of MgF_2, (b) spin coating E-beam Resist, (c) positive EBL process, (d) E-beam deposition of MgF_2 grating, (e) lift-off process to remove the positive PMMA resist and (f) spin-coating of the polymer FP cavity.

Fig. 6.13 shows a brief diagram for single-layer GFP fabrication with six steps. with deposition of 2-μm-thick MgF_2 can be prone to cracking due to the surface tension caused by the high fabrication temperature. Therefore, a 50-nm-thick Al_2O_3 should be deposited for every 500-nm-thick MgF_2. The process uses a combination of EBL and lift-off for grating fabrication with MgF_2 as the grating material. After the

spin-coating, the single-layer GFP can be fabricated.

6.4.2 Fabrication Process for double-Layer GFP

An extra grating layer is required for double-layer GFP. Conventionally, an extra EBL process is required for PET or Parylene cavity. This process requires an additional thin conductive layer before spin-coating the E-beam resist for electron to dissipate, otherwise, there will be cracks on the surface.

For a FP cavity made of PDMS, thermal or UV nano-imprinting process can be applied [192, 193]. A mold with the desired grating pattern is made with deep ultra-violet lithography. After spin-coating of PDMS, the mold is attached to a membrane and applied onto the wet PDMS layer while the chamber between the membrane and trunk is deaerated to remove any air bubbles and the membrane is inflated with air to apply extra pressure on the mold. Depending on the types of PDMS, heat or UV light is applied to cure the PDMS layer. After the curing process, the mold is lifted off PDMS and the grating is printed.

With nano-imprinting technique, the time for fabrication of one grating layer can be shortened to under 10 minutes with going through the tedious and time-consuming writing process of EBL.

6.5 Summary

In this chapter, the concept of GFP is introduced and thoroughly investigated

theoretically. The relationship between grating period and incident wavelength is discussed for GFP modes. A simplified coupled-Bloch-mode model is presented, which shows excellent agreement with a rigorous analysis method, i.e., RCWA. The simulation for GFP modes is presented. It is shown that GFP structures can exhibit enriched behavior including resonance with highly varying Q and broadband pass filter. Then, we focused on the resonance and showed that the Q for different resonance with the same grating structure can vary from 3,000 to over 1,000,000, which can potentially provide over 900-fold improvement in intrinsic dynamic range compared to the conventional Fabry-Pérot structure. The peak response of the sharpest resonance can provide an approximately 180-fold improvement over the conventional FP with 10 nm gold layer. A discussion on fabrication of both single-layer GFP and double-layer GFP is also included. Overall, with extensive behavior enabled by double-layer grating, GFP possess significant potential for ultrasound and photoacoustic imaging, with easy integration with other optical modalities, e.g., optical coherent tomography, because of its transparent nature at visible wavelengths and above GFP wavelengths.

Chapter 7 Conclusion and Prospects

In this chapter, conclusions will be drawn, and future research work will be discussed.

7.1 Conclusion

In this thesis, three types of high performance Fabry-Pérot structures have been demonstrated for refractive index sensing, ultrasound detection and photoacoustic sensing, i.e., high-aspect-ratio-grating-based Fabry-Pérot (HARG-FP) structure for high figure-of-merit refractive index sensing, total-internal-reflection-based Fabry-Pérot (TIR-FP) structure for ultra-sensitive and wideband ultrasound and photoacoustic sensing, and the grating based Fabry-Pérot (GFP) resonator as a highly sensitive ultrasound/photoacoustic sensor. Detailed conclusions are drawn for each type of novel FP structures.

7.1.1 High-aspect-ratio-grating-based Fabry-Pérot structure

In Chapter 3, a HARG-FP structure has been presented and investigated with both theoretical analysis and experiment with TM and TE polarization for high-FOM refractive index measurement at 633 nm optical wavelength. In theoretical analysis, a transmission line model and Smith charts was used to present more intuition into the physics behind the resonator and also provide a layer-wise analysis.

Experimentally, a direct comparison between the conventional surface plasmon

resonator with a 48-nm gold layer, HARG-FP structure with TM and TE polarization for refractive index sensing within the same system. Grating structures with two different duty cycles were tested with TM polarization for comparison of performance. With a duty cycle of 23% for TM polarization, an FOM of 331 was recorded, which is a 10-fold improvement over conventional SPR, whereas with a duty cycle of 35% for TE polarization, an FOM of 1394 was recorded, which is a 44-fold improvement over conventional SPR samples tested within the system. In this discussion, sensitivity, defined with the noise-equivalent refractive index unit, was 1.87×10^{-8} RIU without frame averaging for TE polarization. Averaging 794 frames (approximately 1-second acquisition time) can improve the sensitivity to 1.61×10^{-9} RIU.

With the abovementioned analysis, it is demonstrated that HARG-FP has the capacity to perform high-FOM sensing with outstanding sensitivity performance. The interrogation system is identical to the ones used for conventional SPR, and the excitation angles of the HARG-FP modes are similar to that of the SPR. Moreover, mass production can be done with nano-imprinting techniques at extremely low cost. Therefore, HARG-FP can be a ready substitute in the related sensing applications where SPR is widely used at present.

7.1.2 Total-internal-reflection-based Fabry-Pérot structure

TIR-FP structure was proposed and investigated for ultra-sensitive and wideband ultrasound and photoacoustic sensing applications at 1550 nm optical wavelength.

Chapter 3 presents the mechanical and optical analysis of TIR-FP with the transfer matrix method and Fresnel equations. Chapter 4 presents the experiment results and analysis of TIR-FP. The sensitivity of the TIR-FP comes from two aspects. The first is the deformation of the cavity and the other is pressured induced refractive index change, which results in a phase shift at the top interface. The former contributes high sensitivity within a relatively narrow bandwidth depending on the thickness of the cavity, whereas the latter, since its evanescent field decays quickly off the interface, has a considerable bandwidth.

Two sets of samples were tested with PDMS and PMMA as the cavity. PMMA- and PDMS-based TIR-FP exhibited responsivities of 5.45×10^{-8} Pa^{-1} and 4.5×10^{-7} Pa^{-1} with 110 MHz and 75 MHz bandwidths with a 150 MHz photodetector, respectively, indicating a 3.6- and 30-fold improvement over the conventional system measured in the same system. Sensitivity for PDMS-based TIR-FP was measured to be 160 Pa with the UT excited with small signals generated from a function generator. Further improvement can be achieved with slightly more complicated optical system design for phase interrogation and common-path noise elimination.

7.1.3 Grating Fabry-Pérot structure

A GFP structure was introduced for pressure sensing applications in Chapter 6. The rich behavior of the GFP arises from the grating layer where the optical beam is diffracted, and energy transfer happens between different diffracted orders. With two

grating layers on each side of the polymer, the GFP can function as a high-Q and a wideband reflector.

In the analysis, it was shown that within a double-layer GFP with 50 μm polymer cavity, resonances with Q varying from 3,000 to over 1,000,000 can be observed, providing extraordinary sensitivity and intrinsic dynamic range of detection. In a lateral comparison with the conventional FP structures with 50 μm, sharp peaks can provide a responsivity of 7.2 nm^{-1}, a 180-fold improvement over the conventional FP with 10 nm gold layer and approximately 90-fold improvement over the conventional FP with 15 nm gold layer. In terms of intrinsic dynamic range, the double-layer GFP with 50 μm can easily provide 900-fold improvement compared to the conventional FP structures within the same structure. This will benefit situations where signals of huge scale differences are present, e.g., photoacoustic sensing. Low-Q resonance can be used to detect large signals to avoid saturation, whereas high-Q resonance can be used to detect small signals to avoid quantization errors of data acquisition electronics, simultaneously. Moreover, resonances with sensitivity of different scales can give similar signal-to-noise ratio for signals of different scales in terms of laser fluctuations and additive noise. This can be done by aligning two tunable investigation lasers onto the same sample region, alternatively, by using a broadband light source with a couple of filters.

7.2 Prospects

This thesis proposed and analyzed three types of novel FP structures for sensing applications, and some recommendations for future work are given as follows:

(1) HARG-FP worked effectively for sensing refractive index changes with a camera and a collimated beam projected onto the samples. In the latter stage, modest modifications, e.g., an additional SLM, can be done to the system so that the beam projected on the sample can be focused on multiple points to extract multi-channel refractive index fluctuations for high-throughput sensing applications. This can greatly increase the throughput of the system. Another reference beam can be introduced to suppress laser fluctuations and common-path noise.

(2) TIR-FP exhibited ultra-sensitive and wideband performance for ultrasound and photoacoustic sensing applications. Currently, the excitation beam of photoacoustic signals are 532-nm nanosecond laser pulses focused with a conventional achromatic lens with 50 mm focal length at visible wavelength, the NA of which is 0.24. If the beam is focused with an objective lens with adequate NA of 0.4 or higher instead, the system can be effectively applied for optical-resolution photoacoustic microscopy (OR-PAM) with a lateral resolution around 1 μm.

(3) GFP exhibited huge potential for ultra-sensitive performance with large intrinsic dynamic range for acoustic sensing. GFP sensors can be fabricated based on the

proposed fabrication process and tested with the proposed backward-mode OR-PAM system in Fig. 7.1.

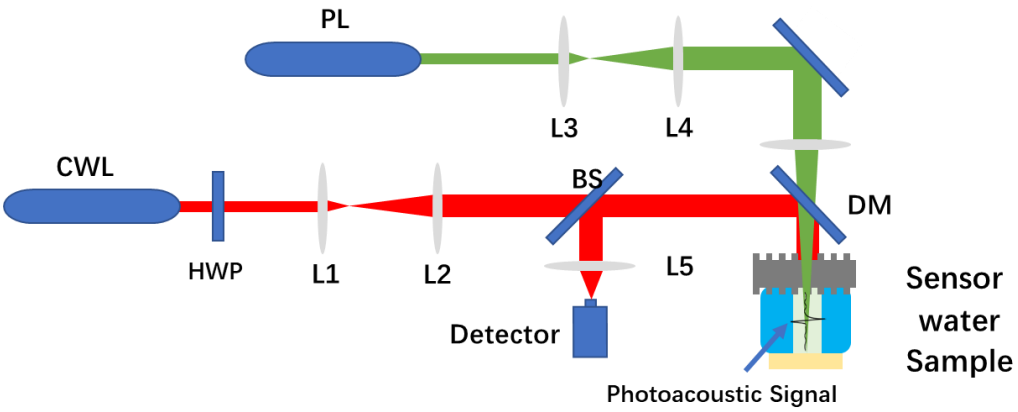

Fig. 7.1. Schematic diagram of proposed backward-mode OR-PAM system for GFP. PL: pulse laser; CWL: continuous-wave laser; BS: beamsplitter; DM: dichroic mirror.

(4) GFP can be considered as a bimodal resonator, the fundamental idea of which is having one propagating mode outside and two propagating modes inside the structure. An analogy of GFP can be made in fiber form consisting of a single-mode fibers and double-mode fibers. A double-mode fiber is fusion-spliced between two single-mode fibers. Acoustic sensing can be achieved with the double-mode fiber. Potential for sensing with compact design and portability can be expected.

Bibliography

[1] C. He, H. He, J. Chang, B. Chen, H. Ma, and M. J. Booth, "Polarisation optics for biomedical and clinical applications: a review," *LIGHT-SCIENCE & APPLICATIONS*, Review vol. 10, no. 1, 2021 SEP 22 2021, Art no. 194.

[2] C. Glorieux, "Perspective on non-invasive and non-destructive photoacoustic and photothermal applications," *JOURNAL OF APPLIED PHYSICS*, Article vol. 131, no. 17, 2022 MAY 7 2022, Art no. 170903.

[3] Y. Meng, Y. Chen, L. Lu, Y. Ding, A. Cusano, J. A. Fan, Q. Hu, K. Wang, Z. Xie, Z. Liu, Y. Yang, Q. Liu, M. Gong, Q. Xiao, S. Sun, M. Zhang, X. Yuan, and X. Ni, "Optical meta-waveguides for integrated photonics and beyond," *LIGHT-SCIENCE & APPLICATIONS*, Review vol. 10, no. 1, 2021 NOV 22 2021, Art no. 235.

[4] L. Chang, S. Liu, and J. E. Bowers, "Integrated optical frequency comb technologies," *NATURE PHOTONICS*, Review vol. 16, no. 2, pp. 95-108, 2022 FEB 2022.

[5] G. Wissmeyer, M. A. Pleitez, A. Rosenthal, and V. Ntziachristos, "Looking at sound: optoacoustics with all-optical ultrasound detection," *LIGHT-SCIENCE & APPLICATIONS*, Review vol. 7, 2018 AUG 15 2018, Art no. 53.

[6] H. Altug, S.-H. Oh, S. A. Maier, and J. Homola, "Advances and applications of nanophotonic biosensors," *Nature Nanotechnology*, vol. 17, no. 1, pp. 5-16, 2022/01/01 2022.

[7] J. A. Guggenheim, J. Li, T. J. Allen, R. J. Colchester, S. Noimark, O. Ogunlade, I. P. Parkin, I. Papakonstantinou, A. E. Desjardins, E. Z. Zhang, and P. C. Beard, "Ultrasensitive plano-concave optical microresonators for ultrasound sensing," *NATURE PHOTONICS*, Article vol. 11, no. 11, pp. 714-+, 2017

NOV 2017.

[8] S. Yoon, M. Kim, M. Jang, Y. Choi, W. Choi, S. Kang, and W. Choi, "Deep optical imaging within complex scattering media," *NATURE REVIEWS PHYSICS*, Review vol. 2, no. 3, pp. 141-158, 2020 MAR 2020.

[9] J. Wang, R. J. Smith, R. A. Light, J. L. Richens, J. Zhang, P. O'Shea, C. See, and M. G. Somekh, "Highly sensitive multipoint real-time kinetic detection of Surface Plasmon bioanalytes with custom CMOS cameras," (in English), *Biosens Bioelectron,* vol. 58, pp. 157-164, Aug 15 2014.

[10] W. Song, F. Yang, C. Min, S. Zhu, and X. Yuan, "Toward Ultrasensitive, Broadband, Reflection-Mode In Vivo Photoacoustic Microscopy Using a Bare Glass," *Laser & Photonics Reviews,* vol. 17, no. 1, p. 2200030, 2023.

[11] P. Marek, H. Kateřiná, V. Milan, C. Karel, T. Ivo, and H. Jiří, "Compact multi-channel high-sensitivity biosensor based on spectroscopy of surface plasmons," in *Proc.SPIE*, 2009, vol. 7192, doi: 10.1117/12.809216. [Online]. Available: https://doi.org/10.1117/12.809216

[12] M. A. Kats and F. Capasso, "Optical absorbers based on strong interference in ultra-thin films," *LASER & PHOTONICS REVIEWS*, Review vol. 10, no. 5, pp. 735-749, 2016 SEP 2016.

[13] K. Pham, S. Noimark, N. Huynh, E. Zhang, F. Kuklis, J. Jaros, A. Desjardins, B. Cox, and P. Beard, "Broadband All-Optical Plane-Wave Ultrasound Imaging System Based on a Fabry-Perot Scanner," *Ieee T Ultrason Ferr,* Article vol. 68, no. 4, pp. 1007-1016, 2021 APR 2021.

[14] C. Massaroni, M. Zaltieri, D. Lo Presti, A. Nicolo, D. Tosi, and E. Schena, "Fiber Bragg Grating Sensors for Cardiorespiratory Monitoring: A Review," *Ieee Sens J,* vol. 21, no. 13, pp. 14069-14080, Jul 1 2021.

[15] J.-F. Masson, "Surface Plasmon Resonance Clinical Biosensors for Medical Diagnostics," *Acs Sensors,* vol. 2, no. 1, pp. 16-30, Jan 2017.

[16] M. Nirschl, F. Reuter, and J. Voros, "Review of transducer principles for label-free biomolecular interaction analysis," *Biosensors*, vol. 1, no. 3, pp. 70-92, 2011 Jul 2011.

[17] J. Zhou, Q. Qi, C. Wang, Y. Qian, G. Liu, Y. Wang, and L. Fu, "Surface plasmon resonance (SPR) biosensors for food allergen detection in food matrices," *Biosens Bioelectron*, vol. 142, Oct 1 2019, Art no. 111449.

[18] D. Kinet, P. Megret, K. W. Goossen, L. Qiu, D. Heider, and C. Caucheteur, "Fiber Bragg Grating Sensors toward Structural Health Monitoring in Composite Materials: Challenges and Solutions," *Sensors-Basel*, vol. 14, no. 4, pp. 7394-7419, Apr 2014.

[19] Y. Xu, P. Bai, X. Zhou, Y. Akimov, C. E. Png, L. K. Ang, W. Knoll, and L. Wu, "Optical Refractive Index Sensors with Plasmonic and Photonic Structures: Promising and Inconvenient Truth," *Adv Opt Mater*, vol. 7, no. 9, 2019.

[20] R. M. A. Azzam and N. M. Bashara, *Ellipsometry and Polarized Light*. North-Holland Publishing Company, 1977.

[21] J. Wang, R. J. Smith, R. A. Light, J. L. Richens, J. Zhang, P. O'Shea, C. See, and M. G. Somekh, "Highly sensitive multipoint real-time kinetic detection of Surface Plasmon bioanalytes with custom CMOS cameras," *Biosens Bioelectron*, vol. 58, pp. 157-64, Aug 15 2014.

[22] T. Velinov, M. Bivolarska, S. Russev, K. Bransalov, and M. Somekh, "Polarization control scheme for surface plasmon and optical guided mode control detection," (in English), *Sensor Actuat B-Chem*, vol. 100, no. 3, pp. 325-332, May 15 2004.

[23] K. J. Moh, X. C. Yuan, J. Bu, R. E. Burge, and B. Z. Gao, "Generating radial or azimuthal polarization by axial sampling of circularly polarized vortex beams," (in English), *Appl Optics*, vol. 46, no. 30, pp. 7544-7551, Oct 20 2007.

[24] B. Zhang, C. Q. Zhang, M. G. Somekh, P. Yan, and L. Wang, "Common-path

surface plasmon interferometer with radial polarization," (in English), *Opt Lett*, vol. 43, no. 14, pp. 3245-3248, Jul 15 2018.

[25] T. Lei, M. Zhang, Y. Li, P. Jia, G. N. Liu, X. Xu, Z. Li, C. Min, J. Lin, C. Yu, H. Niu, and X. Yuan, "Massive individual orbital angular momentum channels for multiplexing enabled by Dammann gratings," *LIGHT-SCIENCE & APPLICATIONS*, Article vol. 4, 2015 MAR 2015, Art no. e257.

[26] P. Yeh, *Optical Waves in Layered Media*. Wiley, 2004.

[27] M. G. Moharam, E. B. Grann, D. A. Pommet, and T. K. Gaylord, "Formulation for stable and efficient implementation of the rigorous coupled-wave analysis of binary gratings," *J. Opt. Soc. Am. A*, vol. 12, no. 5, pp. 1068-1076, 1995/05/01 1995.

[28] E. Popov and M. Nevière, "Maxwell equations in Fourier space: fast-converging formulation for diffraction by arbitrary shaped, periodic, anisotropic media," *J. Opt. Soc. Am. A*, vol. 18, no. 11, pp. 2886-2894, 2001/11/01 2001.

[29] M. G. Moharam and T. K. Gaylord, "Rigorous coupled-wave analysis of planar-grating diffraction," *Journal of the Optical Society of America*, vol. 71, no. 7, pp. 811-818, 1981/07/01 1981.

[30] R. Nuster and G. Paltauf, "Sensitivity of surface plasmon resonance sensors for the measurement of acoustic transients in liquids," in *IEEE Ultrasonics Symposium*, Vancouver, CANADA, 2006

Oct 03-06 2006, in Ultrasonics Symposium, 2006, pp. 768-771, doi: 10.1109/ultsym.2006.166. [Online]. Available: <Go to ISI>://WOS:000260407800184

[31] R. Nuster, G. Paltauf, and P. Burgholzer, "Comparison of surface plasmon resonance devices for acoustic wave detection in liquid," *Opt Express*, vol. 15, no. 10, pp. 6087-6095, 2007/05/14 2007.

[32] R. Zakaria, N. A. Zainuddin, S. A. Raya, S. A. Alwi, T. Anwar, A. Sarlan, K. Ahmed, and I. S. Amiri, "Sensitivity Comparison of Refractive Index Transducer Optical Fiber Based on Surface Plasmon Resonance Using Ag, Cu, and Bimetallic Ag–Cu Layer," *Micromachines-Basel,* vol. 11, no. 1, 2020.

[33] S. H. Chew, A. Gliserin, S. Choi, X. T. Geng, S. Kim, W. Hwang, K. Baek, N. D. Anh, Y.-J. Kim, Y. M. Song, D. E. Kim, S.-Y. Jeong, and S. Kim, "Large-area grain-boundary-free copper films for plasmonics," *Appl Surf Sci,* vol. 521, p. 146377, 2020/08/15/ 2020.

[34] Kretschm.E and H. Raether, "RADIATIVE DECAY OF NON RADIATIVE SURFACE PLASMONS EXCITED BY LIGHT," *Zeitschrift Fur Naturforschung Part a-Astrophysik Physik Und Physikalische Chemie,* vol. A 23, no. 12, pp. 2135-&, 1968 1968.

[35] A. Otto, "Excitation of nonradiative surface plasma waves in silver by the method of frustrated total reflection," *Zeitschrift für Physik A Hadrons and nuclei,* vol. 216, no. 4, pp. 398-410, 1968/08/01 1968.

[36] Y. Lee, S.-m. Sim, J.-M. Kim, and Ieee, "Otto configuration based surface plasmon resonance with tunable air-gap using piezoactuator," in *International Conference on Optical MEMS and Nanophotonics (OMN)*, KAIST, Daejeon, SOUTH KOREA, 2019

Jul 28-Aug 01 2019, in International Conference on Optical MEMS and Nanophotonics, 2019, pp. 60-65. [Online]. Available: <Go to ISI>://WOS:000522410000027. [Online]. Available: <Go to ISI>://WOS:000522410000027

[37] M. Q. Shen, S. Learkthanakhachon, S. Pechprasarn, Y. P. Zhang, and M. G. Somekh, "Adjustable microscopic measurement of nanogap waveguide and plasmonic structures," *Appl Optics,* vol. 57, no. 13, pp. 3453-3462, May 2018.

[38] E. Popov, N. Bonod, and S. Enoch, "Comparison of plasmon surface waves on

shallow and deep metallic 1D and 2D gratings," *Opt Express,* vol. 15, no. 7, pp. 4224-4237, 2007/04/02 2007.

[39] J. Homola, I. Koudela, and S. S. Yee, "Surface plasmon resonance sensors based on diffraction gratings and prism couplers: sensitivity comparison," *Sensor Actuat B-Chem,* vol. 54, no. 1-2, pp. 16-24, Jan 25 1999.

[40] P. Zhang, L. Liu, Y. He, Z. Shen, J. Guo, Y. Ji, and H. Ma, "Non-scan and real-time multichannel angular surface plasmon resonance imaging method," *Appl Optics,* vol. 53, no. 26, pp. 6037-6042, 2014/09/10 2014.

[41] M. Shen, Q. Zou, X. Jiang, F. Feng, and M. G. Somekh, "Single-shot three-input phase retrieval for quantitative back focal plane measurement," *Photonics Res,* vol. 10, no. 2, pp. 491-502, 2022/02/01 2022.

[42] J. Homola, S. S. Yee, and G. Gauglitz, "Surface plasmon resonance sensors: review," *Sensor Actuat B-Chem,* vol. 54, no. 1-2, pp. 3-15, Jan 25 1999.

[43] D. Wang, F. C. Loo, H. Cong, W. Lin, S. K. Kong, Y. Yam, S. C. Chen, and H. P. Ho, "Real-time multi-channel SPR sensing based on DMD-enabled angular interrogation," *Opt Express,* vol. 26, no. 19, pp. 24627-24636, Sep 17 2018.

[44] Y. Xu, P. Bai, X. D. Zhou, Y. Akimov, C. E. Png, L. K. Ang, W. Knoll, and L. Wu, "Optical Refractive Index Sensors with Plasmonic and Photonic Structures: Promising and Inconvenient Truth," (in English), *Adv Opt Mater,* vol. 7, no. 9, May 2019.

[45] M. Piliarik, M. Vala, I. Tichy, and J. Homola, "Compact and low-cost biosensor based on novel approach to spectroscopy of surface plasmons," (in English), *Biosens Bioelectron,* vol. 24, no. 12, pp. 3430-3435, Aug 15 2009.

[46] X. Chong, L. Liu, Z. Liu, S. Ma, J. Guo, Y. Ji, and Y. He, "Detect the Hybridization of Single-Stranded DNA by Parallel Scan Spectral Surface Plasmon Resonance Imaging," *Plasmonics,* Article vol. 8, no. 2, pp. 1185-1191, 2013 JUN 2013.

[47] L. Liu, Y. He, Y. Zhang, S. Ma, H. Ma, and J. Guo, "Parallel scan spectral surface plasmon resonance imaging," *Appl Optics,* Article vol. 47, no. 30, pp. 5616-5621, 2008 OCT 20 2008.

[48] M. Lu, Y. Liang, S. Qian, L. Li, Z. Jing, J.-F. Masson, and W. Peng, "Optimization of Surface Plasmon Resonance Biosensor with Ag/Au Multilayer Structure and Fiber-Optic Miniaturization," *Plasmonics,* vol. 12, no. 3, pp. 663-673, 2016.

[49] S. Deng, P. Wang, and X. Yu, "Phase-Sensitive Surface Plasmon Resonance Sensors: Recent Progress and Future Prospects," *Sensors (Basel),* vol. 17, no. 12, Dec 5 2017.

[50] Y. H. Huang, H. P. Ho, S. K. Kong, and A. V. Kabashin, "Phase-sensitive surface plasmon resonance biosensors: methodology, instrumentation and applications," *Ann Phys-Berlin,* vol. 524, no. 11, pp. 637-662, Nov 2012.

[51] A. V. Kabashin and P. I. Nikitin, "Interferometer based on a surface-plasmon resonance for sensor applications," *Quantum Electronics,* vol. 27, no. 7, pp. 653-654, 1997.

[52] Y. Shao, Y. Li, D. Gu, K. Zhang, J. Qu, J. He, X. Li, S.-Y. Wu, H.-P. Ho, M. G. Somekh, and H. Niu, "- Wavelength-multiplexing phase-sensitive surface plasmon imaging sensor," vol. - 38, no. - 9, pp. - 1372, 2013.

[53] S. P. Ng, C. M. L. Wu, S. Y. Wu, and H. P. Ho, "White-light spectral interferometry for surface plasmon resonance sensing applications," *Opt Express,* Article vol. 19, no. 5, pp. 4521-4527, 2011 FEB 28 2011.

[54] S.-P. Ng, C.-M. L. Wu, S.-Y. Wu, H.-P. Ho, and S. K. Kong, "Differential spectral phase interferometry for wide dynamic range surface plasmon resonance biosensing," *Biosens Bioelectron,* vol. 26, no. 4, pp. 1593-1598, 2010 DEC 15 2010.

[55] S.-P. Ng, C.-M. L. Wu, S.-Y. Wu, H.-P. Ho, and S.-K. Kong, "Surface Plasmon

Resonance Biosensing via Differential Spectral Phase Interferometry," presented at the PLASMONICS IN BIOLOGY AND MEDICINE VIII, 2011, 2011, Proceedings Paper.

[56] R. S. Moirangthem, Y. C. Chang, S. H. Hsu, and P. K. Wei, "Surface plasmon resonance ellipsometry based sensor for studying biomolecular interaction," *Biosens Bioelectron,* vol. 25, no. 12, pp. 2633-8, Aug 15 2010.

[57] R. S. Moirangthem, Y.-C. Chang, S.-H. Hsu, and P.-K. Wei, "Surface plasmon resonance ellipsometry based sensor for studying biomolecular interaction," *Biosens Bioelectron,* Article vol. 25, no. 12, pp. 2633-2638, 2010 AUG 15 2010.

[58] Y. Shao, Y. Li, D. Gu, K. Zhang, J. Qu, J. He, X. Li, S. Y. Wu, H. P. Ho, M. G. Somekh, and H. Niu, "Wavelength-multiplexing phase-sensitive surface plasmon imaging sensor," *Opt Lett,* vol. 38, no. 9, pp. 1370-2, May 1 2013.

[59] G. Qiu, S. P. Ng, and C. M. L. Wu, "Differential phase-detecting localized surface plasmon resonance sensor with self-assembly gold nano-islands," *Opt Lett,* Article vol. 40, no. 9, pp. 1924-1927, 2015 MAY 1 2015.

[60] D. Sarid, "Long-Range Surface-Plasma Waves on Very Thin Metal Films," *Physical Review Letters,* vol. 47, no. 26, pp. 1927-1930, 12/28/ 1981.

[61] R. Slavik and J. Homola, "Ultrahigh resolution long range surface plasmon-based sensor," *Sensor Actuat B-Chem,* vol. 123, no. 1, pp. 10-12, Apr 10 2007.

[62] P. Yeh, A. Yariv, and C.-S. Hong, "Electromagnetic propagation in periodic stratified media. I. General theory*," *Journal of the Optical Society of America,* vol. 67, no. 4, pp. 423-438, 1977/04/01 1977.

[63] P. Hlubina, M. Gryga, D. Ciprian, P. Pokorny, L. Gembalova, and J. Sobota, "High performance liquid analyte sensing based on Bloch surface wave resonances in the spectral domain," *Optics & Laser Technology,* vol. 145, p. 107492, 2022/01/01/ 2022.

[64] F. Giorgis, E. Descrovi, C. Summonte, L. Dominici, and F. Michelotti, "Experimental determination of the sensitivity of Bloch Surface Waves based sensors," *Opt Express,* vol. 18, no. 8, pp. 8087-8093, 2010/04/12 2010.

[65] A. Sinibaldi, N. Danz, E. Descrovi, P. Munzert, U. Schulz, F. Sonntag, L. Dominici, and F. Michelotti, "Direct comparison of the performance of Bloch surface wave and surface plasmon polariton sensors," *Sensors and Actuators B: Chemical,* vol. 174, pp. 292-298, 2012/11/01/ 2012.

[66] W. Kong, Y. Wan, Z. Zheng, X. Zhao, Y. Liu, and Y. Bian, "High-sensitivity sensing based on intensity-interrogated Bloch surface wave sensors," in *IEEE Photonics Conference 2012*, 23-27 Sept. 2012 2012, pp. 204-205, doi: 10.1109/IPCon.2012.6358562.

[67] R. Slavík and J. Homola, "Ultrahigh resolution long range surface plasmon-based sensor," *Sensors and Actuators B: Chemical,* vol. 123, no. 1, pp. 10-12, 2007/04/10/ 2007.

[68] A. A. Yanik, A. E. Cetin, M. Huang, A. Artar, S. H. Mousavi, A. Khanikaev, J. H. Connor, G. Shvets, and H. Altug, "Seeing protein monolayers with naked eye through plasmonic Fano resonances," *Proceedings of the National Academy of Sciences of the United States of America,* vol. 108, no. 29, pp. 11784-11789, Jul 19 2011.

[69] H. Chen, X. Kou, Z. Yang, W. Ni, and J. Wang, "Shape- and size-dependent refractive index sensitivity of gold nanoparticles," *Langmuir,* vol. 24, no. 10, pp. 5233-5237, May 20 2008.

[70] E. Martinsson, B. Sepulveda, P. Chen, A. Elfwing, B. Liedberg, and D. Aili, "Optimizing the Refractive Index Sensitivity of Plasmonically Coupled Gold Nanoparticles," *Plasmonics,* vol. 9, no. 4, pp. 773-780, Aug 2014.

[71] M. Toma, K. Cho, J. B. Wood, and R. M. Corn, "- Gold Nanoring Arrays for Near Infrared Plasmonic Biosensing," vol. - 9, no. - 4, pp. - 772, 2014.

[72] H. Jiang, T. Li, J. Yang, S. Mittler, and J. Sabarinathan, "- Optimization of gold nanoring arrays for biosensing in the fiber-optic communication window," vol. - 24, no. - 46, 2013.

[73] D. E. Charles, D. Aherne, M. Gara, D. M. Ledwith, Y. K. Gun'ko, J. M. Kelly, W. J. Blau, and M. E. Brennan-Fournet, "Versatile Solution Phase Triangular Silver Nanoplates for Highly Sensitive Plasmon Resonance Sensing," *Acs Nano*, vol. 4, no. 1, pp. 55-64, Jan 2010.

[74] L. J. Sherry, R. C. Jin, C. A. Mirkin, G. C. Schatz, and R. P. Van Duyne, "Localized surface plasmon resonance spectroscopy of single silver triangular nanoprisms," *Nano Letters*, vol. 6, no. 9, pp. 2060-2065, Sep 2006.

[75] B. Xue, D. Wang, J. Zuo, X. G. Kong, Y. L. Zhang, X. M. Liu, L. P. Tu, Y. L. Chang, C. X. Li, F. Wu, Q. H. Zeng, H. F. Zhao, H. Y. Zhao, and H. Zhang, "Towards high quality triangular silver nanoprisms: improved synthesis, six-tip based hot spots and ultra-high local surface plasmon resonance sensitivity," *Nanoscale*, vol. 7, no. 17, pp. 8048-8057, 2015.

[76] J. J. Mock, S. J. Oldenburg, D. R. Smith, D. A. Schultz, and S. Schultz, "Composite plasmon resonant nanowires," *Nano Letters*, vol. 2, no. 5, pp. 465-469, May 2002.

[77] S. Czioska, J. Y. Wang, X. Teng, S. S. Zuo, S. H. Xie, and Z. F. Chen, "Hierarchically structured multi-shell nanotube arrays by self-assembly for efficient water oxidation," *Nanoscale*, vol. 10, no. 6, pp. 2887-2893, Feb 2018.

[78] K. M. Mayer and J. H. Hafner, "Localized Surface Plasmon Resonance Sensors," *Chemical Reviews*, vol. 111, no. 6, pp. 3828-3857, Jun 2011.

[79] A. Dahlin, "Biochemical Sensing with Nanoplasmonic Architectures: We Know How but Do We Know Why?," *Annual Review of Analytical Chemistry*, vol. 14, no. 1, pp. 281-297, 2021.

[80] S. A. Dereshgi, Z. Liu, and K. Aydin, "Anisotropic localized surface plasmons

in borophene," *Opt Express*, vol. 28, no. 11, pp. 16725-16739, 2020/05/25 2020.

[81] A. N. Grigorenko, M. Polini, and K. S. Novoselov, "Graphene plasmonics," *Nature Photonics*, vol. 6, no. 11, pp. 749-758, 2012/11/01 2012.

[82] B. Dong, C. Sun, and H. F. Zhang, "Optical Detection of Ultrasound in Photoacoustic Imaging," *IEEE Transactions on Biomedical Engineering*, vol. 64, no. 1, pp. 4-15, 2017.

[83] Q. Liu, Z. Jing, Y. Liu, A. Li, Z. Xia, and W. Peng, "- Multiplexing fiber-optic Fabry–Perot acoustic sensors using self-calibrating wavelength shifting interferometry," vol. - 27, no. - 26, pp. - 38203, 2019.

[84] E. Zhang, J. Laufer, and P. Beard, "Backward-mode multiwavelength photoacoustic scanner using a planar Fabry-Perot polymer film ultrasound sensor for high-resolution three-dimensional imaging of biological tissues," *Appl Optics*, Article vol. 47, no. 4, pp. 561-577, 2008 FEB 1 2008.

[85] G. C. Park and K. Park, "Critically coupled Fabry–Perot cavity with high signal contrast for refractive index sensing," *Sci Rep-Uk*, vol. 11, no. 1, p. 19575, 2021/10/01 2021.

[86] J. Zhang, Y. Rao, Z. Ran, and B. Xu, "Novel Fabry-Perot Fiber Refractive-Index Sensor With Microchannel," *Acta Optica Sinica*, vol. 30, no. 2, pp. 326-329, 2010, Art no. 0253-2239(2010)30:2<326:Dwtddx>2.0.Tx;2-c.

[87] C. Zhang, D. Yang, C. Miao, J. Zhao, H. Li, and H. Bai, "Large-range refractive index measurement method for open cavity Fabry–Pérot interferometer," *Meas Sci Technol*, vol. 30, no. 3, p. 035101, 2019/02/08 2019.

[88] S. Pevec and D. Donlagic, "Miniature fiber-optic Fabry-Perot refractive index sensor for gas sensing with a resolution of 5x10(-9) RIU," *Opt Express*, vol. 26, no. 18, pp. 23868-23882, Sep 2018.

[89] B. Xu, Y. Yang, Z. B. Jia, and D. N. Wang, "Hybrid Fabry-Perot interferometer

for simultaneous liquid refractive index and temperature measurement," *Opt Express*, vol. 25, no. 13, pp. 14483-14493, Jun 2017.

[90] S. Park, J. Eom, and B. H. Lee, "- Photoacoustic signal measurement using thin film Fabry-Perot optical interferometer for photoacoustic microscopy," vol. -, no. -, pp. - 3, 2015.

[91] X. Zou, N. Wu, Y. Tian, Y. Zhang, and X. Wang, "- Polydimethylsiloxane thin film characterization using all-optical photoacoustic mechanism," vol. - 52, no. - 25, pp. - 6244, 2013.

[92] P. C. Beard and T. N. Mills, *A 2D optical ultrasound array using a polymer film sensing interferometer* (2000 IEEE Ultrasonics Symposium. Proceedings. An International Symposium (Cat. No.00CH37121)). 2000, pp. 1183-6 vol.2.

[93] P. Morris, A. Hurrell, A. Shaw, E. Zhang, and P. Beard, "A Fabry–Pérot fiber-optic ultrasonic hydrophone for the simultaneous measurement of temperature and acoustic pressure," *The Journal of the Acoustical Society of America*, vol. 125, no. 6, pp. 3611-3622, 2009/06/01 2009.

[94] R. Ansari, E. Z. Zhang, A. E. Desjardins, and P. C. Beard, "All-optical forward-viewing photoacoustic probe for high-resolution 3D endoscopy," *LIGHT-SCIENCE & APPLICATIONS*, Article vol. 7, 2018 OCT 10 2018, Art no. 75.

[95] E. Z. Zhang and P. Beard, "2D backward-mode photoacoustic imaging system for NIR (650-1200nm) spectroscopic biomedical applications," presented at the PHOTONS PLUS ULTRASOUND: IMAGING AND SENSING 2006, 2006, 2006, Proceedings Paper.

[96] E. J. Alles, E. C. Mackle, S. Noimark, E. Z. Zhang, P. C. Beard, and A. E. Desjardins, "Freehand and video-rate all-optical ultrasound imaging," *ULTRASONICS*, Article vol. 116, 2021 SEP 2021, Art no. 106514.

[97] E. Z. Zhang, J. Laufer, B. Povazay, A. Alex, B. Hofer, W. Drexler, and P.

Beard, "Multimodal simultaneous photoacoustic tomography, optical resolution microscopy and OCT system," presented at the PHOTONS PLUS ULTRASOUND: IMAGING AND SENSING 2010, 2010, 2010, Proceedings Paper.

[98] L. Mengyang, C. Zhe, C. Sinz, E. Rank, B. Zabihian, E. Z. Zhang, P. C. Beard, H. Kittler, and W. Drexler, "Combined multimodal photoacoustic tomography, optical coherence tomography (OCT) and OCT based angiography system for in vivo imaging of multiple skin disorders in human(Conference Presentation)," *Proceedings of the SPIE - Progress in Biomedical Optics and Imaging*, Conference Paper vol. 10037, 2017.

[99] A. G. Samarentsis, A. K. Pantazis, A. Tsortos, J.-M. Friedt, and E. Gizeli, "Hybrid Sensor Device for Simultaneous Surface Plasmon Resonance and Surface Acoustic Wave Measurements," *Sensors-Basel*, vol. 20, no. 21, Nov 2020, Art no. 6177.

[100] T. Wang, R. Cao, B. Ning, A. J. Dixon, J. A. Hossack, A. L. Klibanov, Q. Zhou, A. Wang, and S. Hu, "All-optical photoacoustic microscopy based on plasmonic detection of broadband ultrasound," *Applied Physics Letters*, vol. 107, no. 15, Oct 12 2015, Art no. 153702.

[101] V. Wilkens, "Characterization of an optical multilayer hydrophone for use as broadband ultrasound reference receiver - comparison with PVDF membrane hydrophones," in *2002 IEEE Ultrasonics Symposium, 2002. Proceedings.*, 8-11 Oct. 2002 2002, vol. 1, pp. 773-776 vol.1, doi: 10.1109/ULTSYM.2002.1193513.

[102] C. M. Chow, Y. Zhou, Y. Guo, T. B. Norris, X. Wang, C. X. Deng, and J. Y. Ye, "Broadband optical ultrasound sensor with a unique open-cavity structure," (in eng), *J Biomed Opt*, vol. 16, no. 1, pp. 017001-017001, Jan-Feb 2011.

[103] W. Song, F. Yang, C. Min, S. Zhu, and X. Yuan, "Toward Ultrasensitive,

Broadband, Reflection-Mode In Vivo Photoacoustic Microscopy Using a Bare Glass," *Laser & Photonics Reviews,* vol. 17, no. 1, 2022.

[104] X. Zhu, Z. Huang, Z. Li, W. Li, X. Liu, Z. Chen, J. Tian, and C. Li, "Resolution-matched reflection mode photoacoustic microscopy and optical coherence tomography dual modality system," *Photoacoustics,* vol. 19, p. 100188, Sep 2020.

[105] W. Song, L. Peng, G. Guo, F. Yang, Y. Zhu, C. Zhang, C. Min, H. Fang, S. Zhu, and X. Yuan, "Isometrically Resolved Photoacoustic Microscopy Based on Broadband Surface Plasmon Resonance Ultrasound Sensing," *Acs Appl Mater Inter,* vol. 11, no. 30, pp. 27378-27385, 2019/07/31 2019.

[106] V. V. Yakovlev, W. Dickson, A. Murphy, J. McPhillips, R. J. Pollard, V. A. Podolskiy, and A. V. Zayats, "Ultrasensitive Non-Resonant Detection of Ultrasound with Plasmonic Metamaterials," *Adv Mater,* vol. 25, no. 16, pp. 2351-2356, Apr 2013.

[107] M. A. Ettabib, A. Marti, Z. Liu, B. M. Bowden, M. N. Zervas, P. N. Bartlett, and J. S. Wilkinson, "Waveguide Enhanced Raman Spectroscopy for Biosensing: A Review," *Acs Sensors,* vol. 6, no. 6, pp. 2025-2045, Jun 25 2021.

[108] W. Liu, Y. Shi, Z. Yi, C. Liu, F. Wang, X. Li, J. Lv, L. Yang, and P. K. Chu, "Surface plasmon resonance chemical sensor composed of a microstructured optical fiber for the detection of an ultra-wide refractive index range and gas-liquid pollutants," *Opt Express,* vol. 29, no. 25, pp. 40734-40747, 2021/12/06 2021.

[109] C. Chung, Y.-K. Kim, D. Shin, S.-R. Ryoo, B. H. Hong, and D.-H. Min, "Biomedical Applications of Graphene and Graphene Oxide," *Accounts Chem Res,* vol. 46, no. 10, pp. 2211-2224, Oct 15 2013.

[110] F. Vollmer and L. Yang, "Label-free detection with high-Q microcavities: a review of biosensing mechanisms for integrated devices," *Nanophotonics,* vol.

1, no. 3-4, pp. 267-291, 2012 2012.

[111] M. Piliarik, H. Sipova, P. Kvasnicka, N. Galler, J. R. Krenn, and J. Homola, "High-resolution biosensor based on localized surface plasmons," (in English), *Opt Express,* vol. 20, no. 1, pp. 672-680, Jan 2 2012.

[112] Y. Sun and X. Fan, "Optical ring resonators for biochemical and chemical sensing," *Anal Bioanal Chem,* vol. 399, no. 1, pp. 205-211, Jan 2011.

[113] J. T. Robinson, L. Chen, and M. Lipson, "On-chip gas detection in silicon optical microcavities," *Opt Express,* vol. 16, no. 6, pp. 4296-4301, Mar 17 2008.

[114] Y. Zhang, Z. Liang, D. Meng, Z. Qin, Y. Fan, X. Shi, D. R. Smith, and E. Hou, "All-dielectric refractive index sensor based on Fano resonance with high sensitivity in the mid-infrared region," *Results Phys,* vol. 24, May 2021, Art no. 104129.

[115] M. Q. Shen and M. G. Somekh, "A General Description of the Performance of Surface Plasmon Sensors Using a Transmission Line Resonant Circuit Model," (in English), *Ieee Sens J,* vol. 19, no. 23, pp. 11281-11288, Dec 1 2019.

[116] X. P. Jiang, M. Q. Shen, D. P. K. Lun, W. Chen, and M. G. Somekh, "High Aspect-Ratio Open Grating Fabry-Perot Resonator for High-Sensitivity Refractive Index Sensing," *Ieee Sens J,* vol. 22, no. 16, pp. 15923-15933, AUG 15 2022.

[117] P. Urbancova, D. Pudis, M. Goraus, and J. Kovac, Jr., "IP-Dip-Based SPR Structure for Refractive Index Sensing of Liquid Analytes," *Nanomaterials-Basel,* vol. 11, no. 5, May 2021, Art no. 1163.

[118] O. R. Bolduc, L. S. Live, and J.-F. Masson, "High-resolution surface plasmon resonance sensors based on a dove prism," *Talanta,* vol. 77, no. 5, pp. 1680-1687, Mar 15 2009.

[119] J.-Y. Jing, Q. Wang, W.-M. Zhao, and B.-T. Wang, "Long-range surface

plasmon resonance and its sensing applications: A review," *Opt Laser Eng,* vol. 112, pp. 103-118, 2019.

[120] E. Gonzalez-Valencia, I. D. Villar, and P. Torres, "Novel Bloch wave excitation platform based on few-layer photonic crystal deposited on D-shaped optical fiber," *Sci Rep-Uk,* vol. 11, no. 1, p. 11266, 2021/05/28 2021.

[121] R. Caroselli, S. Ponce-Alcantara, F. Prats Quilez, D. Martin Sanchez, L. Torrijos Moran, A. Griol Barres, L. Bellieres, H. Bandarenka, K. Girel, V. Bondarenko, and J. Garcia-Ruperez, "Experimental study of the sensitivity of a porous silicon ring resonator sensor using continuous in-flow measurements," *Opt Express,* vol. 25, no. 25, pp. 31651-31659, Dec 11 2017.

[122] S. Sasivimolkul, S. Pechprasarn, and M. G. Somekh, "Analysis of Open Grating-Based Fabry-Perot Resonance Structures With Potential Applications for Ultrasensitive Refractive Index Sensing," (in English), *Ieee Sens J,* vol. 21, no. 9, pp. 10628-10636, May 1 2021.

[123] O. Levy and D. Stroud, "Maxwell Garnett theory for mixtures of anisotropic inclusions: Application to conducting polymers," (in English), *Phys Rev B,* vol. 56, no. 13, pp. 8035-8046, Oct 1 1997.

[124] T. Liu, Y. Pang, M. Zhu, and S. Kobayashi, "Microporous Co@CoO nanoparticles with superior microwave absorption properties," (in English), *Nanoscale,* vol. 6, no. 4, pp. 2447-2454, 2014.

[125] A. Polemi and K. L. Shuford, "Transmission line equivalent circuit model applied to a plasmonic grating nanosurface for light trapping," *Opt Express,* vol. 20, no. S1, pp. A141-A156, 2012/01/02 2012.

[126] W. Song, Y.-c. Wang, H. Chen, X. Li, L. Zhou, C. Min, S. Zhu, and X. Yuan, "Label-free identification of human glioma xenograft of mouse brain with quantitative ultraviolet photoacoustic histology imaging," *J Biophotonics,* Article vol. 15, no. 5, 2022 MAY 2022, Art no. e202100329.

[127] "adhesion promoter ar 300-80 new." https://www.allresist.com/portfolio-item/adhesion-promoter-ar-300-80-new/ (accessed Feb 28, 2023).

[128] "e-beam resist ar-p 672 series." https://www.allresist.com/portfolio-item/e-beam-resist-ar-p-672-series/ (accessed Feb 28, 2023).

[129] S. G. Nelson, K. S. Johnston, and S. S. Yee, "High sensitivity surface plasmon resonace sensor based on phase detection," *Sensors and Actuators B: Chemical*, vol. 35, no. 1, pp. 187-191, 1996/09/01/ 1996.

[130] S.-L. Chen and C. Tian, "Recent developments in photoacoustic imaging and sensing for nondestructive testing and evaluation," *Visual Computing for Industry, Biomedicine, and Art*, vol. 4, no. 1, p. 6, 2021/03/19 2021.

[131] A. B. E. Attia, G. Balasundaram, M. Moothanchery, U. S. Dinish, R. Z. Bi, V. Ntziachristos, and M. Olivo, "A review of clinical photoacoustic imaging: Current and future trends," *Photoacoustics*, vol. 16, DEC 2019, Art no. 100144.

[132] G. Paltauf, R. Nuster, and M. Frenz, "Progress in biomedical photoacoustic imaging instrumentation toward clinical application," *JOURNAL OF APPLIED PHYSICS*, Article vol. 128, no. 18, 2020 NOV 14 2020, Art no. 180907.

[133] Y. R. Gu, Y. Y. Sun, X. Wang, H. Y. Li, J. F. Qiu, and W. Z. Lu, "Application of photoacoustic computed tomography in biomedical imaging: A literature review," *BIOENGINEERING & TRANSLATIONAL MEDICINE*.

[134] J. Yao and L. V. Wang, "Photoacoustic microscopy," *LASER & PHOTONICS REVIEWS*, Review vol. 7, no. 5, pp. 758-778, 2013 SEP 2013.

[135] J. Kim, J. Y. Kim, S. Jeon, J. W. Baik, S. H. Cho, and C. Kim, "Super-resolution localization photoacoustic microscopy using intrinsic red blood cells as contrast absorbers," *LIGHT-SCIENCE & APPLICATIONS*, Article vol. 8, 2019 NOV 20 2019, Art no. 103.

[136] X. Deng, T. Xu, G. Huang, Q. Li, L. Luo, Y. Zhao, Z. Wu, J. Ou-Yang, X. Yang, M. Xie, and B. Zhu, "Design and Fabrication of a Novel Dual-Frequency Confocal Ultrasound Transducer for Microvessels Super-Harmonic Imaging," *Ieee T Ultrason Ferr,* Article vol. 68, no. 4, pp. 1272-1277, 2021 APR 2021.

[137] X. Jiang, M. Shen, D. P.-K. Lun, W. Chen, and M. G. Somekh, "A total-internal-reflection-based Fabry–Pérot resonator for ultra-sensitive wideband ultrasound and photoacoustic applications," *Photoacoustics,* vol. 30, p. 100466, 2023/04/01/ 2023.

[138] A. Jakob, M. Bender, T. Knoll, R. Lemor, T. Lehnert, M. Koch, M. Veith, Q. Zhou, B. P. Zhu, J. X. Han, and K. K. Shung, "Comparison of different piezoelectric materials for GHz acoustic microscopy transducers," in *2009 IEEE International Ultrasonics Symposium*, 20-23 Sept. 2009 2009, pp. 1722-1725, doi: 10.1109/ULTSYM.2009.5442024.

[139] K. K. Shung, J. M. Cannata, and Q. F. Zhou, "Piezoelectric materials for high frequency medical imaging applications: A review," *Journal of Electroceramics,* vol. 19, no. 1, pp. 141-147, 2007.

[140] J. Bamber, D. Cosgrove, C. F. Dietrich, J. Fromageau, J. Bojunga, F. Calliada, V. Cantisani, J. M. Correas, M. D'Onofrio, E. E. Drakonaki, M. Fink, M. Friedrich-Rust, O. H. Gilja, R. F. Havre, C. Jenssen, A. S. Klauser, R. Ohlinger, A. Saftoiu, F. Schaefer, I. Sporea, and F. Piscaglia, "EFSUMB Guidelines and Recommendations on the Clinical Use of Ultrasound Elastography. Part 1: Basic Principles and Technology," *ULTRASCHALL IN DER MEDIZIN,* Article vol. 34, no. 2, pp. 169-184, 2013 APR 2013.

[141] Q. Zhou, S. Lau, D. Wu, and K. Kirk Shung, "Piezoelectric films for high frequency ultrasonic transducers in biomedical applications," *Progress in Materials Science,* vol. 56, no. 2, pp. 139-174, 2011/02/01/ 2011.

[142] Y. Liu, T. Seresini, J.-Y. Liu, L. Liu, F. Wang, Y. Wang, and C. Glorieux, "All-optical dynamic analysis of the photothermal and photoacoustic response of a microcantilever by laser Doppler vibrometry," *Photoacoustics,* Article vol. 24, 2021 DEC 2021, Art no. 100299.

[143] S. Learkthanakhachon, S. Pechprasarn, and M. G. Somekh, "Optical detection of ultrasound by lateral shearing interference of a transparent PDMS thin film," *Opt Lett,* vol. 43, no. 23, pp. 5797-5800, Dec 1 2018.

[144] F. Yang, W. Song, C. Zhang, H. Fang, C. Min, and X. Yuan, "A Phase-Shifted Surface Plasmon Resonance Sensor for Simultaneous Photoacoustic Volumetric Imaging and Spectroscopic Analysis," *Acs Sensors,* Article vol. 6, no. 5, pp. 1840-1848, 2021 MAY 28 2021.

[145] H. Ichihashi, S. Ueno, T. Fukunaga, S. Takayanagi, and M. Matsukawa, "Signal Amplification of the Transient Response Measured by the Subnanosecond Pump-Probe Method Based on Surface Plasmon Resonance," *Ieee T Ultrason Ferr,* Article vol. 69, no. 6, pp. 2152-2161, 2022 JUN 2022.

[146] H. Li, B. Q. Dong, Z. Zhang, H. F. Zhang, and C. Sun, "A transparent broadband ultrasonic detector based on an optical micro-ring resonator for photoacoustic microscopy," *Sci Rep-Uk,* vol. 4, MAR 28 2014, Art no. 4496.

[147] H. Li, B. Q. Dong, X. Zhang, X. Shu, X. F. Chen, R. H. Hai, D. A. Czaplewski, H. F. Zhang, and C. Sun, "Disposable ultrasound-sensing chronic cranial window by soft nanoimprinting lithography," *NATURE COMMUNICATIONS,* vol. 10, SEP 19 2019, Art no. 4277.

[148] W. Song, Y. S. Dong, Y. X. Shan, F. Yang, C. J. Min, and X. C. Yuan, "Ultrasensitive broadband photoacoustic microscopy based on common-path interferometric surface plasmon resonance sensing," *Photoacoustics,* vol. 28, DEC 2022, Art no. 100419.

[149] F. Yang, G. Guo, S. Zheng, H. Fang, C. Min, W. Song, and X. Yuan,

"Broadband surface plasmon resonance sensor for fast spectroscopic photoacoustic microscopy," *Photoacoustics*, vol. 24, p. 100305, Dec 2021.

[150] G. Dai, N. Yu, S. Zhang, L.-P. Sun, J. Li, J. Ma, and B.-O. Guan, "Photothermally stabilized Fabry-Perot cavity with patterned nanofilm for photoacoustic trace gas sensing," *Sensor Actuat B-Chem*, Article vol. 355, 2022 MAR 15 2022, Art no. 131259.

[151] Z. Gong, T. Gao, Y. Chen, Y. Jiao, K. Chen, and Q. Yu, "Parylene-C diaphragm-based fiber-optic gas sensor based on photoacoustic spectroscopy," presented at the 2019 INTERNATIONAL CONFERENCE ON OPTICAL INSTRUMENTS AND TECHNOLOGY: OPTOELECTRONIC IMAGING/SPECTROSCOPY AND SIGNAL PROCESSING TECHNOLOGY, 2020, 2020, Proceedings Paper.

[152] X. Wang, Y. Jiang, Z. Li, W. Wang, and Z. Li, "Sensitivity Characteristics of Microfiber Fabry-Perot Interferometric Photoacoustic Sensors," *J Lightwave Technol*, Article vol. 37, no. 17, pp. 4229-4235, 2019 SEP 1 2019.

[153] P. Morris, A. Hurrell, A. Shaw, E. Zhang, and P. Beard, "A Fabry-Perot fiber-optic ultrasonic hydrophone for the simultaneous measurement of temperature and acoustic pressure," *JOURNAL OF THE ACOUSTICAL SOCIETY OF AMERICA*, Article vol. 125, no. 6, pp. 3611-3622, 2009 JUN 2009.

[154] S. Sasivimolkul, S. Pechprasarn, and M. G. Somekh, "Analysis of Open Grating-Based Fabry-Perot Resonance Structures With Petential Applications for Ultrasensitive Refractive Index Sensing," *Ieee Sens J*, vol. 21, no. 9, pp. 10628-10636, 2021.

[155] B. T. Cox and P. C. Beard, "The frequency-dependent directivity of a planar fabry-perot polymer film ultrasound sensor," *IEEE Transactions on Ultrasonics, Ferroelectrics, and Frequency Control*, vol. 54, no. 2, pp. 394-404, 2007.

[156] S. Kuhr, S. Gleyzes, C. Guerlin, J. Bernu, U. B. Hoff, S. Deleglise, S. Osnaghi, M. Brune, J. M. Raimond, S. Haroche, E. Jacques, P. Bosland, and B. Visentin, "Ultrahigh finesse Fabry-Perot superconducting resonator," *APPLIED PHYSICS LETTERS,* Article vol. 90, no. 16, 2007 APR 16 2007, Art no. 164101.

[157] D. Nesterenko, S. Hayashi, and V. Soifer, "Approximation of Fabry-Perot resonances in Ag/quartz/Ag structures," presented at the 2020 VI INTERNATIONAL CONFERENCE ON INFORMATION TECHNOLOGY AND NANOTECHNOLOGY (IEEE ITNT-2020), 2020, 2020, Proceedings Paper.

[158] N. Uddin, M. Shrestha, B. Zheng, H.-J. Yoon, X. Wang, and Q. H. Fan, "Liquid Sensors Based on Enhanced Fabry-Perot Etalons," *Ieee Sens J,* Article vol. 17, no. 22, pp. 7348-7354, 2017 NOV 15 2017.

[159] H. Jiang, C. Liu, P. Wang, D. Zhang, Y. Lu, and H. Ming, "High-Q/Veff gap-mode plasmonic FP nanocavity," *Opt Express,* Article vol. 21, no. 4, pp. 4752-4757, 2013 FEB 25 2013.

[160] L. P. Wang, S. Basu, and Z. M. Zhang, "Direct Measurement of Thermal Emission From a Fabry-Perot Cavity Resonator," *JOURNAL OF HEAT TRANSFER-TRANSACTIONS OF THE ASME,* Article vol. 134, no. 7, 2012 JUL 2012, Art no. 072701.

[161] X. Hu, M. Li, Z. Ye, W. Y. Leung, K.-M. Ho, and S.-Y. Lin, "Design of midinfrared photodetectors enhanced by resonant cavities with subwavelength metallic gratings," *APPLIED PHYSICS LETTERS,* Article vol. 93, no. 24, 2008 DEC 15 2008, Art no. 241108.

[162] J. Buchmann, J. Guggenheim, E. Zhang, C. Scharfenorth, B. Spannekrebs, C. Villringer, and J. Laufer, "Characterization and modeling of Fabry-Perot ultrasound sensors with hard dielectric mirrors for photoacoustic imaging,"

Appl Opt, vol. 56, no. 17, pp. 5039-5046, Jun 10 2017.

[163] A. A. Oraevsky, L. V. Wang, J. Buchmann, E. Zhang, C. Scharfenorth, B. Spannekrebs, C. Villringer, and J. Laufer, "Evaluation of Fabry-Perot polymer film sensors made using hard dielectric mirror deposition," presented at the Photons Plus Ultrasound: Imaging and Sensing 2016, 2016.

[164] X. Jiang, M. Shen, D. P.-K. Lun, W. Chen, and M. G. Somekh, "A total-internal-reflection-based Fabry-Perot resonator for ultra-sensitive wideband ultrasound and photoacoustic applications," *Photoacoustics,* Journal Article vol. 30, pp. 100466-100466, 2023 Apr 2023.

[165] L. Gao, F. Lemarchand, and M. Lequime, "Comparison of different dispersion models for single layer optical thin film index determination," *THIN SOLID FILMS,* Article vol. 520, no. 1, pp. 501-509, 2011 OCT 31 2011.

[166] X. Zhang, J. Qiu, X. Li, J. Zhao, and L. Liu, "Complex refractive indices measurements of polymers in visible and near-infrared bands," *Appl Opt,* vol. 59, no. 8, pp. 2337-2344, Mar 10 2020.

[167] G. M. Hale and M. R. Querry, "OPTICAL-CONSTANTS OF WATER IN 200-NM TO 200-MUM WAVELENGTH REGION," *Appl Optics,* Article vol. 12, no. 3, pp. 555-563, 1973 1973.

[168] W. Xia, D. Piras, J. Hespen, W. Steenbergen, and S. Manohar, "A new acoustic lens material for large area detectors in photoacoustic breast tomography," *Photoacoustics,* vol. 1, 05/17 2013.

[169] G. Xu, Z. Ni, X. Chen, J. Tu, X. Guo, H. Bruus, and D. Zhang, "Acoustic Characterization of Polydimethylsiloxane for Microscale Acoustofluidics," *PHYSICAL REVIEW APPLIED,* Article vol. 13, no. 5, 2020 MAY 27 2020, Art no. 054069.

[170] J. K. Tsou, J. Liu, A. I. Barakat, and M. F. Insana, "Role of ultrasonic shear rate estimation errors in assessing inflammatory response and vascular risk,"

ULTRASOUND IN MEDICINE AND BIOLOGY, Article vol. 34, no. 6, pp. 963-972, 2008 JUN 2008.

[171] F. Yang, W. Song, C. L. Zhang, H. Fang, C. J. Min, and X. C. Yuan, "A Phase-Shifted Surface Plasmon Resonance Sensor for Simultaneous Photoacoustic Volumetric Imaging and Spectroscopic Analysis," (in English), *Acs Sensors*, vol. 6, no. 5, pp. 1840-1848, May 28 2021.

[172] D. R. Ramasawmy, E. Martin, J. A. Guggenheim, E. Z. Zhang, P. C. Beard, B. E. Treeby, and B. T. Cox, "Analysis of the Directivity of Glass-Etalon Fabry–Pérot Ultrasound Sensors," *IEEE Transactions on Ultrasonics, Ferroelectrics, and Frequency Control,* vol. 66, no. 9, pp. 1504-1513, 2019.

[173] E. Baumann, U. Pohle, E. Zhang, T. Allen, C. Villringer, S. Pulwer, H. Gerhardt, and J. Laufer, "A backward-mode optical-resolution photoacoustic microscope for 3D imaging using a planar Fabry-Perot sensor," *Photoacoustics,* Article vol. 24, 2021 DEC 2021, Art no. 100293.

[174] J. Huang, Y. Cai, C. Xue, J. Ge, H. Zhao, and S.-H. Yu, "Highly stretchable, soft and sticky PDMS elastomer by solvothermal polymerization process," *Nano Research,* vol. 14, no. 10, pp. 3636-3642, 2021.

[175] S. H. Jeong, S. Zhang, K. Hjort, J. Hilborn, and Z. Wu, "PDMS-Based Elastomer Tuned Soft, Stretchable, and Sticky for Epidermal Electronics," *Adv Mater,* vol. 28, no. 28, pp. 5830-5836, 2016/07/01 2016.

[176] C. F. Carlborg, T. Haraldsson, K. Öberg, M. Malkoch, and W. van der Wijngaart, "Beyond PDMS: off-stoichiometry thiol–ene (OSTE) based soft lithography for rapid prototyping of microfluidic devices," *Lab on a Chip,* 10.1039/C1LC20388F vol. 11, no. 18, pp. 3136-3147, 2011.

[177] A. Kossoy, V. Merk, D. Simakov, K. Leosson, S. Kéna-Cohen, and S. A. Maier, "Optical and Structural Properties of Ultra-thin Gold Films," *Adv Opt Mater,* vol. 3, no. 1, pp. 71-77, 2015/01/01 2015.

[178] W. Song, L. L. Peng, G. D. Guo, F. Yang, Y. Zhu, C. L. Zhang, C. J. Min, H. Fang, S. W. Zhu, and X. C. Yuan, "Isometrically Resolved Photoacoustic Microscopy Based on Broadband Surface Plasmon Resonance Ultrasound Sensing," (in English), *Acs Appl Mater Inter,* vol. 11, no. 30, pp. 27378-27385, Jul 31 2019.

[179] K. Fukuda, Y. Takeda, Y. Yoshimura, R. Shiwaku, T. Lam Truc, T. Sekine, M. Mizukami, D. Kumaki, and S. Tokito, "Fully-printed high-performance organic thin-film transistors and circuitry on one-micron-thick polymer films," *NATURE COMMUNICATIONS,* Article vol. 5, 2014 JUN 2014, Art no. 4147.

[180] A. J. T. Teo, A. Mishra, I. Park, Y.-J. Kim, W.-T. Park, and Y.-J. Yoon, "Polymeric Biomaterials for Medical Implants and Devices," *ACS BIOMATERIALS SCIENCE & ENGINEERING,* Review vol. 2, no. 4, pp. 454-472, 2016 APR 2016.

[181] A. Ciesielski, L. Skowronski, M. Trzcinski, and T. Szoplik, "Controlling the optical parameters of self-assembled silver films with wetting layers and annealing," *Appl Surf Sci,* vol. 421, pp. 349-356, Nov 1 2017.

[182] D. Rioux, S. Vallieres, S. Besner, P. Munoz, E. Mazur, and M. Meunier, "An Analytic Model for the Dielectric Function of Au, Ag, and their Alloys," *Adv Opt Mater,* vol. 2, no. 2, pp. 176-182, Feb 2014.

[183] B. Karki, A. Pal, Y. Singh, and S. Sharma, "Sensitivity enhancement of surface plasmon resonance sensor using 2D material barium titanate and black phosphorus over the bimetallic layer of Au, Ag, and Cu," *Opt Commun,* Article vol. 508, 2022 APR 1 2022, Art no. 127616.

[184] P. C. Beard, F. Perennes, and T. N. Mills, "Transduction mechanisms of the Fabry-Perot polymer film sensing concept for wideband ultrasound detection," *IEEE Transactions on Ultrasonics, Ferroelectrics, and Frequency Control,* vol. 46, no. 6, pp. 1575-1582, 1999.

[185] C. J. Chang-Hasnain and W. Yang, "High-contrast gratings for integrated optoelectronics," *Advances in Optics and Photonics*, vol. 4, no. 3, pp. 379-440, 2012/09/30 2012.

[186] V. Karagodsky and C. J. Chang-Hasnain, "Physics of near-wavelength high contrast gratings," *Opt Express*, vol. 20, no. 10, pp. 10888-10895, 2012/05/07 2012.

[187] P. Qiao, L. Zhu, W. C. Chew, and C. J. Chang-Hasnain, "Theory and design of two-dimensional high-contrast-grating phased arrays," *Opt Express*, vol. 23, no. 19, pp. 24508-24524, 2015/09/21 2015.

[188] P. Lalanne, J. P. Hugonin, and P. Chavel, "Optical Properties of Deep Lamellar Gratings: A Coupled Bloch-Mode Insight," *J Lightwave Technol*, vol. 24, no. 6, p. 2442, 2006/06/01 2006.

[189] Santec. "TSL-770." https://inst.santec.com/products/tunablelaser/tsl-770 (accessed 6.1, 2023).

[190] H. H. Li, "Refractive index of alkaline earth halides and its wavelength and temperature derivatives," *Journal of Physical and Chemical Reference Data*, vol. 9, no. 1, pp. 161-290, 1980.

[191] H. H. Li, "Refractive index of alkali halides and its wavelength and temperature derivatives," *Journal of Physical and Chemical Reference Data*, vol. 5, no. 2, pp. 329-528, 1976.

[192] J. A. Liddle and G. M. Gallatin, "Nanomanufacturing: A Perspective," *Acs Nano*, Review vol. 10, no. 3, pp. 2995-3014, 2016 MAR 2016.

[193] K. J. Byeon and H. Lee, "Recent progress in direct patterning technologies based on nano-imprint lithography," *Eur Phys J-Appl Phys*, Review vol. 59, no. 1, 2012 JUL 2012, Art no. 10001.